# Electronic and Vibrational States of Point Defects in Semiconductors

Thesis by

Randall Meindert Feenstra

In Partial Fulfillment of the Requirements

for the Degree of

Doctor of Philosophy

California Institute of Technology

Pasadena, California

1982

(Submitted May 26, 1982)

To my parents

## ACKNOWLEDGEMENTS

I would like to thank Dr. T. C. McGill for his support and assistance during the course of this work. Dr. McGill has provided me with excellent laboratory facilities, and an environment which was very conducive to research. I have benefited greatly from his careful reading of my research papers, and of this manuscript. I would also like to thank Vere Snell for her excellent and cheerful secretarial help.

I am very grateful to many people at Caltech for informative and stimulating discussions about physics. Drs. D. L. Smith and J. J. Lambe have illuminated many points for me and have provided fresh ideas for my research. I am particularly grateful to Drs. K. R. Elliott, A. T. Hunter, and G. S. Mitchard for helping me get started in the laboratory, and providing me with valuable guidance during my work. I would like to thank B. M. Clemens, R. T. Collins, and Dr. C. A. Swarts for many helpful discussions. I am grateful to Drs. R. R. Johnson, R. R. Parsons, and D. Ll. Williams of the University of British Columbia who originally encouraged me to pursue a career in physics.

I am deeply indebted to Dr. C. H. Henry of Bell Telephone Laboratories for providing the GaP samples used in this work. The major part of this thesis is concerned with a study of these GaP samples. The numerous contributions of Dr. Henry to the field of semiconductor physics have greatly aided me in understanding the results of my experiments. I would also like to thank Drs. O. J. Marsh and J. P. Baukus of Hughes Research Laboratories for providing the Si samples used in this work.

For financial support, I gratefully acknowledge the Natural Sciences and Engineering Research Council of Canada, California Institute of Technology, and the Office of Naval Research.

## ABSTRACT

This thesis deals with the properties of defects in tetrahedrally-bonded semiconductors. The defects which will be studied here are impurity atoms substitutional for host atoms in the crystal. In particular, those defects which produce localized electronic states in the middle of the electronic energy gap ("deep levels") will be discussed. The main experimental technique used is photoluminescence. The crystals are excited with a laser, and they emit light due to various electronic transitions at the defects. The energy of this luminescence yields information about the nature of the excited electronic states. Also, excited vibrational states of the defects are apparent in the luminescence, and these vibrational states yield structural information about the defect.

The major system studied here is GaP containing Zn and O impurities. The Zn and O ions experience an attractive Coulomb interaction, so that they tend to occupy lattice sites which are near to each other, forming defect pairs. The energy of luminescence emitted from a (Zn,O) pair depends on the separation of the impurities. Thus, a luminescence spectrum contains information about the number of pairs of each possible separation. I have used this phenomenon to monitor the relative positions of Zn and O impurities in the lattice. I have observed reactions in which the impurity atoms move through the lattice under the influence of laser excitation. Specifically, I observe the dissociation of nearest-neighbor (Zn,O) pairs, and the subsequent formation of further separated pairs. The dissociation of the nearest-neighbor pairs can occur thermally, or by a photoinduced mechanism. At temperatures near 200 C, the intensity of the (Zn,O) luminescence spectra changes with time, a direct observation of the photoinduced reactions in progress. The (Zn,O) pairs are observed to dissociate by purely thermal means at temperatures near 900 C. From the rates of these two types of reactions, I identify the photoinduced pair dissociation as being a "recombination-enhanced

defect reaction". In the reaction, electron-hole recombination puts the defect into a highly excited vibrational state, leading to the dissociation. This is the first observation of this sort of reaction in a system with known defect types. Thus, my study provides unique information about the electron-phonon interaction at defects. This study also has some practical application. The material GaP:(Zn,O) is used for fabricating red light-emitting-diodes, and the dissociation of the pairs provides an explanation for the degradation of these diodes. Presumably the degradation of some other semiconductor devices proceeds by mechanisms similar to those observed here.

This thesis deals with several other topics aside from GaP:(Zn,O). The geometry of impurity pairs in zinc-blende crystals is discussed. For a given separation of the impurity atoms, there is some number of different possible relative orientations of the impurities. I have derived an analytic form for this distribution of impurity pair separations, and I show how this formula can be used to interpret the observed luminescence spectra of GaP:N. Another system studied here is Si containing In and B impurities. Recombination of excitons bound onto the impurities produces luminescence. From the observed decay times of these luminescence lines, I deduce values of the cross sections for free exciton capture onto In and B impurities. The magnitude of the In cross section indicates the presence of excited states of the In bound exciton. Finally, a theoretical treatment of the vibrational modes of substitutional defects in zinc-blende crystals is presented. The defects consist of an impurity atom, with springs of variable strength connecting it to its neighbors. For the case of oxygen in GaP, the theory predicts the existence of two defect vibrational modes, in agreement with experiment. From the energies of the observed vibrational modes, it appears that the oxygen impurity is quite weakly bonded to its neighboring atoms.

Parts of this thesis have been or will be published under the following titles:

Chapter 2:

**Periodicity in the Undulation Spectra of GaP:N**,

R. M. Feenstra and T. C. McGill, *Phys. Rev. B Brief Reports* **26**, 1 (1982).

Chapter 3:

**Defect Reactions in GaP:(Zn,O)**,

R. M. Feenstra and T. C. McGill, *Phys. Rev. Lett.* **47**, 925 (1981).

**Reaction Kinetics in GaP:(Zn,O)**,

R. M. Feenstra and T. C. McGill, *Phys. Rev. B* **25**, Vol. 10 (1982).

Chapter 4:

**Exciton Capture Cross Sections of Boron and Indium Impurities in Silicon**,

R. M. Feenstra and T. C. McGill, *Solid State Comm.* **36**, 1039 (1980).

Chapter 5:

**Vibrational Modes of Oxygen in GaP**,

R. M. Feenstra and T. C. McGill, in preparation.

# CONTENTS

# CHAPTER 1

# ELECTRONIC AND VIBRATIONAL STATES OF POINT DEFECTS IN SEMICONDUCTORS

## 1.1 Introduction

The quantum theory of solids attempts to divide a system into different types of excitations. Each type of excitation has some set of energy levels (eigenstates, normal modes). These energy levels are occupied by the "particles" of the system. For example, the electronic eigenstates are occupied by *electrons*, and the vibrational states of the atoms are occupied by *phonons*. In the first approximation we view these excitations as noninteracting. For certain ranges of energy this may indeed be a good approximation. Weak interactions between the excitations can be viewed as causing transitions of the particles between the energy levels. Strong interactions give rise to strongly coupled excitations, in which case the physics of both types of excitations must be treated together and the result is some new type of excitation.

The particles we will be considering here consist of electrons and phonons in crystalline solids, and their interaction with *photons* (electromagnetic waves which propogate through the material). These photons cause transitions of the electrons between various states. In some cases it will be convenient to view an unoccupied electron state as a hole in the occupation of the states, and these *holes* will be regarded as another type of particle. The photons we will be using in the experiments described here are of the energy range 1–2 eV (in or near the visible part of the spectrum). The phonons have energies typically 50 meV or less, and the electronic states we will be considering have energies ranging from 1 meV–2 eV. Our experiments involve the transfer of energy between these different types of excitations. In Fig. 1.1 we show the major processes which occur; (a) a photon is absorbed to create an electron-hole pair, (b) an electron-hole pair recombines to produce a photon, and (c) an electron-hole pair recombines to produce many phonons. The sequence of events which occur in a typical experiment are pictured

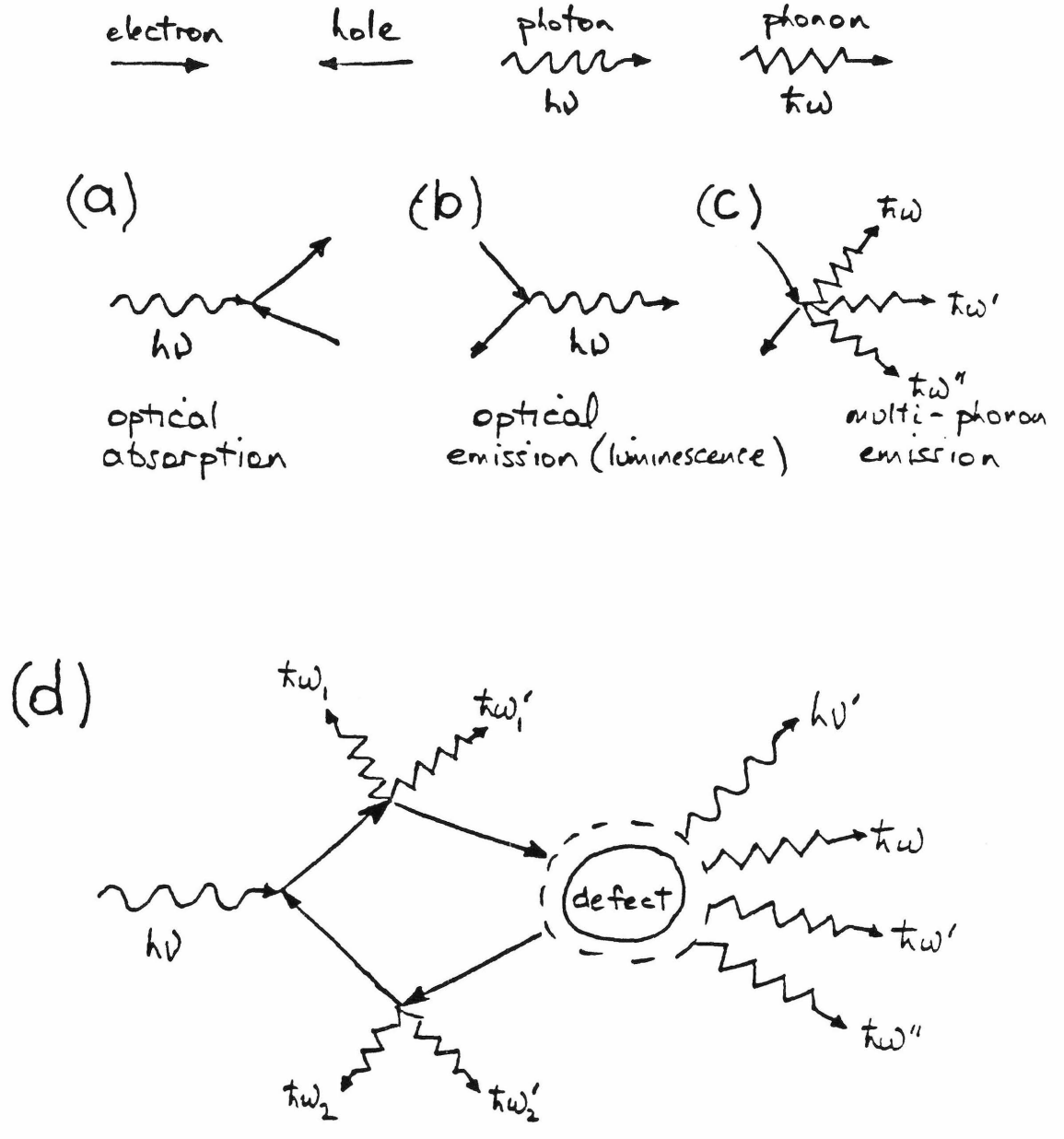


**Figure 1.1:** Important processes which occur in photoluminescence experiments: (a) optical absorption, (b) optical emission (luminescence), and (c) multi-phonon emission. (d) A sequence of events occurring in a typical experiment: the incident laser light is absorbed to created excited electrons and holes, which lose energy by phonon emission to become bound onto a defect, and eventually recombine with the emission of a photon and one or more phonons.

in Fig. 1.1(d). An incident photon from a laser is absorbed to produce an excited electron-hole pair, the electron and hole lose energy by phonon emission, they eventually become bound onto a defect in the material, and finally the electron and hole recombine to produce a photon and one or more phonons.

In this thesis, we will be studying the properties of those materials known as tetrahedrally-bonded semiconductors. These include the elements from Column IV of the periodic table (*e.g.* Si), and also the compounds from Columns III-V (*e.g.* GaP), and Columns II-VI. The elemental semiconductors are of course covalent, and the compound semiconductors are also at least partially covalent. Thus, a suitable picture for the structure of the material consists of localized bonds, with the electrons residing in the region between the atomic cores[1]. Each atom has four nearest-neighbors, and the point group symmetry about each atomic site is $T_d$. The electronic states in these materials can be divided into three groups; the core levels, the valence band, and the conduction band. An energy gap of the order of 1 eV exists between the valence and conduction bands. At zero temperature, in a pure material, the valence band is full of electrons and the conduction band is empty of electrons. In this situation the material is an insulator, since the electrons are not free to propagate through the crystal (full bands carry no net current). Even at room temperature, pure (intrinsic) conduction is very small. However, by introducing small amounts of impurities into these materials we can drastically modify their electrical characteristics. Certain impurities known as *donors* will donate electrons to the conduction band. These electrons are free to move through the states of the band, and in this way they carry a net current. Other impurities known as *acceptors* will accept electrons from the valence band, leaving behind a hole in the valence band. The holes carry current in the valence band. Thus there are two types of carriers, electrons and holes, and the currents

in a real device are divided up in various ways between these carriers.

By judiciously introducing donor and acceptor impurities into semiconductors we are able to accurately control their electrical properties. The preparations of semiconductors in this way has led to the development of transistors, and eventually led to the revolution in computer technology which is occurring at the present time. Aside from the donor and acceptor impurities present in the material, there always exist other defects. These defects may (and often do) produce unwanted electrical behavior. For this reason, the identification and characterization of defects in semiconductors is of very practical use. The study of these defects is also interesting for its own sake since it employs very modern experimental and theoretical techniques. The defects which we will be mainly concerned with in this thesis are impurity atoms which are substitutional for host atoms in the lattice. However, many of the considerations should also apply to other point defects such as vacancies and interstitial impurities.

Generally speaking, most of the investigations of defects in semiconductors to date have concentrated on their electrical properties. This is not surprising, since it is these properties which directly affect device operation. However, the vibrational properties of the defects have recently been under more investigation. When the excited electrons in the material relax, their energy can be dissipated in the form of phonons. Such an event is known as nonradiative recombination by multi-phonon emission, as shown in Fig. 1.1(c). This type of recombination will limit the lifetime of carriers in the device, and thus lead to poor device performance. Also, the energy which is transferred to the phonons may be localized in some region around an impurity. This may lead to *motion* of the impurity atoms through the material. In this thesis we report on the first real identification of such a process in a semiconductor[2], and we show how this is

directly responsible for the degradation of a semiconductor device.

In this chapter, we will give a brief introduction to the electronic and vibrational states of point defects in semiconductors. In Section 1.2 we will discuss the nature of the states. It is shown that the states of a perfect lattice are basically just plane waves, labelled by their wave-vector **k**. We will present energy levels for the electrons and phonons in GaP. Then we will discuss what happens when we introduce a defect into the material. The translational symmetry of the perfect lattice is lost, and we are reduced to the point group symmetry of the defect. The states of the defect are labelled according to the point group symmetry. We give some examples of these defect states, including shallow electronic levels, deep electronic levels, and vibrational levels. In Section 1.3 we will discuss in greater detail how photoluminescence can be used to probe the electronic and vibrational states of the defects. We consider the effects of having donor and acceptor impurities close to each other in the crystal. The luminescence resulting from this pair of impurities is shown to depend on their relative separation, so that the spectrum gives us information about the number of pairs of each possible separation. We also discuss the effects in the luminescence spectrum of having phonons emitted in the electronic transition. We show how the spectrum gives us information about the vibrational modes of a defect, which tells us something about the local environment of the defect in the crystal. In Section 1.4 a summary of Chapters 2–5 is presented.

## 1.2 The Nature of the States

### 1.2.1 States of the Perfect Lattice

Let us now consider the states of a perfect lattice. In general the excitations in a system will not be truly noninteracting. The description of the entire system is a very complicated many-body problem. In order to make progress, we approximate the Hamiltonian by some one-body operator which describes the states of a system in which the particles move in the *mean-field* of all the other particles. The resulting states are known as single-particle states. The particles in the system are seen as occupying these states, and forming a gas of weakly interacting particles. For electrons in semiconductors, many-body effects are certainly important in any theoretical descriptions of the material, but conceptually it is usually sufficient to simply consider the single-particle states of the system. Phonons are a much better example of noninteracting particles, at least in a completely covalent material. In any case, in the following discussion we will restrict ourselves to single-particle states.

The single-particle states of any system are given by the solutions of the eigenvalue problem

$$H\psi(\mathbf{r}) = E\psi(\mathbf{r}), \tag{1.1}$$

where $H$ is the Hamiltonian operator, $E$ are the energy eigenvalues and $\psi(\mathbf{r})$ are the eigenfunctions. The quantity $|\psi(\mathbf{r})|^2$ gives the probability of finding the particle at any point $r$ in space. The perfect lattice is invariant under any translation by

$$\mathbf{R} = l_1\mathbf{a}_1 + l_2\mathbf{a}_2 + l_3\mathbf{a}_3, \tag{1.2}$$

where $(\mathbf{a}_1, \mathbf{a}_2, \mathbf{a}_3)$ are the primitive vectors which define the Bravais lattice, and $(l_1, l_2, l_3)$ run over all integer values. The Hamiltonian for the perfect lattice is also invariant under any translation by $\mathbf{R}$.

Intuitively, it seems resonable that the normal modes in a perfect crystal of infinite extent are plane waves propagating through the material. Let us now investigate how the symmetry of the lattice leads us to this conclusion[3]. Consider the set of translation operators $T(\mathbf{R})$ whose effect is to displace any function through the distance $\mathbf{R}$:

$$T(\mathbf{R})f(\mathbf{r}) = f(\mathbf{r}+\mathbf{R}). \tag{1.3}$$

Since the Hamiltonian is invariant under a translation by $\mathbf{R}$, then the commutator $[T(\mathbf{R}), H] = 0$. Therefore, these two operators can be simultaneously diagonalized, *i.e.* the eigenfunctions of $T(\mathbf{R})$ can also be used as the eigenfunctions of $H$. The eigenvalue problem for $T(\mathbf{R})$ can be written as

$$T(\mathbf{R})g(\mathbf{r}) = C(\mathbf{R})g(\mathbf{r}), \tag{1.4}$$

where $C(\mathbf{R})$ are the eigenvalues and $g(\mathbf{r})$ are the eigenfunctions. Since $T(\mathbf{R}_1 + \mathbf{R}_2) = T(\mathbf{R}_1)T(\mathbf{R}_2)$, this implies that $C(\mathbf{R}_1 + \mathbf{R}_2) = C(\mathbf{R}_1)C(\mathbf{R}_2)$ or that $C(n\mathbf{R}) = C^n(\mathbf{R})$. One solution of these equations is given by $C(\mathbf{R}) = \exp(i\mathbf{k}\cdot\mathbf{R})$ for any value of $\mathbf{k}$. The eigenvalues and eigenfunctions of $T$ are labelled by this $\mathbf{k}$-value, and Eq. (1.4) can be rewritten as

$$T(\mathbf{R})g_{\mathbf{k}}(\mathbf{r}) = g_{\mathbf{k}}(\mathbf{r}+\mathbf{R}) = \exp(i\mathbf{k}\cdot\mathbf{R})g_{\mathbf{k}}(\mathbf{r}). \tag{1.5}$$

Now, by writing the eigenfunctions in the form

$$g_{\mathbf{k}}(\mathbf{r}) = \exp(i\mathbf{k}\cdot\mathbf{r})u_{\mathbf{k}}(\mathbf{r}) \tag{1.6}$$

we find that $u_{\mathbf{k}}(\mathbf{r}+\mathbf{R}) = \exp[-i\mathbf{k}\cdot(\mathbf{r}+\mathbf{R})]g_{\mathbf{k}}(\mathbf{r}+\mathbf{R}) = \exp(-i\mathbf{k}\cdot\mathbf{r})g_{\mathbf{k}}(\mathbf{r}) = u_{\mathbf{k}}(\mathbf{r})$. Thus, the eigenfunctions of $T(\mathbf{R})$ and of $H$ are of the form Eq. (1.6) where $u_{\mathbf{k}}(\mathbf{r})$ is a periodic function of $\mathbf{r}$. For a homogeneous material of infinite extent, the values of $\mathbf{k}$ must be real in order that the wavefunction remain bounded. The

**k**-vector now labels the solutions for the eigenstates of the perfect crystal, and Eq. (1.1) can be rewritten as

$$H\psi_{\mathbf{k}}(\mathbf{r}) = E_{\mathbf{k}}\psi_{\mathbf{k}}(\mathbf{r}), \tag{1.7}$$

where the eigenfunctions $\psi_{\mathbf{k}}(\mathbf{r})$ are simply plane waves $\exp(i\mathbf{k}\cdot\mathbf{r})$, modulated by some periodic function $u_{\mathbf{k}}(\mathbf{r})$. This result is known as Bloch's theorem[3].

Let us now examine some energy levels in a real material. Figure 1.2(a) shows the calculated electronic band structure for GaP. The figure shows the energy of the states as a function of the wave-vector **k**. The labels Γ, X, L, U, and K on the abscissa refer to particular values of **k** in the first Brillouin zone. The labels in the figure refer to the symmetry of the eigenfunctions. Many energy bands are shown. There are an infinite number of bands for the electrons. The top of the valence band is at the point labelled $\Gamma_{15}$, occurring at $\mathbf{k} = \Gamma$ and $E = 0$. The bottom of the conduction band is labelled $X_1$, occurring at $\mathbf{k} = X$ and $E = 2.4$ eV. In the energy gap between these bands, no states of the perfect crystal occur. The electronic defect states we will be studying here occur in this energy gap. In Fig. 1.2(b) we show experimentally determined dispersion curves for phonons in GaP. The labelling of the curves is similar to that in Fig. 1.2(a). There are six branches; three acoustic branches at low energy and three optical branches at high energy. These branches are separated by an energy gap in the region 30–40 meV. The defect vibrational modes we will be studying here may have their energies above the optical branches (split-off modes), in the energy gap (gap modes), or in the bulk bands (resonant modes).

### 1.2.2 States of the Imperfect Lattice

Let us now consider the effect of introducing a defect into the material. We expect two types of states for this imperfect system. First, the states for the perfect system (bulk states) will be modified by the presence of the defect.

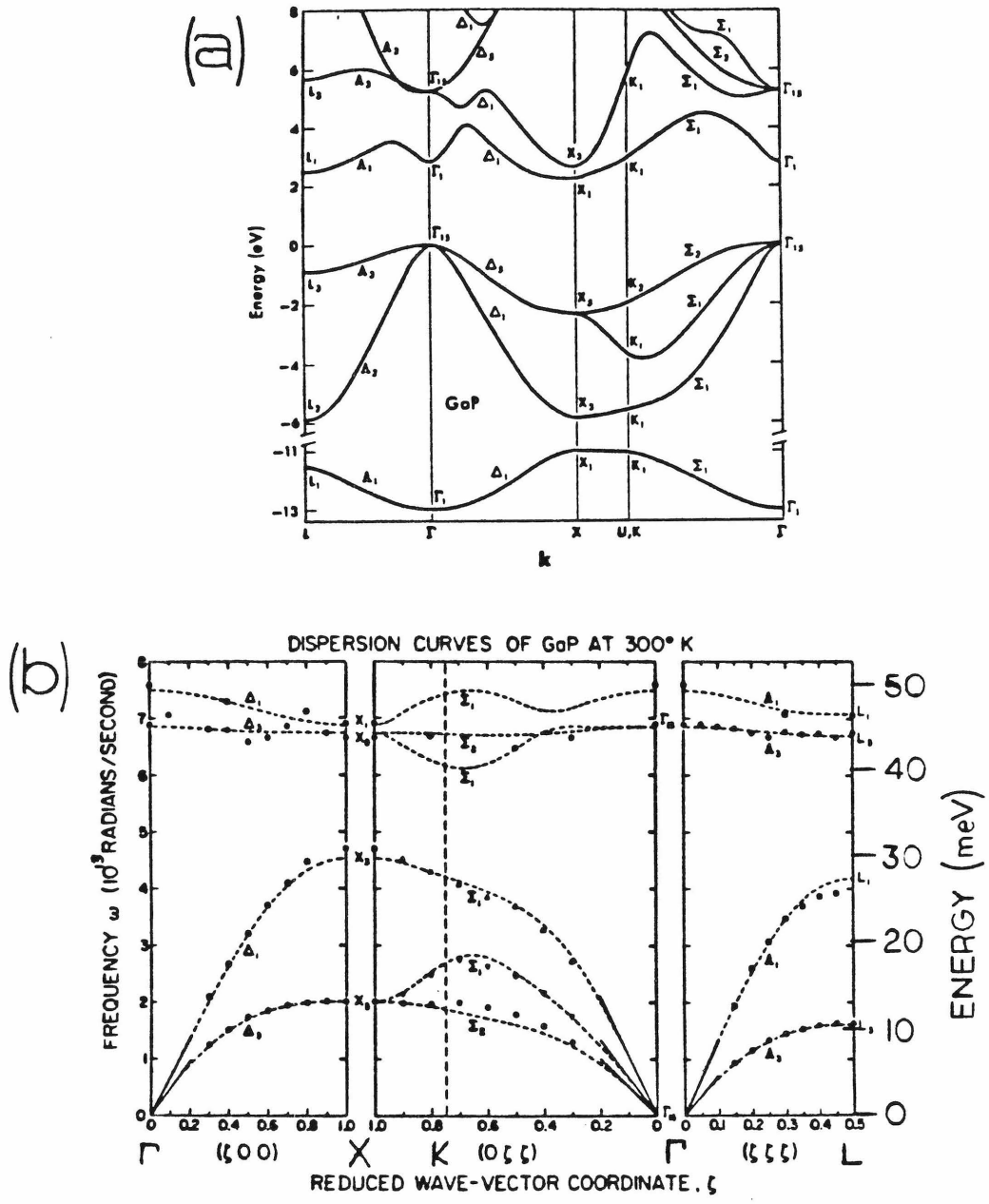


**Figure 1.2:** Electronic and vibrational states in GaP. The energy of the states is plotted as a function of the wave-vector $\mathbf{k}$ along various directions in the first Brillouin zone. (a) Computed electron states. The top of the valence band occurs at $\mathbf{k} = \Gamma$ and $E = 0$. The bottom of the conduction band occurs at $\mathbf{k} = X$ and $E = 2.4$ eV. (After J. P. Walter and M. L. Cohen, *Phys. Rev.* **183**, 763, 1969). (b) Measured phonon states. Longitudinal modes are shown by squares, and transverse modes by circles. Modes whose polarizations are not determined by symmetry are indicated by triangles. The dashed lines represent a shell model fit to the data. (After J. L. Yarnell, J. L. Warren, R. G. Wenzel, and P. J. Dean, in *Neutron Inelastic Scattering*, (IAEA, Vienna, 1968), Vol. 1, p. 301).

Second, the defect may introduce new states in those energy regions where no bulk states occur. In those regions of the crystal not affected by the defect, the solutions for the states should be similar to those discussed above for the perfect crystal, *i.e.* eigenfunctions given by $\exp(i\mathbf{k}\cdot\mathbf{r})u_k(\mathbf{r})$. However, now we have a defect in the material, and so we must allow complex values of $\mathbf{k}$ in the solutions. In regions of energy which are forbidden to the bulk states, the $\mathbf{k}$-values for the imperfect crystal states will be purely imaginary. This leads to decaying exponentials for the defect modes. These types of states are known as *localized* states of the defect. The wavefunction for these states falls to zero as one proceeds away from the defect. In those energy regions where we have bulk states, there may also be certain states which are caused by the defect. These states are characterized by a peak in the wavefunction in the vicinity of the defect. For electrons, this corresponds to a larger charge density around the defect. For phonons, the amplitude of vibration near the defect is significantly greater than that far removed from the defect. These types of states are known as *resonant* states, since their energy is resonant with modes of the bulk crystal. We will use the term defect modes to refer to both of these types of states associated with crystal defects.

The states of the perfect lattice are labelled by their $\mathbf{k}$-vector, which arose directly from the translational symmetry of the lattice. With a defect in the crystal, the translational symmetry is lost. What remains is the point group symmetry, with the defect as the origin in space. For substitutional defects in zinc-blende lattices this point group symmetry is $T_d$. The eigenstates of the defect will now be labelled by the irreducible representations of the $T_d$ group; $A_1$, $A_2$, $E$, $T_1$, and $T_2$. These labels give the degeneracy the levels and specify the nature of the eigenfunctions. The theoretical problem of describing defect states consists

in part of dividing those bulk states labelled by **k** into their various components which are labelled by $A_1$, $A_2$, $E$, $T_1$, and $T_2$. These states then form bases with which we construct the states of the imperfect crystal. The calculations presented in Chapter 5 explicitly demonstrate this decomposition, for the case of vibrational states in GaP.

Let us now consider some specific types of point defects in semiconductors. Perhaps the most common types of defects are donor and acceptor impurities. A donor atom has one extra electron and one extra proton relative to the host atom it replaces. All of the bonds in the material are satisfied without this extra electron. The core of the donor appears as a single positive charge, and the extra electron resides in a hydrogenic-type orbit around the donor core. The ground state of the electron is an $s$-like ($A_1$) state, with a binding energy given by effective-mass theory[4] to be

$$E = \frac{m^* e^4}{2\hbar^2 \epsilon^2}, \tag{1.8}$$

where $m^*$ is the effective-mass of the electron. In GaP, effective-mass donor binding energies are 14 meV, corresponding to a Bohr radius of 45 Å. At room temperature, most of the donor-bound electrons are thermally ionized to the conduction band states where they carry current. An acceptor impurity in a semiconductor has one less electron and one less proton than the atom it replaces. In analogy with the donors, these acceptors will bind a hole in a hydrogenic-type orbit. At room temperature these holes are ionized into the valence band where they carry current. The energy levels produced by acceptors and donors are known as *shallow* levels since they are very near to the edges of the bands.

Many defects in semiconductors produce electronic energy levels which are in the middle of the energy gap. Such levels are known as *deep* levels[5]. These levels may be associated with changes in the charge density of the actual bonds

in the crystal. Whereas a shallow level impurity does not produce significant changes in the bonds, a deep level impurity often does. Typical examples of defects which produce deep levels are vacancies, anti-site defects, and interstitial impurities. Deep levels may also be formed by impurities which, according to their position in the periodic table, should form shallow levels. One example of this is oxygen in GaP. The electronic energy levels of this impurity have been extensively studied[5—9], and are still the subject of much controversy. The wave-function of a deep level is quite localized around the defect. The nature of the wave-function can be similar to molecular-orbitals formed by the bonds associated with the defect and its neighbors. Electronic transitions at the defect may produce significant changes in the configuration of the atoms. This leads to large electron-phonon coupling, which is a characteristic trait of many deep level impurities.

Many defects in semiconductors will produce significant changes in the vibrational states of the system. The defect phonons which are formed may be either localized or resonant. It is well-known that an impurity with small mass will produce a localized mode split-off from the bulk modes. A heavy mass impurity will produce resonant modes. An impurity with significantly different bond strengths compared to the bulk may have many types of vibrational modes. As discussed above, the bonds of a deep level impurity can be significantly different from those of the bulk material. Therefore, those impurities which produce deep levels will also tend to produce defect phonons, and these phonons are observed in experiment.

## 1.3 Observation of the States using Photoluminescence

### 1.3.1 Donor-Acceptor Luminescence

Defects in semiconductors will often tend to cluster together to form defect complexes. One simple complex which commonly occurs is a donor-acceptor pair, consisting of one donor impurity and one acceptor impurity. As discussed above, the core of a donor appears to be positive, and the core of an acceptor appears to be negative, relative to the atoms which they replace. Thus, there exists an attractive Coulomb interaction between the acceptor and donor impurity cores, and they tend to form pairs. There are certain discrete lattice sites on which the impurities may reside, and this results in a series of discrete separations between the donor and acceptor. We refer to these separations as *shells* and label them by $m$; $m = 1$ for first-nearest-neighbor pairs, $m = 2$ for second-nearest-neighbor pairs, *etc.* At zero temperature, in thermal equilibium, all of the pairs would be nearest-neighbor $m = 1$ pairs (this state is never achieved of course). At elevated temperatures, some of the the pairs will have $m > 1$. The number of pairs of each possible separation can be computed using a statistical model of oppositely-charged centers in equilibrium at some specified temperature[10]. At a typical crystal growth temperature of 1000 K, roughly 10% of the pairs are nearest-neighbor.

As long as a pair of donor and acceptor impurities are not too close together, they will still bind their respective electron and hole. This electron and hole may recombine, producing a photon. If the impurites are far enough separated so that their wavefunctions do not overlap, then the energy of this photon can be estimated by the following simple model. In the initial state we have a bound-electron and bound-hole, together with two neutral (noninteracting) impurities. The energy of this state will be the band-gap minus the sum of the donor and

acceptor binding energies, $E_g - (E_D + E_A)$. In the final state there are two oppositely-charged centers separated by some distance $r_m$, with an interaction energy of $-e^2/\epsilon r_m$ where $\epsilon$ is the dielectric constant of the material. Thus, the luminescence energy is given by[11]

$$h\nu_m = E_g - (E_D + E_A) + \frac{e^2}{\epsilon r_m}. \tag{1.9}$$

Even though we have derived this formula under the assumption that the impurities are far separated, it actually works remarkably well for closer pairs of impurities also. The result is a whole series of luminescence lines, one for each possible donor-acceptor separation (shell). This phenomenon is known as donor-acceptor (DA) luminescence. It was first observed about twenty years ago, and has since been studied in great detail by many workers[12]. The energy of the observed luminescence lines has provided us with some of the most accurate measurements of impurity binding energies and the dielectric constant of the bulk material. The observed spectra also provided some of the first information about which particular site a given impurity was residing on. The intensity of the luminescence lines is related to the number of possible sites in the various shells. Inequivalent sites in a given shell will result in line-splitting and this produces fine structure on the DA spectrum.

Figure 1.3 shows an example of donor-acceptor luminescence. The material under study is GaP, doped with Zn and O impurities. The Zn atom substitutional for P is a shallow acceptor, and the O atom substitutional for P is a deep donor. Together, they produce DA luminescence in the manner described above. The spectrum shown in Fig. 1.3 was obtained at 1.6 K, using above-band-gap continuous $Ar^+$ laser excitation. We see a series of luminescence lines. These lines are labelled by $(m)$ for $m^{th}$-nearest-neighbor pairs, with a superscript indicating the type of phonon involved in the transition. These phonons will

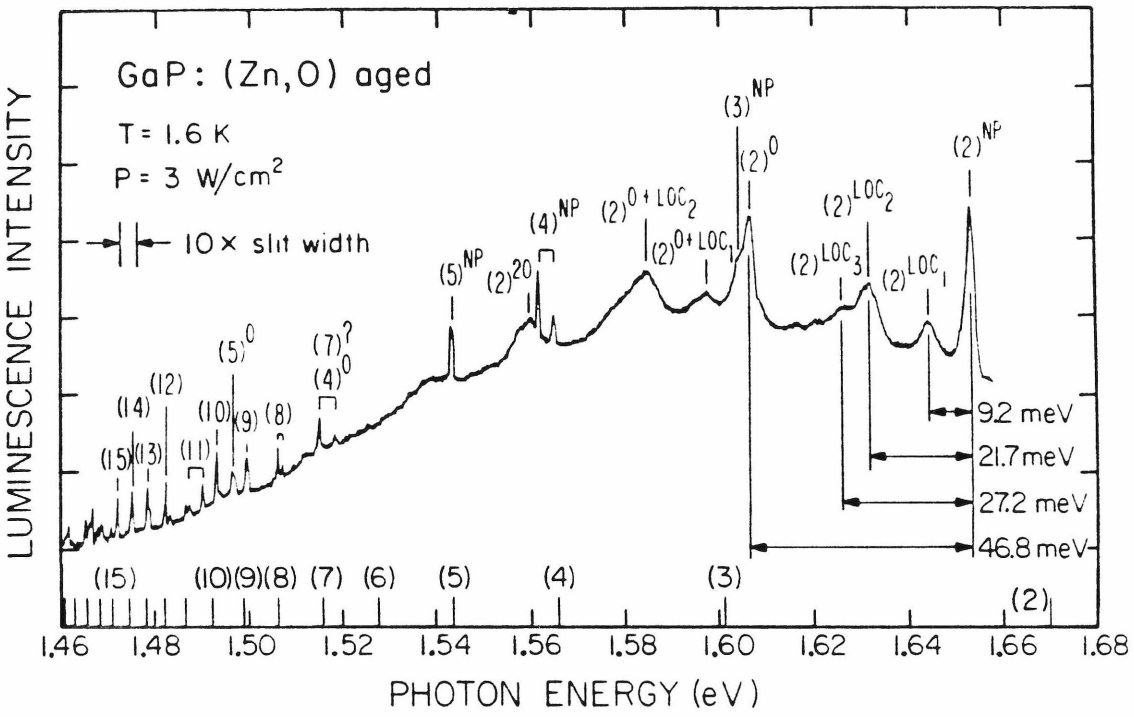


**Figure 1.3:** Low temperature donor-acceptor pair luminescence from GaP containing (Zn,O) pairs. The lines are labelled by $(m)$ for $m^{th}$-nearest-neighbor pairs, with a superscript indicating the type of phonon involved in the transition (O=optical, LOC=local, NP=no-phonon). Those labels with no superscripts refer to no-phonon transitions. Theoretical predictions for the line positions are shown on the abscissa.

be discussed in the following section, and let us for now examine those sharp luminescence lines with $m \geq 4$. As expected, we observe a luminescence line for each possible separation of donor and acceptor. The lines in the spectrum were identified from the work of previous authors[13], and also by comparing their observed energy with the theoretical predictions from Eq. (1.9) shown on the abscissa (the details of this calculation will be discussed in Chapters 2 and 3). The agreement between experiment and theory is very good for the further separated pairs, and there are sufficiently few of the close pairs to make their identification possible. Some splittings of the lines are observed (*e.g.* for $m = 4$, 8 and 11). This is due to inequivalent sites in a given shell. Actually, on the basis of Fig. 1.3 alone, one might not be able to identify all of the lines. But when observations are made versus laser power, temperature, and for many different samples, the identification eventually becomes quite certain.

In this thesis, we are not so much interested in the phenomenon of donor-acceptor luminescence itself. Rather, we use the phenomenon as a technique for monitoring the relative positions of Zn and O impurities in GaP. In this way, we have a microscopic probe of the impurity positions in the sample. Movement of the impurities is seen directly as a shift in the luminescence energy. We are able to observe reactions in which the impurity atoms diffuse through the material under conditions of photo-excitation. These "defect reactions" are discussed in detail in Chapter 3.

### 1.3.2 Phonon-Assisted Luminescence

When an electron and hole recombine at a defect, their energy may be emitted in the form of a photon (*i.e.* luminescence). However, the defect may be left in some excited vibrational state in the final state of the electronic transition. In that case, the emitted photon will be reduced in energy by the amount of the

vibrational energy. We can view this process as the emission of one of more phonons. What will be observed in the luminescence spectrum is a series of luminescence lines. The highest energy line (the no-phonon line) is due to the emission of a photon and no phonons. The lower energy lines (phonon-assisted lines) are due to the emission of a photon and some phonons. The energy of these lines will be shifted from the no-phonon line by the energy of the phonon(s) involved. If the defect level is shallow, so that the carrier wavefunctions are quite extended in space, then the phonons which may be excited will generally be characteristic of the bulk material. Alternatively, if the defect level is deep, so that the wavefunction is quite localized, then the vibrational modes will be characteristic of the defect itself *i.e.* defect phonons.

An example of these phonon-assisted luminescence lines is given in Fig. 1.3. As discussed in the previous section, the defects which produced the luminescence shown in this figure are actually $m^{th}$-nearest-neighbor pairs of Zn and O impurities in GaP. The lines are labelled by $(m)$, with a superscript indicating the type of phonon involved in the transition (NP=no-phonon, LOC=local phonon, O=optical phonon). Let us consider the second-nearest-neighbor lines. The no-phonon line is labelled by $(2)^{\mathrm{NP}}$. A number of phonon replicas of this line are visible. The lines labelled $(2)^{\mathrm{LOC}_1}$, $(2)^{\mathrm{LOC}_2}$, and $(2)^{\mathrm{LOC}_3}$ are due to excitations of defect phonons of the second-nearest-neighbor (Zn,O) complex. The line labelled $(2)^{\mathrm{O}}$ is probably due the excitation of the bulk optical phonon. Similarly the lines labelled $(2)^{\mathrm{O+LOC}_1}$, *etc.* are due to the excitation of two phonons in the final state of the electronic transition. These identifications will be discussed in greater detail in Chapter 3. All we wish to note here is that these phonon-replicas do indeed exist in the luminescence spectra, and they contain some information about the vibrational modes of the defect and of the bulk.

## 1.4 Summary of Thesis

### 1.4.1 Periodicity in the Undulation Spectra of GaP:N

In Chapter 2 of this thesis, we will consider some of the geometrical aspects of the relative positions of donor-acceptor pairs in the crystal lattice. This is a fairly brief chapter, and it is meant to serve as an introduction to the subject of donor-acceptor pairs, which will be investigated further in Chapter 3. The original results of Chapter 2 are purely mathematical. We use these results to give a very simple geometrical interpretation of an observed physical phenomenon. We consider the calculation of the distribution of donor-acceptor site separations. For very close pairs, the number of sites in each shell can be counted from a physical model; for the zinc-blende structure we are considering, there are 4 first-nearest neighbors, 12 second-nearest-neighbors, 12 third-nearest-neighbors, *etc.* By using some numerical model to generate the appropriate lattice, a procedure can easily be implemented on a computer to count the number of sites in any given shell. The results from such a calculation are tabulated in Chapter 2. The donor-acceptor separation in each shell, and the DA luminescence energies fom Eq. (1.9) are also given.

For quite far separated DA pairs, the discrete distribution of sites becomes a rather wildly fluctuating quantity. For example, there are 72, 120, 60, and 48 sites in the $m = 97, 98, 99$, and $m = 100$ shells respectively. The averaged number of sites in each shell will vary simply like $4\pi r^2$, but the fluctuations around this quantity appear to be quite random. However, when one actually computes the averaged number of sites in each shell, we find quite regular oscillations in this quantity. These oscillations were first observed by Street and Wiesner[14], who associated them with undulations observed in the DA luminescence spectra of GaP doped with N (a donor) and various acceptors. Street and Weisner observed

that oscillations in the distribution of donor-acceptor site separations existed, and they speculated that these oscillations were purely random in origin. In Chapter 2 we derive an analytic form for the distribution of donor-acceptor site separations, and we show that it is composed of a series of functions which are approximately periodic in $r$. This periodicity is shown to arise directly from the long-range order of the lattice. In this way we show that the observed undulations in the GaP:N spectra are due to the crystal symmetry, and how in principle the symmetry of the lattice could be deduced from the spectra.

### 1.4.2 Defect Reactions in GaP:(Zn,O)

Chapter 3 forms the major part of this thesis. Here we will be considering phenomena involving Zn (an acceptor) and O (a donor) impurities in GaP. When the Zn and O atoms occupy nearest-neighbor lattice sites, they produce donor-acceptor luminescence in the red part of the spectrum[15,16]. Consequently, this material has been used for making red-light-emitting-diodes. When operated under forward bias, the performance of these diodes is observed to decay with time[17]. This study provides a microscopic explanation for this degradation; namely, that the nearest-neighbor (Zn,O) pairs dissociate and subsequently reform as further separated pairs. This reaction can be written as

$$(\mathrm{Zn,O})_{m=1} \rightarrow (\mathrm{Zn,O})_{m>1}\,. \tag{1.10}$$

The observation and identification of this reaction is the main result of this thesis. The dissociation of the nearest-neighbor pairs can occur by a photoinduced mechanism. Such a process of photoinduced reactions among defects of known chemical type has not previously been observed in a semiconductor. The phenomenon of donor-acceptor luminescence is used here to observe the motion of the impurities directly, in terms of a shift in the luminescence energy. This is the first time donor-acceptor luminescence has been used as a microscopic probe

of defect reactions. In Chapter 3, high temperature photoluminescence spectra are presented which show this reaction in progress. Low temperature spectra are displayed in order to clearly identify the initial and final states of the reaction.

We have identified the mechanism for the photoinduced pair dissociation by performing measurements of the reaction rate versus laser power and temperature. The dissociation rate of the nearest-neighbor pairs is deduced using a model for the electron-hole recombination kinetics which includes the effects of high carrier occupation (saturation) and spatially varying carrier generation. The activation energy for the photoinduced reaction is found to be $0.60 \pm 0.07$ eV with a pre-exponential factor of about $3 \times 10^4$ $s^{-1}$. The dissociation of the nearest-neighbor (Zn,O) pairs can also occur by purely thermal mechanisms. From annealing studies, the activation energy for thermal dissociation of the pairs is estimated to be $2.6 \pm 0.6$ eV with a pre-exponential factor of roughly $10^{10}$ $s^{-1}$. From these values, the photoinduced pair dissociation is identified as a "recombination-enhanced defect reaction". In the reaction, nonradiative electron-hole recombination puts the defect into a highly excited vibrational state, leading to the dissociation of the pair.

Although recombination-enhanced reactions have been previously observed in semiconductors[19], the chemical identity of the defects in those studies was unknown. In this work, we know that the defect involved is a (Zn,O) pair. This knowledge makes our work unique, and enables us to study in greater detail the microscopic mechanism for the observed pair dissociation. In Chapter 3 it is argued that a strong electron-phonon interaction is responsible for the reactions. This interaction is clearly evident in the intense phonon replicas which are present in the photoluminescence spectra. Ultimately, a detailed understanding of these defect phonons should lead to a greater understanding of the reactions. The

calculations presented in Chapter 5 represent the first step in an analysis of these defect phonons.

### 1.4.3 Exciton Capture Cross Sections in Si:In,B

Free electrons and holes in semiconductors can interact to form a variety of multi-particle complexes. These complexes represent a breakdown of the single-particle picture for the electronic states. In Chapter 4, we will discuss the properties of some of these complexes, namely, free excitons and bound excitons. A free electron and hole will experience an attractive Coulomb interaction, and they will bind to form a free exciton. These free excitons may in turn bind onto impurities in the crystal to form bound excitons. Electron-hole recombination of an exciton results in luminescence. The energy of the luminescence is characteristic of the particular type of exciton involved. In silicon, we observe bound excitons consisting of a free exciton bound onto a neutral donor or acceptor. The study described in Chapter 4 deals with the properties of excitons bound onto In and B acceptors in Si.

The intensity of bound exciton luminescence is proportional to the concentration of impurities in the material. Therefore, it seems reasonable that we may use this luminescence as a technique for measuring the impurity concentrations[20]. To quantitatively relate the luminescence intensity to the impurity concentration requires detailed knowledge of all the exciton kinetics (generation, capture, release, and recombination) in the system. In Chapter 4, we study the process by which free excitons are captured onto impurities to form bound excitons. From observed lifetimes of luminescence lines, we deduce the cross sections for free exciton capture onto In and B impurities. We find that at low temperature the In cross section is much larger than that of B. This is rather surprising since the excitons are more tightly bound to In than B, and hence

should have a smaller cross section. We conclude that excited states of the In bound exciton exist, and capture into these excited states produces the observed large capture rates.

The kinetics of excitons in semiconductors is very similar to the kinetics involved with single carriers (electrons or holes). In this way, the kinetic considerations in Chapters 3 and 4 are related. There is however one important difference between the results presented in these two chapters. In Chapter 3, we are in the regime of high laser powers, in which the the (Zn,O) centers are almost always occuppied by electrons (*i.e.* the centers are saturated). In that case, a change in laser power results in almost no change in luminescence intensity (or in pair dissociation rate). In Chapter 4, we are in the limit of low laser powers, in which the exciton occupation of the impurities varies linearly with power. In both cases, it was not obvious *a priori* what laser power levels were suitable to use in the experiments. Only after careful observation over a very wide range of powers were the appropriate ranges for the laser powers in each type of experiment determined.

### 1.4.4 Vibrational Modes of Oxygen in GaP

The photoluminescence spectra of defects in semiconductors often contain information about the vibrational modes of the defects. A good example of this behavior is found in the oxygen defect in GaP. The photoluminescence spectra of GaP:O display a very large amount of phonon coupling[2,6]. In Chapter 5, we present theoretical calculations which were undertaken in an effort to understand the vibrational modes of substitutional defects in zinc-blende lattices. The results are applied to the case of oxygen in GaP. For the charge state $O^+$, two resonant vibrational modes are observed in experiment. On the basis of our calculations we identify these as being a $A_1$ breathing mode, and a $T_2$ motion of the oxygen

atom itself. Furthermore, on the basis of the observed energies of the modes we find that the O-Ga spring constants are roughly 50% of the bulk P-Ga spring constants, which suggests that O in GaP is a weakly bonded defect. This weak bonding has implications to the dissociation of the (Zn,O) pairs discussed in Chapter 3, since it indicates that it may be the oxygen atom which moves in the dissociation rather than the zinc atom.

The technique of Green's functions is widely used in solid-state physics to compute the properties of defects in crystals, and in particular it has been used for computing the vibrational modes of defects[21,22]. This technique is used in Chapter 5 to treat the vibrational modes of point defects. The first step in the computation is to calculate the phonon bands of the perfect crystal. The defect is then introduced as a localized perturbation, and the vibrational modes of the imperfect crystal are evaluated. In all of our calculations the spring constants of the bulk crystal and of the defect are treated as parameters. The bulk spring constants are chosen to fit the actual phonon bands. The defect spring constants are unknowns, and the defect phonons are computed as a function of these unknowns. The quantity which effectively describes the vibrational modes of a defect is the *local density-of-states*. Localized modes show up as $\delta$-functions in the local density-of-states, and resonant modes appear as peaks with some nonzero width. In Chapter 5, we will emphasize the investigation of resonant vibrational modes, since it is these modes which are observed in experiment.

## REFERENCES


1. W. A. Harrison, *Electronic Structure and the Properties of Solids*, (Freeman, San Francisco, 1980).
2. R. M. Feenstra and T. C. McGill, *Phys. Rev.* **47**, 925 (1981).
3. N. W. Ashcroft and N. D. Mermin, *Solid State Physics*, (Holt, Rinehart and Winston, New York, 1976), p. 134.
4. F. Bassani and G. P. Parravicini, *Electronic States and Optical Transitions in Solids*, (Pergamon, Oxford, 1975).
5. M. Jaros, *Advances in Physics* **29**, 409 (1980).
6. P. J. Dean and C. H. Henry, *Phys. Rev.* **176**, 928 (1968).
7. T. N. Morgan, *Phys. Rev. Lett.* **40**, 190 (1978).
8. B. Monnemar and L. Samuelson, *Phys. Rev.* **18**, 809 (1978).
9. G. A. Baraff, E. O. Kane, and M. Schulter, *Phys. Rev. Lett.* **47**, 601 (1981).
10. J. S. Prener, *J. Chem. Phys.* **25**, 1294 (1956).
11. J. J. Hopfield, D. G. Thomas, and M. Gershenzon, *Phys. Rev. Lett.* **10**, 162 (1963).
12. F. Williams, *Phys. Stat. Sol.* **25**, 493 (1968).
13. P. J. Dean, C. H. Henry, and C. J. Frosch, *Phys. Rev.* **168**, 812 (1968).
14. R. A. Street and P. J. Wiesner, *Phys. Rev. Lett.* **34**, 1569 (1975).
15. T. N. Morgan, B. Welber, and R. N. Bhargava, *Phys. Rev.* **166**, 751 (1968).
16. C. H. Henry, P. J. Dean, and J. D. Cuthbert, *Phys. Rev.* **166**, 754 (1968).
17. P. D. Dapkus and C. H. Henry, *J. Appl. Phys.* **47**, 4061 (1976).
18. A. Onton and M. R. Lorenz, *Appl. Phys. Lett.* **12**, 115 (1968).
19. D. V. Lang and L. C. Kimerling, *Phys. Rev. Lett.* **33**, 489 (1974).
20. G. S. Mitchard and T. C. McGill, *Appl. Phys. Lett.* **37**, 959 (1980).
21. A. A. Maradudin, *Rep. Prog. Phys.* **28**, 331 (1965).

22. S. T. Pantelides, *Reviews of Modern Physics* **50**, 797 (1978).

# CHAPTER 2

# PERIODICITY IN THE UNDULATION SPECTRA OF GaP:N

## 2.1 INTRODUCTION

### 2.1.1 Undulation Spectra of GaP:N

Donor-acceptor (DA) pairs in semiconductors produce a variety of interesting luminescence spectra. As discussed in Section 1.3.1, the energy of luminescence emitted from a pair depends on the separation of the impurities. Thus, a luminescence spectrum provides information about the number of pairs of each possible separation. The different separations of the impurities are referred to as *shells*, and labelled by $m$; $m = 1$ for first-nearest-neighbors, $m = 2$ for second-nearest-neighbors, *etc.* The intensity of the luminescence lines is affected by the number of sites in each shell. For example, in the DA spectrum shown in Fig. 1.3, the intensity of each discrete line ($m$) is determined in part by the number of sites in the $m^{th}$ shell. For far separated DA pairs (say $m \gtrsim 30$), the luminescence lines from adjacent shells start to overlap and smear together to form a band. The luminescence spectrum of GaP:N co-doped with acceptors displays this sort of luminescence band[1—5]. Nitrogen substituting for phosphorous in GaP is an unusual type of donor. When N is paired with acceptors, they produces a unique type of DA luminescence. Since N is isoelectronic with P, this DA luminescence does not follow Eq. (1.9), but the luminescence energy still has some dependence on the donor-acceptor separation.

The DA luminescence spectrum of GaP:(N,acceptor) displays approximately periodic undulations[1]. A variety of explanations have been proposed for this undulatory behavior[2—5], including an "interference effect" of the carrier wavefunctions at the N and acceptor sites, and "rotational levels" of the acceptor wavefunction. . Finally, it was shown by Street and Wiesner[5], the undulatory behavior of the spectrum results from the properties of $N(r)$, the distribution of acceptor sites located a distance $r$ from the donor site. It turns out that the *averaged*

number of sites in each donor-acceptor shell displays quite regular oscillations as a function of $r$. Street and Wiesner observed that fluctuations in $N(r)$ existed, and they speculated that these fluctuations were purely random in origin. Here we will show that oscillatory nature of $N(r)$ is in fact due to the long-range symmetry of the crystal lattice.

### 2.1.2 Results of this Work

The original results of this work are purely mathematical. We derive an analytic form for $N(r)$, the distribution of donor-acceptor site separations. We show that $N(r)$ is composed of a series of functions which are approximately periodic in $r$. The period of the oscillations is given by $2\pi/|\mathbf{G}|$, where $\mathbf{G}$ is a reciprocal lattice vector. This period equals the perpendicular separation of those lattice planes labelled by $\mathbf{G}$. This leads us to the following geometrical interpretation for the periodic behavior of $N(r)$: consider a sphere of radius $r$ centered at the donor site. As $r$ increases the sphere intersects new lattice planes. The total number of points $L(r)$ enclosed by the sphere will show a sharp increase each time a new plane is intersected, and $N(r) = dL(r)/dr$ will show a corresponding peak. Thus, $N(r)$ will show oscillatory behavior with period given by the lattice plane spacing. In particular, the low frequency oscillations in $N(r)$ result from lattice planes of high symmetry ( (100), (110), etc. ) .

### 2.1.3 Outline of Chapter

In this chapter we will mainly be considering the geometrical aspects of donor-acceptor pair luminescence. The donor-acceptor pairs in the lattice are divided into shells, the radius of a shell corresponding to the separation of the donor and acceptor sites. Section 2.2.1 presents this shell-decomposition for the case of a zinc-blende lattice. We consider the number of different sites in each shell. This quantity is just the discrete analogue of $N(r)$ discussed above. In

Section 2.2.2 we present a numerical computation of $N(r)$. The purpose of this computation is mainly to make a connection with the work of other authors[5]. Finally, in Section 2.2.3 we present the major result of this work: an analytic form for $N(r)$. We discuss the connection between this formula and the observed luminescence spectra in GaP:N. Our conclusions are presented in Section 2.3.

## 2.2 THE DISTRIBUTION OF DONOR-ACCEPTOR SITE SEPARATIONS

### 2.2.1 Geometrical Considerations

Let us take our origin in space to be a donor site in the lattice. Then the set of all possible acceptor sites can be divided into shells, each shell corresponding to a particular donor-acceptor separation. Let us denote the number of sites in a shell by $N_m$, where $m$ labels the shell ($m = 1$ for first-nearest-neighbor, *etc.*). $N_m$ is the discrete distribution of donor-acceptor site separations. The continuous distribution $N(r)$ is related to $N_m$ by

$$N(r) = \sum_m N_m \, \delta(r - r_m), \tag{2.1}$$

where $r_m$ is the radius (donor-acceptor separation) of the $m^{th}$ shell.

Let us now consider the donor-acceptor shells for (N,acceptor) pairs in GaP. The GaP lattice has the zinc-blende structure, consisting of two face-centered-cubic (fcc) sublattices offset by $a_0(1/4, 1/4, 1/4)$ where $a_0$ is the lattice constant (length of a cube face). The Ga atoms reside on one fcc sublattice and the P atoms on the other. The nitrogen donors substitute for P atom, and the acceptor impurities substitute for a Ga atom. This situation with the impurities on different sublattices is known as a type-II geometry[6]. The coordinates of a displaced fcc lattice in units of $a_0/4$ can be generated by the set of all integers

$(m_1, m_2, m_3)$ which satisfy:

$$m_1, m_2, m_3 \qquad \text{all odd,} \tag{2.2a}$$

and

$$\frac{m_1 + m_2 + m_3 - 3}{2} \qquad \text{even.} \tag{2.2b}$$

These coordinates define shells, having radius[6]

$$r_m = \frac{a_0}{4}\sqrt{m_1^2 + m_2^2 + m_3^2} \tag{2.3a}$$

$$= \frac{a_0}{4}\sqrt{8m - 5}, \tag{2.3b}$$

where $m = 1, 2, 3, \ldots$ is the shell number. The number of lattice sites in each shell can be computed by finding all the different sets of $(m_1, m_2, m_3)$ which satisfy Eq. (2.2) and which result in the same $m$. Those sets of $(m_1, m_2, m_3)$ in which the elements $m_i$ are just rearranged, or in which the sign of one or more elements is changed, belong to the same subshell. There are 4, 12, or 24 sites in a subshell[7], corresponding to one, two or three different values of $|m_i|$ in $(m_1, m_2, m_3)$. Table 2.1 gives the number of sites and the coordinates of a site in various subshells of the lattice. Also listed in the table are the donor-acceptor separations, Eq. (2.3), and the luminescence energy, Eq. (1.9). The data used in the calculations were for (Zn,O) pairs in GaP; $E_g = 2339$ meV, $E_A = 64$ meV, $E_D = 893$ meV, $\epsilon = 11.1$, and $a_0 = 5.45$ Å. From this table is appears that the number of sites in each shell varies more or less randomly from one shell to the next, especially for large $m$. However, as we will see in the following sections, there is an underlying periodicity in this quantity.

**2.2.2 Numerical Computations**

It is straightforward to numerically compute $N(r)$, where $N(r)dr$ is the number of acceptor sites located a distance between $r$ and $r + dr$ from the donor

**TABLE 2.1:** Type-II donor-acceptor shells. The donor-acceptor separation in the $m^{th}$ shell is denoted $r_m$, and $h\nu_m$ gives the luminescence energy. $N_m$ is the total number of sites in the $m^{th}$ shell. The number of sites in each subshell is denoted by $n_m^i$. $(m_1, m_2, m_3)$ are the coordinates of a site in each subshell.

| $m$ | $r_m$(Å) | $h\nu_m$(meV) | $N_m$ | $n_m^i$ | $(m_1, m_2, m_3)$ |
|---|---|---|---|---|---|
| 1 | 2.360 | 1933.2 | 4 | 4 | ( 1, 1, 1 ) |
| 2 | 4.519 | 1669.9 | 12 | 12 | ( 3, -1, 1 ) |
| 3 | 5.939 | 1601.0 | 12 | 12 | ( 3, 3, 1 ) |
| 4 | 7.080 | 1565.7 | 16 | 4 | ( 3, -3, 3 ) |
| | | | | 12 | ( 5, 1, 1 ) |
| 5 | 8.061 | 1543.4 | 24 | 24 | ( 5, -3, 1 ) |
| 6 | 8.935 | 1527.6 | 12 | 12 | ( 5, 3, 3 ) |
| 7 | 9.730 | 1515.7 | 24 | 12 | ( 5, 5, 1 ) |
| | | | | 12 | ( 7, -1, 1 ) |
| 8 | 10.466 | 1506.3 | 36 | 12 | ( 5, -5, 3 ) |
| | | | | 24 | ( 7, 3, 1 ) |
| 9 | 11.153 | 1498.6 | 12 | 12 | ( 7, -3, 3 ) |
| 10 | 11.800 | 1492.2 | 28 | 4 | ( 5, 5, 5 ) |
| | | | | 24 | ( 7, -5, 1 ) |
| 11 | 12.413 | 1486.8 | 36 | 24 | ( 7, 5, 3 ) |
| | | | | 12 | ( 9, 1, 1 ) |
| 12 | 12.997 | 1482.1 | 24 | 24 | ( 9, -3, 1 ) |
| 13 | 13.557 | 1478.0 | 36 | 12 | ( 7, -5, 5 ) |
| | | | | 12 | ( 7, 7, 1 ) |
| | | | | 12 | ( 9, 3, 3 ) |
| 14 | 14.094 | 1474.3 | 36 | 12 | ( 7, -7, 3 ) |
| | | | | 24 | ( 9, 5, 1 ) |
| 15 | 14.611 | 1471.0 | 24 | 24 | ( 9, -5, 3 ) |
| . | | | | | |
| . | | | | | |
| . | | | | | |
| 97 | 37.832 | 1416.4 | 72 | 24 | ( 19, 17, 11 ) |
| | | | | 12 | ( 19,-19, 7 ) |
| | | | | 12 | ( 23,-11, 11 ) |
| | | | | 24 | ( 25,-11, 5 ) |
| 98 | 38.028 | 1416.2 | 120 | 12 | ( 21, 13, 13 ) |
| | | | | 24 | ( 21,-17, 7 ) |
| | | | | 24 | ( 23,-13, 9 ) |
| | | | | 24 | ( 23, 15, 5 ) |
| | | | | 12 | ( 27, -5, 5 ) |
| | | | | 24 | ( 27, 7, 1 ) |
| 99 | 38.223 | 1416.0 | 60 | 24 | ( 21, 15, 11 ) |
| | | | | 12 | ( 25, 9, 9 ) |
| | | | | 24 | ( 27, -7, 3 ) |
| 100 | 38.417 | 1415.9 | 48 | 24 | ( 25, 11, 7 ) |
| • | | | | 24 | ( 25, 13, 1 ) |
| • | | | | | |
| • | | | | | |

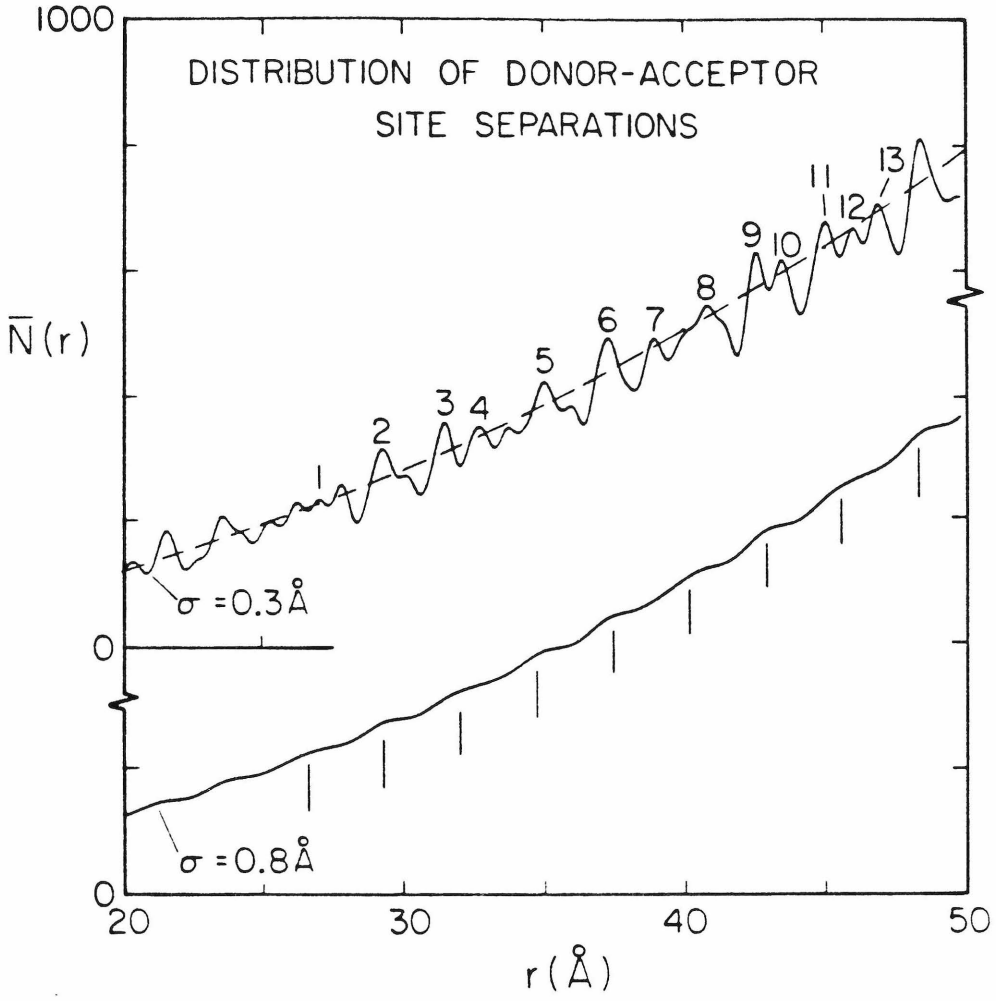


**Figure 2.1:** The broadened distribution $\overline{N}(r)$ of acceptor sites located a distance $r$ from the donor site for (N,acceptor) pairs in GaP. Upper curve: $\sigma = 0.3$ Å broadening with the peaks labelled as in Ref. 5. The dashed line is a plot of $4\pi r^2/V_c$, where $V_c$ is the volume of a unit cell. Lower curve: $\sigma = 0.8$ Å broadening showing the lowest frequency oscillations with period 2.73 Å$= a_0/2$.

site. As shown in Eq. (2.1), $N(r)$ is a series of $\delta$-functions, one for each donor-to-acceptor shell. Experimentally, these discrete lines are broadened. To simulate this line broadening we replace each $\delta$-function by a Gaussian of width $\sigma$. The averaged number of sites $\overline{N}(r)$ is then computed by summing each Gaussian weighted by the number of sites in each shell. Figure 2.1 shows $\overline{N}(r)$ for a type-II spectrum in a zinc-blende lattice (donor and acceptor ions on different sublattices). For a broadening of $\sigma = 0.3$ Å the results are basically identical with those of Street and Wiesner[5]. The approximately periodic behavior of $N(r)$ is clearly seen. For $\sigma = 0.8$ Å the period of the oscillations as measured from Fig. 2.1 is 2.73 Å$= a_0/2$ where $a_0$ is the lattice constant. This period will be theoretically justified below.

**2.2.3 Analytic Form**

Let us now derive an analytic form for $N(r)$. Consider a lattice composed of all possible acceptor sites. For simplicity, assume that this lattice has only one atom per unit cell. The acceptor sites are then specified by

$$\mathbf{T} = n_1\mathbf{a}_1 + n_2\mathbf{a}_2 + n_3\mathbf{a}_3, \tag{2.4}$$

where $\mathbf{a}_1$, $\mathbf{a}_2$, and $\mathbf{a}_3$ are the primitive translation vectors and $n_1$, $n_2$, and $n_3$ run over all integer values. Let $V_c$ denote the volume of the unit cell, and let the reciprocal lattice vectors be labelled by $\mathbf{G}$. Let the donor position be specified by $\mathbf{R}_d$. The total number of lattice points enclosed by a sphere of radius $r$, centered at $\mathbf{R}_d$, can be expressed as

$$L(r, \mathbf{R}_d) = \sum_{\mathbf{T}} \Theta(r - |\mathbf{T} - \mathbf{R}_d|), \tag{2.5}$$

where $\Theta$ is a unit step-function. The function $L(r, \mathbf{R}_d)$ is periodic in $\mathbf{R}_d$ and so it can be expanded in a Fourier series,

$$L(r, \mathbf{R}_d) = \sum_{\mathbf{G}} c(\mathbf{G}) \exp(i\mathbf{G} \cdot \mathbf{R}_d). \tag{2.6}$$

Following Kendall and Rankin[8], the coefficients $c(\mathbf{G})$ are given by

$$c(\mathbf{G}) = \frac{1}{V_c}\int_{cell} L(r,\mathbf{R}_d)\exp(-i\mathbf{G}\cdot\mathbf{R}_d)d\mathbf{R}_d \tag{2.7a}$$

$$= \frac{1}{V_c}\sum_{\mathbf{T}}\int_{cell}\Theta(r-|\mathbf{T}-\mathbf{R}_d|)\exp(-i\mathbf{G}\cdot\mathbf{R}_d)d\mathbf{R}_d \tag{2.7b}$$

$$= \frac{1}{V_c}\int_{|\mathbf{R}|\leq r}\exp(i\mathbf{G}\cdot\mathbf{R})d\mathbf{R} \tag{2.7c}$$

$$= \frac{1}{V_c}\frac{4\pi r^2}{|\mathbf{G}|}j_1(|\mathbf{G}|r), \tag{2.7d}$$

where $j_1$ is a spherical Bessel function of the first kind. The distribution of acceptor sites located a distance $r$ from the donor can now be evaluated to be

$$N(r) = \frac{dL(r,\mathbf{R}_d)}{dr} = \frac{4\pi r^2}{V_c}\left(1+\sum_{\mathbf{G}\neq\mathbf{0}}\frac{\sin(|\mathbf{G}|r)}{|\mathbf{G}|r}\exp(i\mathbf{G}\cdot\mathbf{R}_d)\right). \tag{2.8}$$

It is clear from Eq. (2.8) that $N(r)$ is approximately periodic in $r$ with frequencies given by $|\mathbf{G}|/2\pi$. Depending on the value of $\mathbf{R}_d$ some frequencies may not be observed. In particular, if $\cos(\mathbf{G}\cdot\mathbf{R}_d) = 0$ then the frequency $|\mathbf{G}|/2\pi$ is forbidden. The above discussion can easily be generalized to include more than one type of acceptor site (*i.e.* more than one atom per unit cell in the lattice). $N(r)$ then contains a summation of the form Eq. (2.8) for each inequivalent type of acceptor site. Inequivalent donor sites can be handled in a similar manner. Finally, we note that the role of acceptors and donors in the above discussion can be interchanged and the results are the same.

These results can be applied to the problem of GaP:(N,acceptor). The acceptor ions are located on an face-centered-cubic lattice with $V_c = {a_0}^3/4$ where $a_0 = 5.45$ Å is the lattice constant. The frequencies of oscillation are found to be $\sqrt{3}/a_0, 2/a_0, 2\sqrt{2}/a_0, \ldots$ . The donor is located at $\mathbf{R}_d = a_0(1/4, 1/4, 1/4)$ so that the frequency $\sqrt{3}/a_0$ is forbidden. Therefore, the lowest frequency will be $2/a_0$ as observed in the numerical calculation shown in Fig. 2.1 for $\sigma = 0.8$ Å.

For a broadening of $\sigma = 0.3$ Å, some of the higher frequency components are observed.

**2.2.4 Physical Interpretation**

Now that we have a mathematical reason for the observed undulations in the GaP:(N,acceptor) spectrum, it is interesting to seek some simple physical interpretation of the results. From the form of Eq. (2.8) this interpretation is obvious. The reciprocal lattice vectors label lattice plane in real-space. The period of oscillation $2\pi/|\mathbf{G}|$ is simply equal to the perpendicular distance between lattice planes. Consider the number of lattice points contained in a sphere of radius $r$. As $r$ increases, the sphere will intersect new lattice planes. Each time such an intersection occurs there will be a sharp increase in $L(r)$ and a corresponding peak in $N(r)$. Thus, the frequency $|\mathbf{G}|/2\pi$ is associated with those lattice planes labelled by $\mathbf{G}$. As a corollary, we note that those acceptor ions which contribute to the $|\mathbf{G}|/2\pi$ fluctuations in $N(r)$ will be concentrated around the directions from the donor which are parallel to $\mathbf{G}$.

This physical interpretation is demonstrated graphically for the two-dimensional simple-cubic lattice shown in Fig. 2.2. The reciprocal lattice is also simple-cubic. The lowest frequencies of oscillation are $1/a_0$ and $\sqrt{2}/a_0$ corresponding to reciprocal lattice vectors $\mathbf{G} = 2\pi(1,0)/a_0$ [(10) lattice planes] and $\mathbf{G} = 2\pi(1,1)/a_0$ [(11) lattice planes] respectively. As shown in the figure, the (10) planes give rise to $1/a_0$ fluctuations in $N(r)$ and the (11) planes give rise to $\sqrt{2}/a_0$ fluctuations in $N(r)$. For other lattice types the geometry is more complicated but the source of oscillations in $N(r)$ is the same.

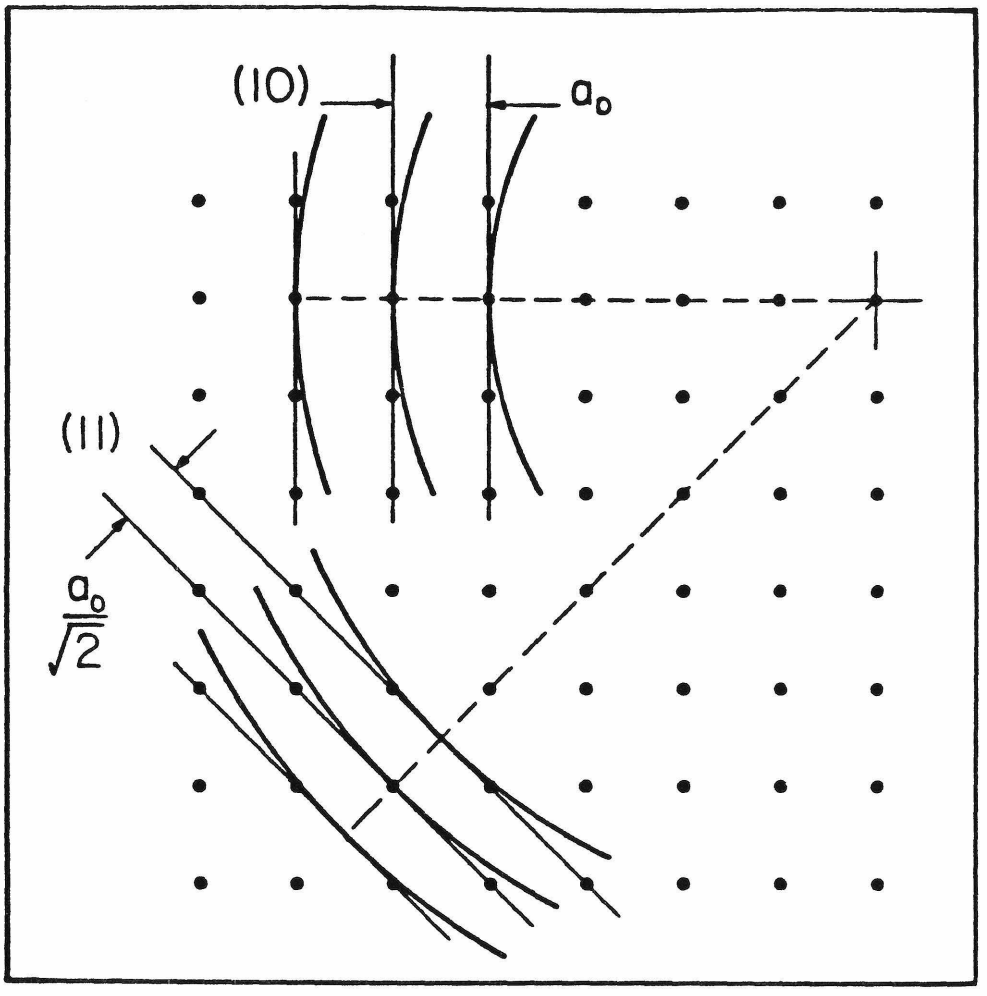


**Figure 2.2:** Lattice planes in a two-dimensional simple-cubic lattice. As $r$ increases, the total number of points $L(r)$ contained in a circle of radius $r$ increases sharply each time a new plane is intersected. This results in periodic oscillations in $N(r) = dL(r)/dr$, the distribution of lattice sites located a distance $r$ from the center of the circle.

## 2.3 CONCLUSIONS

In this chapter we have discussed the geometry of donor-acceptor pairs in a zinc-blende lattice. We have calculated the number of possible sites in each donor-acceptor shell. The luminescence energies for GaP:(Zn,O) pairs have been tabulated. The original part of this work is the derivation of an analytic form for $N(r)$, the continuous distribution of donor-acceptor site separations. From this analytic form, we have shown that the observed periodicity of GaP:(N,acceptor) luminescence spectra is the result of long-range order in the crystal lattice. In principal the crystal symmetry could be deduced from the spectra, but in practice this may be difficult since it would require detailed knowledge of the relationship between luminescence energy and the donor-acceptor separation.

## REFERENCES


1. Reported by J. J. Hopfield in *Proceedings of the International Conference on II-VI Semiconducting Compounds*, edited by D. G. Thomas (Benjamin, New York, 1968), p. 786.
2. J. J. Hopfield, H. Kukimoto, and P. J. Dean, *Phys. Rev. Lett.* **27**, 139 (1971).
3. T. N. Morgan, M. R. Lorenz, and A. Onton, *Phys. Rev. Lett.* **28**, 906 (1972).
4. C. H. Henry and M. D. Sturge, *Bull. Amer. Phys. Soc.* **18**, 415 (1973).
5. R. A. Street and P. J. Wiesner, *Phys. Rev. Lett.* **34**, 1569 (1975).
6. D. G. Thomas, M. Gershenzon, and F. A. Trumbore, *Phys. Rev.* **133**, A269 (1964).
7. L. Patrick, *Phys. Rev.* **180**, 794 (1969).
8. D. G. Kendall and R. A. Rankin, *Quart. J. Math.* (Oxford), **4**, 178 (1953).

# CHAPTER 3

# DEFECT REACTIONS IN GaP:(Zn,O)

## 3.1 INTRODUCTION

### 3.1.1 Degradation of GaP:(Zn,O) Light-Emitting-Diodes

Defect complexes in semiconductors can play an important role in determining the electrical and optical characteristics of the material. One simple complex which commonly occurs is a pair of donor and acceptor impurities. The energy of the luminescence emitted from donor-acceptor (DA) pairs depends on the separation of the impurities[1], and so a luminescence spectrum provides information about the number of pairs of each possible separation.

In gallium phosphide, a zinc atom substituting for gallium ($Zn_{Ga}$) forms a shallow acceptor, and an oxygen atom substituting for phosphorous ($O_P$) forms a deep donor. When these impurities occupy nearest-neighbor lattice sites they produce intense red luminescence. Consequently, this material has been used for making red-light-emitting-diodes[2]. When operated under forward bias, the performance of these diodes is observed to degrade with time[3—5]. This study provides a microscopic explanation for this degradation; namely, that the nearest-neighbor (Zn,O) pairs dissociate and re-form as further separated pairs.

In general the degradation of semiconductor devices is due to some change in the physical structure of the device. Defects are formed by the rearrangement of the atoms in the bulk material or at interfaces. These changes in the structure affect the recombination paths for carriers and thereby affect the device characteristics. The energy to move the atoms comes either from purely thermal processes, or from some type of carrier recombination event in the material. In the latter case, we can view the process as involving the transfer of energy from an electronic excitation to a vibrational excitation, ultimately leading to atomic motion. This phenomenon clearly requires a strong electron-phonon interaction. In the GaP:(Zn,O) system studied here, we have obtained a detailed picture of

the reactions which cause the device degradation. These types of reactions have not previously been observed in a material which is as well characterized as GaP:(Zn,O). Thus, this system provides a unique opportunity for studying the strong electron-phonon interaction which is often present at "deep-level" defects in semiconductors. The understanding of this interaction is important since it significantly affects the performance of semiconductor devices[6,7].

### 3.1.2 Results of this Work

In this work we use photoluminescence to monitor the relative positions of Zn and O impurities in GaP. When the GaP is subjected to laser excitation at high temperatures, we observe reactions in which the impurities diffuse through the lattice to occupy new substitutional sites. This is the first time that DA luminescence has been used as a microscopic probe of defect reactions. From low-temperature studies we identify these reactions as being the dissociation of nearest-neighbor (Zn,O) pairs and the formation of further separated pairs. Such a dynamic process of reactions among lattice defects of known chemical type has not previously been observed in a semiconductor.

We have identified the mechanism for the photoinduced reactions by measuring the reaction rates versus laser power and temperature. The dissociation rate of the nearest-neighbor pairs is deduced using a model for the electron-hole recombination kinetics which includes the effects of high carrier occupation (saturation) and spatially varying carrier generation. The activation energy for the photoinduced reaction is found to be $0.60 \pm 0.07$ eV with a pre-exponential factor of about $3 \times 10^4$ $s^{-1}$. From annealing studies, the activation energy for purely thermal dissociation of the pairs is estimated to be $2.6 \pm 0.6$ eV with a pre-exponential factor of roughly $10^{10}$ $s^{-1}$. From these values, the photoinduced pair dissociation is identified as a "recombination-enhanced defect reaction" (REDR). In the

reaction, nonradiative electron-hole recombination puts the defect into a highly excited vibrational state, leading to the dissociation of the pair.

### 3.1.3 Outline of Chapter

Photoluminescence (optical emission) data will be presented throughout this chapter, and some experimental details are summarized in Section 3.2. In Section 3.3 photoluminescence spectra are displayed which clearly show the dissociation of nearest-neighbor (Zn,O) pairs and the formation of further separated pairs. These reactions are observed in real-time at high temperatures. Low temperature spectra are obtained in order to identify the initial and final states of the reaction.

In Section 3.4 we discuss the reaction rates for the photoinduced pair dissociation. Equations are formulated describing the electron-hole recombination kinetics. Simple relations between the observed photoluminescence intensities and the defect concentrations are derived. Using these relations, an analysis is made of the decay rates of the luminescence intensities. Activation energies for the reactions are deduced. In Section 3.5, a discussion is given of the mechanism for the photoinduced reactions. It is argued that the dissociation proceeds by the excitation of vibrational modes of the defect by nonradiative electron-hole recombination. The conclusions which can be drawn from this work are presented in Section 3.6.

## 3.2 EXPERIMENTAL

### 3.2.1 Apparatus

Figure 3.1 shows a diagram of the apparatus used in these experiments. The excitation source was an $Ar^+$ laser. The laser beam was filtered to remove stray lines and was directed at the sample. For the low temperature work ($T < 100$

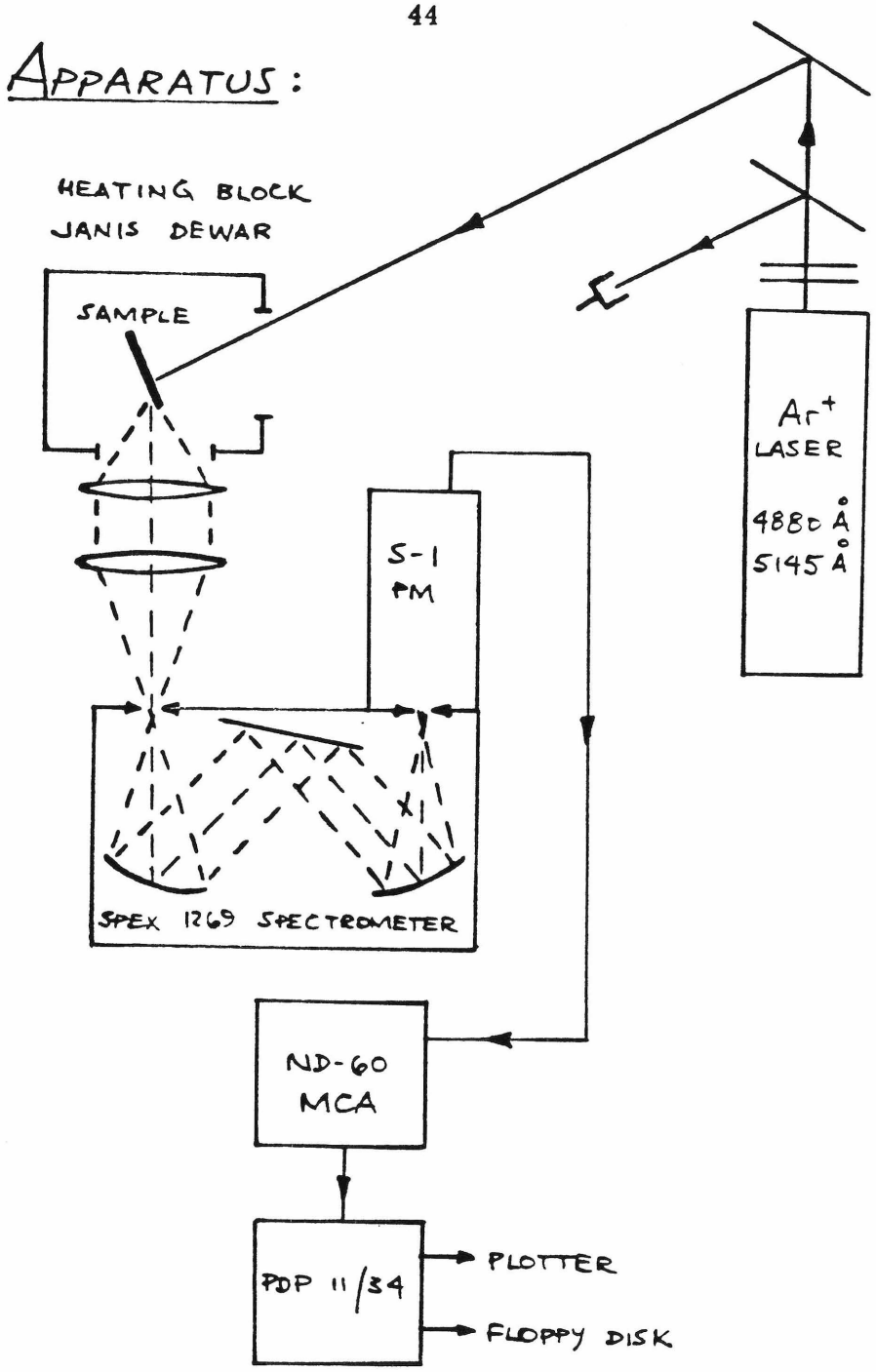


**Figure 3.1:** A schematic of the apparatus used in photoluminescence experiments. The incident laser excites the sample, causing it to emit characteristic luminescence. A particular wavelength of the luminescence is selected with the spectrometer, and the intensity of this signal is measured with a photomultiplier (PM). The data are acquired on a multi-channel-analyzer (MCA) and passed to a computer for analysis and storage. A typical experiment will record intensity versus wavelength as the spectrometer is scanned, or intensity versus time at a single wavelength.

K) reported here the sample was mounted in a variable temperature cryostat and illuminated with the 4545 Å laser line. The sample was moved vertically to permit observation of different regions of the crystal and the change in photon collection efficiency between these runs was very small. For the high temperature work (300 K $< T <$ 700 K) the sample was mounted on a heating block and illuminated with the 4880 Å laser line, focussed to a beam diameter of 55 $\mu$m (FWHM). For the results reported here the sample was in air, although similar results were obtained when the sample was in a He environment. The photoluminescence spectra were obtained using a $LN_2$ cooled S-1 type photomultiplier and a SPEX 1269 spectrometer with a 1200 gr/mm grating blazed a 1 $\mu$m. The data were acquired on an ND-60 multi-channel-analyzer and were passed to a PDP 11/34 computer for permanent storage. Annealing studies ($T >$ 1000 K) were performed in a furnace purged with He. Following each anneal the sample was quenched in water and etched for 3 min in 3:1:1 $H_2SO_4$:$H_2O_2$:$H_2O$ at 60 $^\circ$C.

### 3.2.2 Sample Description

The samples used in this work were liquid-phase-epitaxially grown $pn$ junctions on $n$-type GaP (single crystal). The growth technique is described by Saul, Armstrong, and Hackett[2]. The samples consisted of an $n$-type substrate on which was grown a 50 $\mu$m thick $n$-type layer followed by a 50 $\mu$m thick $p$-type layer. This top $p$-type layer was doped with Zn and O. The (substitutional) O concentration is about $10^{16}$ cm$^{-3}$ and the Zn concentration is about $3 \times 10^{17}$ cm$^{-3}$ (based on crystal growth conditions). Other impurities include N and S. The photoluminescence spectra were obtained with the excitation laser incident on the $p$-type layer. The absorption depth of the laser light is roughly 10 $\mu$m so that only luminescence from this top layer is observed.

### 3.2.3 Sample Heating

The reactions observed in these experiments can proceed thermally or by athermal photoinduced mechanisms. In order to separate these processes it is essential to know how much the laser excitation source heats the sample. This sample heating can be theoretically estimated by considering the heat diffussion problem in an infinite slab of thickness $l$ with one side at a constant temperature and the other side exposed to a surface heat source with a Gaussian profile. The maximum temperature increase $\Delta T$ in the sample can be shown to be

$$\Delta T = \frac{P}{2\pi k\sigma} \cdot \begin{cases} 1 & \sigma \ll l \\ \frac{l}{\sigma} & \sigma \gtrsim l \end{cases} \tag{3.1}$$

where $P$ is the laser power, $k$ is the thermal conductivity ($k$ = 0.4 W/cmK at 473 K for GaP[8]) and $\sigma$ is the beam width (FWHM= $2\sigma\sqrt{(2\ln 2)}$ ). For the experiments discussed here $\sigma = 55\mu$m and $l = 350\mu$m so that the limit $\sigma \ll l$ applies. For a typical power level of $P$ = 200 mW we find $\Delta T$ = 35 K. This amount of sample heating is small enough so that we can easily distinguish thermal and photoinduced effects.

## 3.3 OBSERVATION OF PHOTOINDUCED REACTIONS

### 3.3.1 Identification of the Reaction

In this section we will present data which show photoinduced reactions involving (Zn,O) pairs in GaP. Figure 3.2 shows several high and low temperature photoluminescence spectra obtained from samples of GaP:(Zn,O). These spectra were obtained using above-band-gap laser excitation at the power levels indicated. Figure 3.2(a) shows a series of successive scans, obtained at the relatively high temperature of 470 K. As first shown by Onton and Lorenz[9] these spectra consist of a band centered at 1.7 eV due to nearest-neighbor $(Zn,O)_{m=1}$ pairs, and a

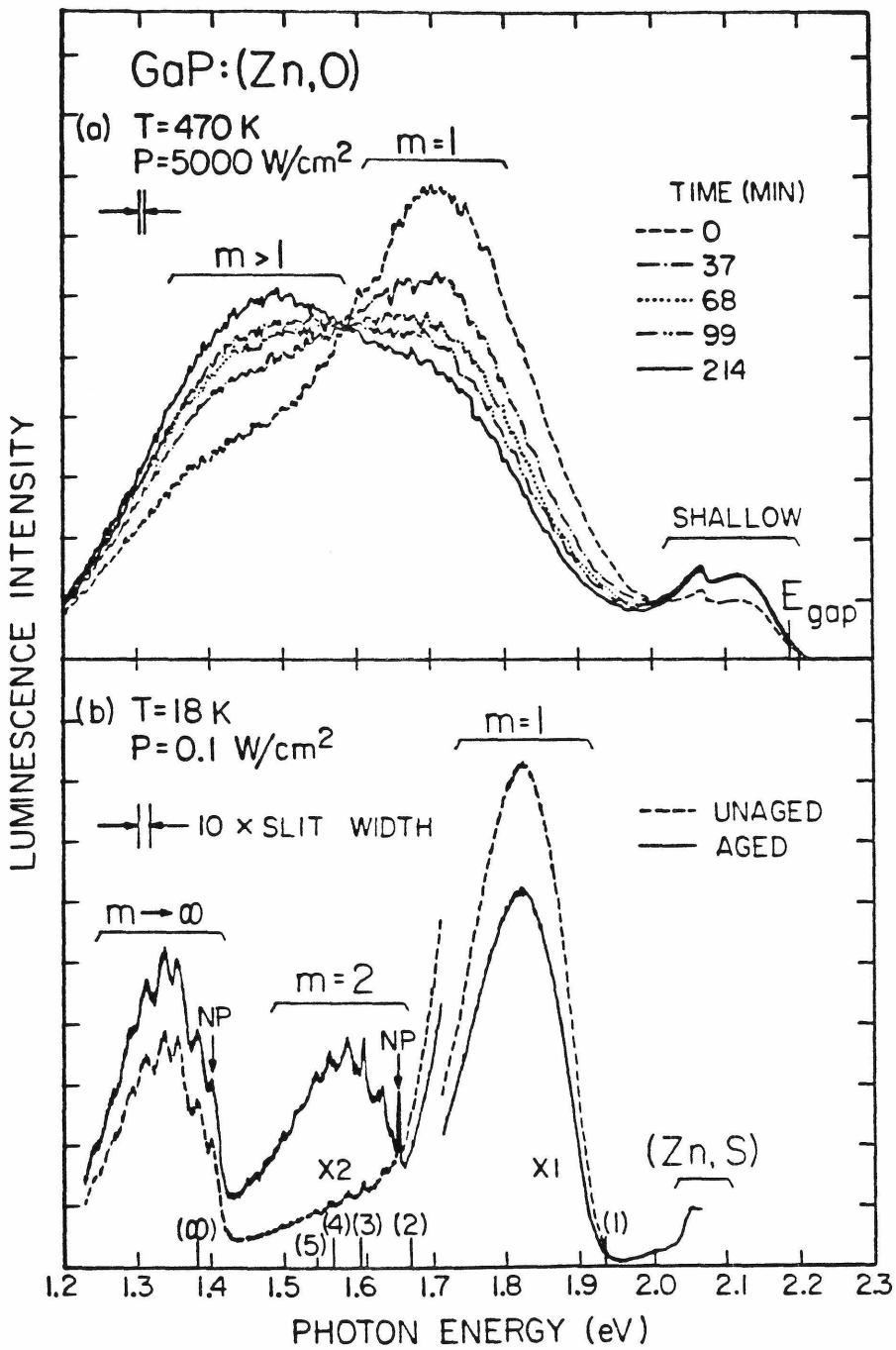


**Figure 3.2:** Photoluminescence spectra at various temperatures ($T$) and laser power densities ($P$); (a) time-resolved spectra showing defect reactions in progress and (b) the initial and final states of the reaction. The label $m$ denote luminescence from an $m^{th}$-nearest-neighbor (Zn,O) pair. NP refers to a no-phonon-assisted transition. Theoretical predictions for the line positions are shown on the abscissa.

band centered at 1.5 eV due to further separated pairs $(Zn,O)_{m>1}$. There is also luminescence at 2.1 eV due to various shallow impurities and possibly free-exciton or band-to-band recombination. The incident laser was illuminating the sample continuously during these measurements. The scans were acquired successively, and are separated in time by about 30 min each. We see that the spectra are changing with time. This is a direct observation of a reaction in progress. We refer to this reaction as an "aging" process. The initial and final spectra shown are similar to those seen by Dapkus and Henry[4]. These authors showed that the aging reaction is due to photoinduced destruction of nearest-neighbor (Zn,O) pairs, and they speculated that the pairs were in fact dissociating and forming further separated pairs. Here, we prove that this speculation is correct.

To clearly identify the luminescence bands we go to the low temperature spectra shown in Fig. 3.2(b). In this figure, the spectrum labelled "aged" was obtained from a sample which was subjected to the high temperature aging treatment discussed above. The "unaged" spectrum was obtained from a sample which was not aged. From the work of previous authors[10−12] we identify the band centered at 1.82 eV as being due to nearest-neighbor pairs $(Zn,O)_{m=1}$, and the band centered at 1.35 eV as due to far separated pairs $(Zn,O)_{m\to\infty}$. The breadth of these bands is due to phonon-assisted radiative transitions. Centered at 1.59 eV is a luminescence band which is seen in the aged sample, but barely visible in the unaged material. The breadth of this band is similar to those of $(Zn,O)_{m=1}$ and $(Zn,O)_{m\to\infty}$ and the resolved phonon structure is characteristic of a complex involving O. Furthermore, if we compare the no-phonon transition energy with theoretical predictions[1,13], we see that the position of this new band is as expected for $(Zn,O)_{m=2}$. Thus, we identify the new luminescence as being due to second-nearest-neighbor $(Zn,O)_{m=2}$ pairs.

The aging process has clearly affected the intensity of the various luminescence bands shown in Fig. 3.2(b). The intensity of the $m = 1$ band has decreased and the intensity of the $m > 1$ bands have increased. The luminescence at about 2.05 eV is due to (Zn,S) donor-acceptor pairs. This luminescence is constant in intensity between the unaged and aged material, indicating that the low temperature minority carrier concentration is also constant. Thus, the reduced intensity of the $m = 1$ band in the aged material must be due to a reduction of the $(Zn,O)_1$ concentration. Similarly, the $(Zn,O)_{m>1}$ concentration has increased. The reduction in $m = 1$ pair concentration has been accompanied by an increase in concentration of $m > 1$ pairs. We note that in Fig. 3.1(a) the $m > 1$ band is increasing at exactly the same rate as the $m = 1$ band is decreasing. Also, as will be shown in following section, the number of dissociated $m = 1$ pairs is roughly equal to the number of newly formed $m > 1$ pairs. Thus, we conclude that the nearest-neighbor pairs are dissociating and forming further separated pairs.

The $(Zn,O)_{m=1}$ dissociation reaction is not a thermal one, since the temperature in Fig. 3.2(a) is only 470 K (sample heating due to the laser is about 20 K), and the $(Zn,O)_{m=1}$ pairs are thermally stable up to 800 K. Rather, the reaction is photoinduced[4]. The incident light creates electron-hole pairs in the material, and the electrons and holes may be captured and may recombine at the (Zn,O) centers. The energy to dissociate the $(Zn,O)_{m=1}$ pairs comes from some electron (or hole) capture or recombination event at the defect. In Section 3.4 we will identify this event to be electron-hole recombination.

### 3.3.2 Redistribution of Pairs

We have studied the pair re-formation process by measuring the number of pairs of a given shell number $m$ which are produced by the aging process. Figure 3.3 shows low temperature spectra in an unaged and an aged sample. The

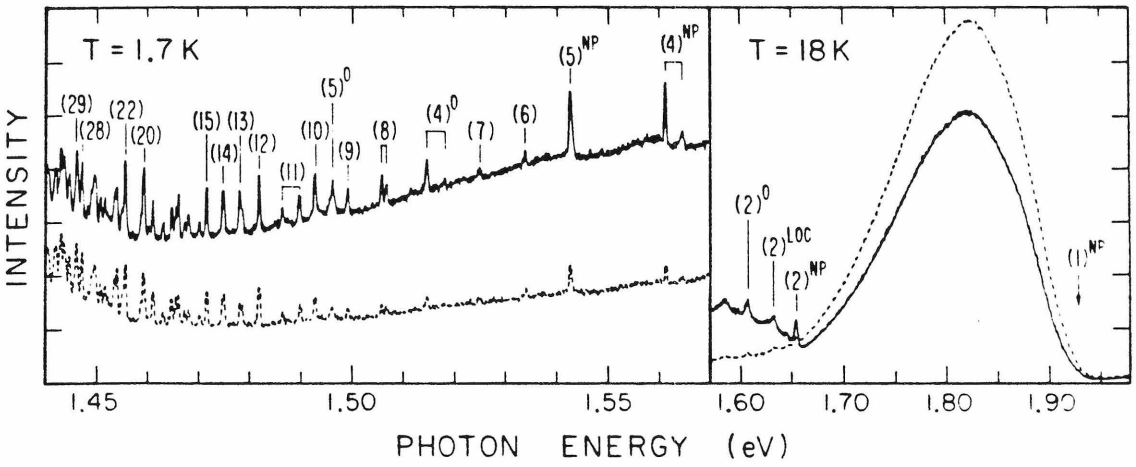


**Figure 3.3:** Low temperature donor-acceptor luminescence from an aged (solid line) and an unaged (dashed line) sample. The lines are labeled by $(m)$ for $m^{th}$-nearest-neighbor pairs with a superscript indicating the type of phonon involved in the transition (O=optical, LOC=local, NP=no-phonon). Those labels with no superscripts refer to no-phonon transitions. Note the intensity and energy scale change at 1.57 eV. The data on the left had a flat background subtracted from them.

discrete lines in the spectra are $(Zn,O)_m$ donor-acceptor (DA) luminescence. The broad background is due to radiative processes involving mainly recombination of electrons bound to $m = 1$ and $m = 2$ pairs with holes bound to distant acceptors. The pairs responsible for the discrete DA lines are labelled in accordance with previous identifications[12], although we have reidentified a few of the lines as phonon-assisted transitions. The minority carrier concentration is observed to be the same in the unaged and aged samples, so that the ratio of line intensities between the samples is equal to the ratio of pair concentrations. In the aged material, the line intensity is the sum of that from the new centers produced by the aging and that from the centers which existed prior to the aging. Thus, the concentration of centers produced by the aging is given by

$$N'_m = N_m\left(\frac{I'_m}{I_m} - 1\right), \tag{3.2}$$

where $I_m$ and $I'_m$ are the luminescence intensities in the unaged and aged sample respectively, and $N_m$ is the pair concentration in the unaged material. $N_m$ can be computed[14] by considering equilibrium between oppositely charged ions at the growth temperature of the crystal. For small $m$ this is a very crude model, but it has been shown to give reasonable results[9].

The concentration of new $m > 1$ centers produced by the aging process is dependent on the sample conditions prior to aging. Figure 3.4 shows typical results, based on the integrated DA line intensities of Fig. 3.3. We see that the dissociated nearest-neighbor pairs tend to re-form as pairs with low $m$. By interpolating between the data points in Fig. 3.4 and extrapolating to large $m$, we can estimate the total number of new $m > 1$ pairs formed by the dissociation of the $m = 1$ pairs. We find that the number of newly formed $m > 1$ pairs roughly equals the number of dissociated $m = 1$ pairs. The distribution of new pairs contains some information about the pair re-formation process. At present

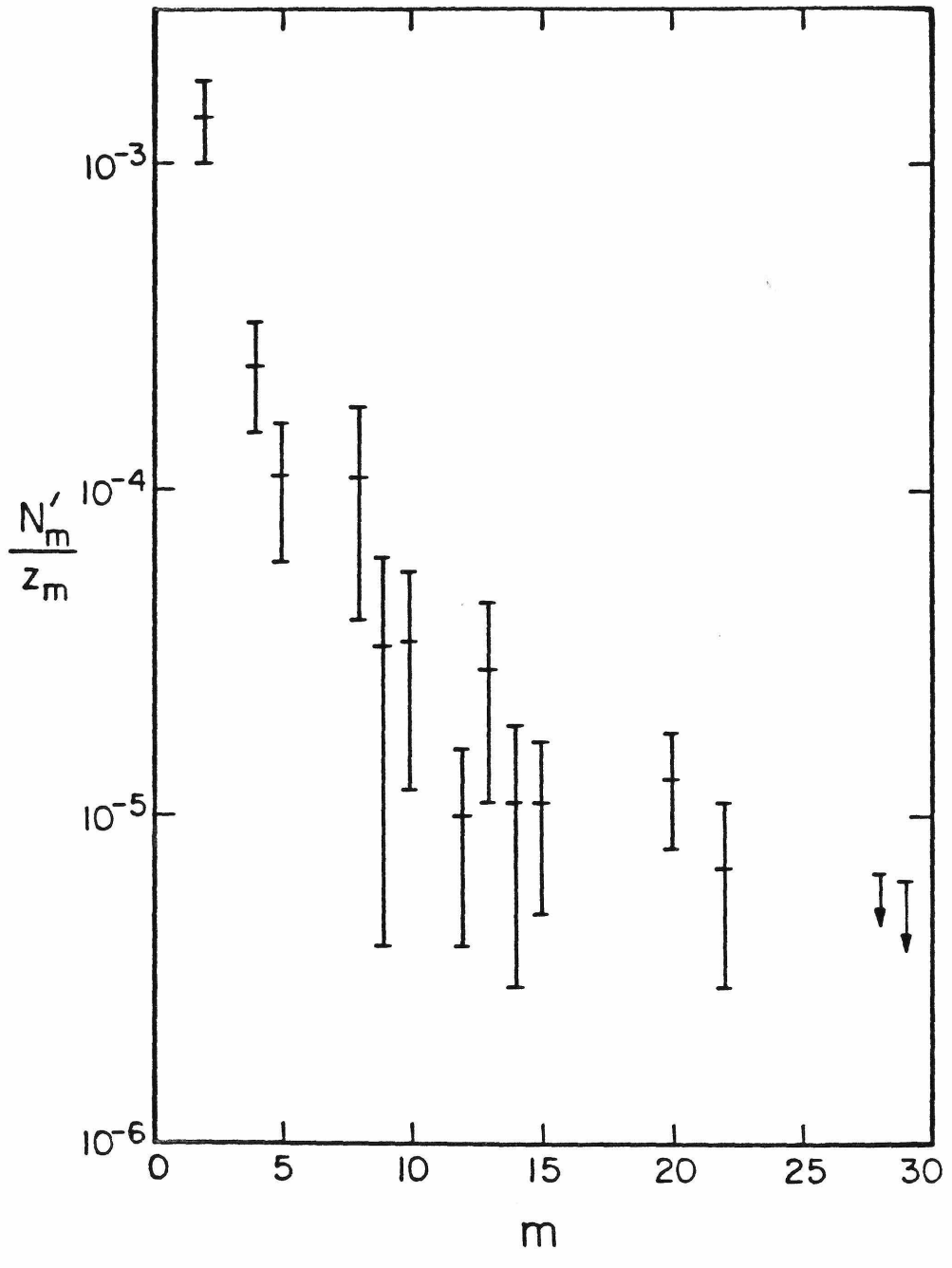


**Figure 3.4:** The distribution of new pairs formed by the aging process. $N'_m$ is the concentration of $m^{th}$-nearest-neighbor pairs, normalized to the total concentration of pairs (estimated) in the sample. $z_m$ is the number of equivalent $m^{th}$-nearest-neighbor sites.

we do not have a theory which allows us to uniquely identify the re-formation mechanism. In Section 3.5 we will discuss further the atomic motions involved in the pair dissociation and re-formation.

## 3.4 REACTION RATES

### 3.4.1 Electron-hole Recombination Kinetics

To understand the mechanism of the (Zn,O) pair dissociation, we have performed measurements of the reaction rates. The first step in a quantitative analysis of these rates is to relate the observed luminescence intensities with the pair concentrations. This relation requires some understanding of the electron-hole populations in the material. The kinetics of electron-hole recombination in GaP:(Zn,O) have been extensively studied[15—21]. It is not the purpose of this work to obtain a detailed understanding of the recombination kinetics. Rather, we wish to arrive at approximate values for some of the kinetic parameters. From these values we will determine the regime of carrier concentrations in which our experiments lie and this will enable us to make a reasonable interpretation of the data to be presented in Section 3.4.2.

We use a simple but accurate model which is similar to that used for nearest-neighbor pairs by Henry, Bachrach, and Schumaker[21]. Each $(Zn,O)_m$ center is considered to be a single electron trap, with an associated electron release rate $R_m$, capture rate $C_m$, and a total recombination rate $1/\tau_m$. For $m \rightarrow \infty$, *i.e.* isolated oxygen, a second electron level has been observed[6]. Here we will be considering centers with $m < 50$ for which this level has not been observed (it probably is not bound due to the Coulomb repulsion of the acceptor) and so we need not consider it. For the present discussion, the hole occupation of

the $(Zn,O)_m$ centers will be implicitly included in the electron recombination rate $1/\tau_m$. Later, we will consider the dependence of $1/\tau_m$ on the various hole concentrations. The concentration $n_m$ of $(Zn,O)_m$ centers which are occupied by electrons is given by

$$\frac{dn_m}{dt} = \frac{-n_m}{\tau_m} - R_m n_m + C_m(N_m - n_m)n_0, \qquad m = 1, 2, 3, ... \tag{3.3}$$

where $N_m$ is the total concentration of $(Zn,O)_m$ centers and $n_0$ is the free electron concentration. In steady state, the concentration of occupied $(Zn,O)_m$ centers is found by equating Eq. (3.3) to zero to yield

$$f_m = \frac{n_m}{N_m} = \frac{n_0/n_{tm}}{1 + n_0/n_{tm}}, \tag{3.4a}$$

where

$$n_{tm} = \frac{(1/\tau_m + R_m)}{C_m}. \tag{3.4b}$$

Here, $f_m$ represents the fractional electron occupation of the centers. The intensity of luminescence emitted from an $m^{th}$-nearest-neighbor pair is given by

$$I_m = \frac{1}{\tau_m^{rad}} n_m = \frac{1}{\tau_m^{rad}} N_m f_m, \tag{3.5}$$

where $1/\tau_m^{rad}$ is the radiative decay rate. Later in this work we will discuss processes in which the impurity concentrations $N_m$ vary with time. However, these time variations are very slow compared with thoses expressed in Eq. (3.3) and so Eq. (3.4) is still valid at each point in time.

Let us consider the minority carrier (electron) concentration $n_0$. The variables of interest in these experiments are the laser power $P$, the temperature $T$, and the impurity concentrations $N_i$. The impurities labelled by $N_i$ include the $(Zn,O)_m$ centers as well as various intrinsic impurities which could be undergoing photoinduced reactions[5,22]. In steady state $n_0$ is a complicated function of $T$, $P$

and $N_i$. Neglecting spatial diffusion we write

$$n_0 = G\tau_0, \tag{3.6}$$

where $G$ is the electron-hole generation rate and $\tau_0$ is defined by this equation to be the steady-state minority carrier lifetime. We will assume that $\tau_0$ has no spatial dependence. This neglects effects such as surface recombination. The spatial dependence of $G$ is derived by considering the incident laser beam which is perpendicular to the surface ($x, y$ plane) of the crystal. The photon density has a Gaussian dependence on $\rho = \sqrt{(x^2 + y^2)}$ and varies exponentially with $z$ (the direction into the crystal). Thus, the generation rate can be expressed as

$$G = \frac{\alpha P}{h\nu_i 2\pi\sigma^2} \exp\left(\frac{-\rho^2}{2\sigma^2} - \alpha z\right), \tag{3.7}$$

where $1/\alpha$ is the absorption depth, $\sigma$ is the beam radius, $h\nu_i$ is the incident photon energy, and $P$ is the absorbed laser power. The laser power levels reported here actually correspond to incident power, but this difference is not significant in our calculations. The minority carrier lifetime $\tau_0$ is determined by all of the various recombination channels in the material. In our experiments we observe quantities which are independent of $\tau_0$ and so we do not need to know its precise value. The minority carrier concentration can be estimated by observing the luminescence intensity as a function of laser power[16]. For the nearest-neighbor pairs at $T \approx 500$ K we observe significant saturation effects ($f_1 \approx 0.5$) to begin at $P \approx 100$ mW (FWHM=55 $\mu$m). At this temperature $1/\tau_1 \approx 10^6$ s$^{-1}$ (Ref. 21) $\ll R_1 \approx 10^8$ s$^{-1}$ (Ref. 19). The maximum minority carrier concentration is then given by $n_0 \approx n_{t1} \approx R_1/C_1 \approx 5 \times 10^{15}$ cm$^{-3}$. This also equals the concentration of majority carriers (holes) introduced by the laser. From Eqs. (3.6) and (3.7) this value of $n_0$ corresponds to a lifetime of $\tau_0 \approx 1$ nsec which seems quite reasonable.

Much of the complicated electron-hole recombination kinetics has been hidden in the rates $1/\tau_0$, $1/\tau_m$ and $1/\tau_m^{rad}$. The rate $1/\tau_m$ is the sum of nonradiative and radiative rates. There are two nonradiative decay channels: Auger decay[19] and multi-phonon-emission (MPE) recombination[6]. There are also two radiative decay channels: the bound electron can recombine with a hole bound onto the same $(Zn,O)_m$ center, or with a hole bound onto a distant impurity, namely, a Zn acceptor[11,15]. The rates $1/\tau_m$ and $1/\tau_m^{rad}$ are therefore functions of the temperature and various hole concentrations. For $T \approx 500$ K the concentration of holes introduced by the laser is small compared with the free hole concentration of $p \approx 10^{17}$ cm$^{-3}$. Furthermore, the shallowly bound holes are in equilibrium with the free holes[20,21]. Thus, $1/\tau_m$ and $1/\tau_m^{rad}$ will be functions only of temperature, and will have very little spatial or time dependence.

Now let us specialize to the experimental results presented in the following section. In these experiments the sample is exposed to the laser at some temperature 300 K $< T <$ 700 K and some laser power $P$. The intensity of $(Zn,O)_{m=1}$ luminescence is observed to decrease with time, presumably due to some changing impurity concentration $N_i$. The luminescence intensity is given by

$$I_1(t) = \frac{1}{\tau_1^{rad}} \int dV N_1(\rho, z, t) f_1(\rho, z, t), \tag{3.8}$$

where the spatial dependence of the electron occupation $f_1$ is given by Eqs. (3.4a), (3.6), and (3.7). $N_1$ refers to the concentration of nearest-neighbor $(Zn,O)_{m=1}$ pairs, whereas $N_i$ refers to the concentration of any type of impurity in the sample ($(Zn,O)_m$ pairs, intrinsic defects, *etc.*). At low power levels the electron occupation $f_1$ is proportional to the minority carrier concentration $n_0$. In general, $n_0$ changes with $N_i$ and results in changes in the $(Zn,O)_{m=1}$ luminescence intensity. We have observed these effects. At low powers, a change in $n_0$ will cause

the entire luminescence spectrum to change uniformly. However, at high powers the luminescence band saturates; $f_1 \rightarrow 1$ for most of the centers contributing to the band. In that case the luminescence intensity is independent of $n_0$. The observed decreasing intensity is due to a decreasing concentration of $(Zn,O)_1$ pairs, and the intensity is directly proportional to the pair concentration. The data presented in the following section are in this high power regime.

### 3.4.2 Analysis of Observed Dissociation Rates

Figure 3.5 shows the decay of the $(Zn,O)_{m=1}$ luminescence at several different temperatures. These decay curves are nonexponential. Typically, the luminescence intensity initially changes relatively fast, then it slows down to a long-lived tail. We attribute this nonexponential behavior to a nonuniform minority carrier (electron) density in the material. This nonuniformity is due to the Gaussian profile of the incident laser beam, and the exponential dropoff of its intensity into the sample. A nonuniform electron density results in a nonuniform electron occupation of the $(Zn,O)_1$ centers. Those centers with high occupation ($f_1 \rightarrow 1$) dissociate at some rate, and those centers with low occupation ($f_1 \rightarrow 0$) dissociate at a much slower rate. The observed decay curves are integrals over the sample of all the individual exponential decays. The result is a nonexponential decay. For high laser powers the observed luminescence is initially due almost entirely to the saturated centers. In that case the luminescence intensity is proportional to the pair concentration and independent of $n_0$, as discussed in Section 3.4.1. At later times we observe those centers whose occupation is lower. Then, the luminescence intensity may depend on $n_0$. We can monitor $n_0$ by observing the intensity of luminescence from the shallow impurity levels. As shown in Fig. 3.2, the variation in $n_0$ occurs over a much shorter time period than the $(Zn,O)_{m=1}$ decay time. We observe that this is true for $P \geq 100$ mW at

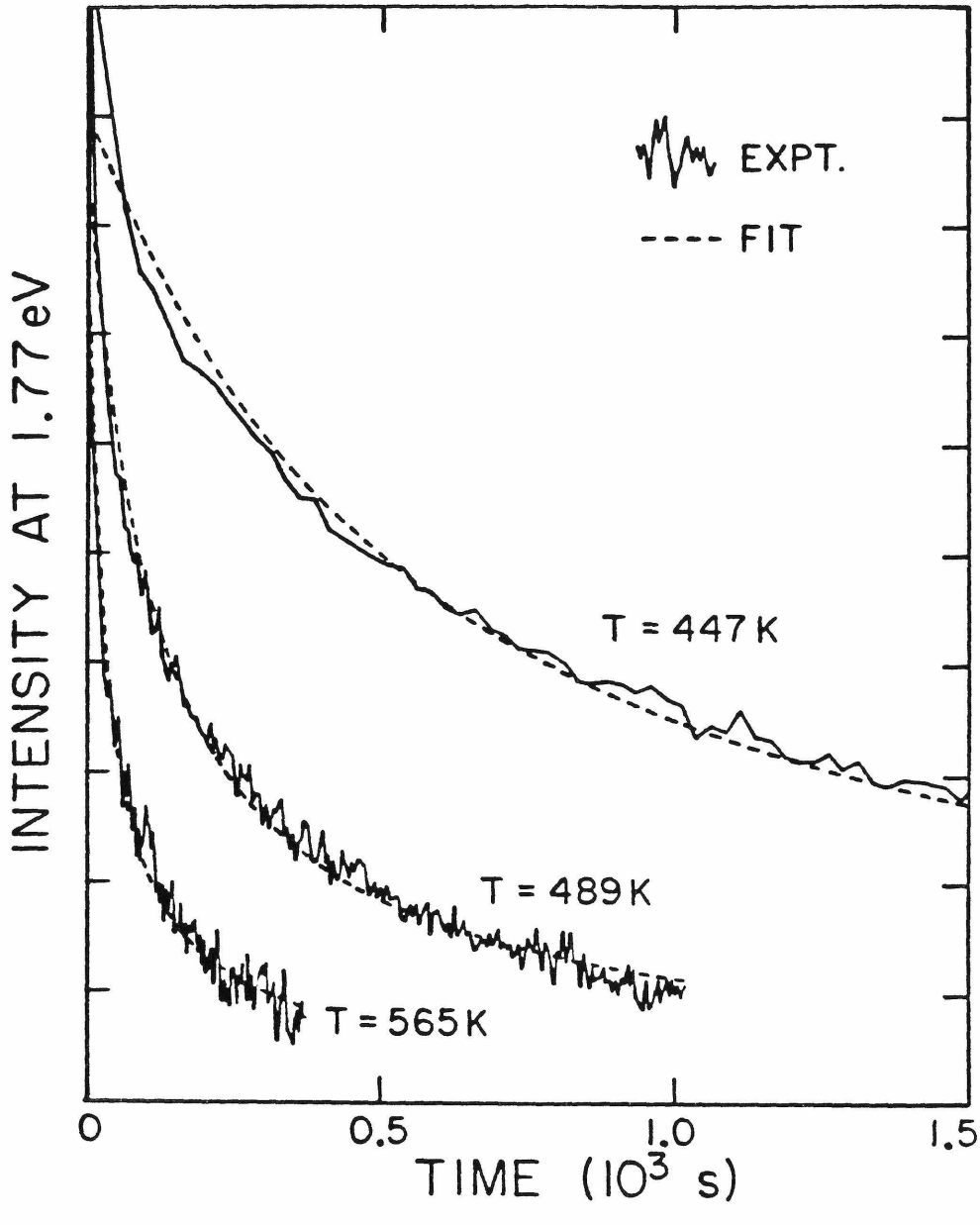


**Figure 3.5:** Decay of the nearest-neighbor $(Zn,O)_{m=1}$ luminescence, at various temperatures $T$. The data have been fit to a theoretical form corresponding to the $f(0,0)\rightarrow 0$ curve shown in Fig. 3.6.

all of the temperatures discussed here. Thus, the final part of the decay curves are not affected by $n_0$ because it is a constant. Therefore, we need not further concern ourselves with the time dependence of $n_0$ or $f_1$.

Let us now derive a functional form for the observed decay curves. From Eqs. (3.3-3.7) we find that the electron occupation of the $(Zn,O)_1$ centers is given by

$$f(\rho,z)=f(0,0)\frac{\exp\left(\frac{-\rho^2}{2\sigma^2}-\alpha z\right)}{\left[1+f(0,0)\exp\left(\frac{-\rho^2}{2\sigma^2}-\alpha z\right)\right]}, \tag{3.9}$$

where we have dropped the subscript '1'. We assume that the dissociation rate of a given center is proportional to its occupation. This assumption is justified below. Thus, the concentration of $(Zn,O)_1$ centers at $(\rho,z)$ varies with time according to

$$N(\rho,z,t)=N(0)\exp(-f(\rho,z)rt), \tag{3.10}$$

where $r$ is the reaction rate and $N(0)$ is the spatially uniform impurity concentration at $t=0$. From Eqs. (3.8)–(3.10) the total intensity of $(Zn,O)_1$ luminescence can be evaluated to be

$$I(t)=\frac{N(0)f(0,0)\sigma^2}{\alpha\tau^{rad}}\int_0^1 du\ \ln(1/u)\frac{\exp\left[\frac{-f(0,0)urt}{1+f(0,0)(u-1)}\right]}{1+f(0,0)(u-1)}. \tag{3.11}$$

Figure 3.6 shows several examples of Eq. (3.11) for various values of $f(0,0)$. For $f(0,0)\rightarrow 1$ the decay is purely exponential. This corresponds to an infinitely large excitation region with uniform occupation of all the centers. For $f(0,0)\rightarrow 0$ the decay follows an exponential integral form. In our experiments $f(0,0)<0.9$. From Fig. 3.6 we see that Eq. (3.11) is quite well approximated by its $f(0,0)\rightarrow 0$ limit:

$$I(t)\approx\frac{a}{r_0t}(\gamma+\ln(r_0t)+E_1(r_0t))+b, \qquad f(0,0)<0.9 \tag{3.12}$$

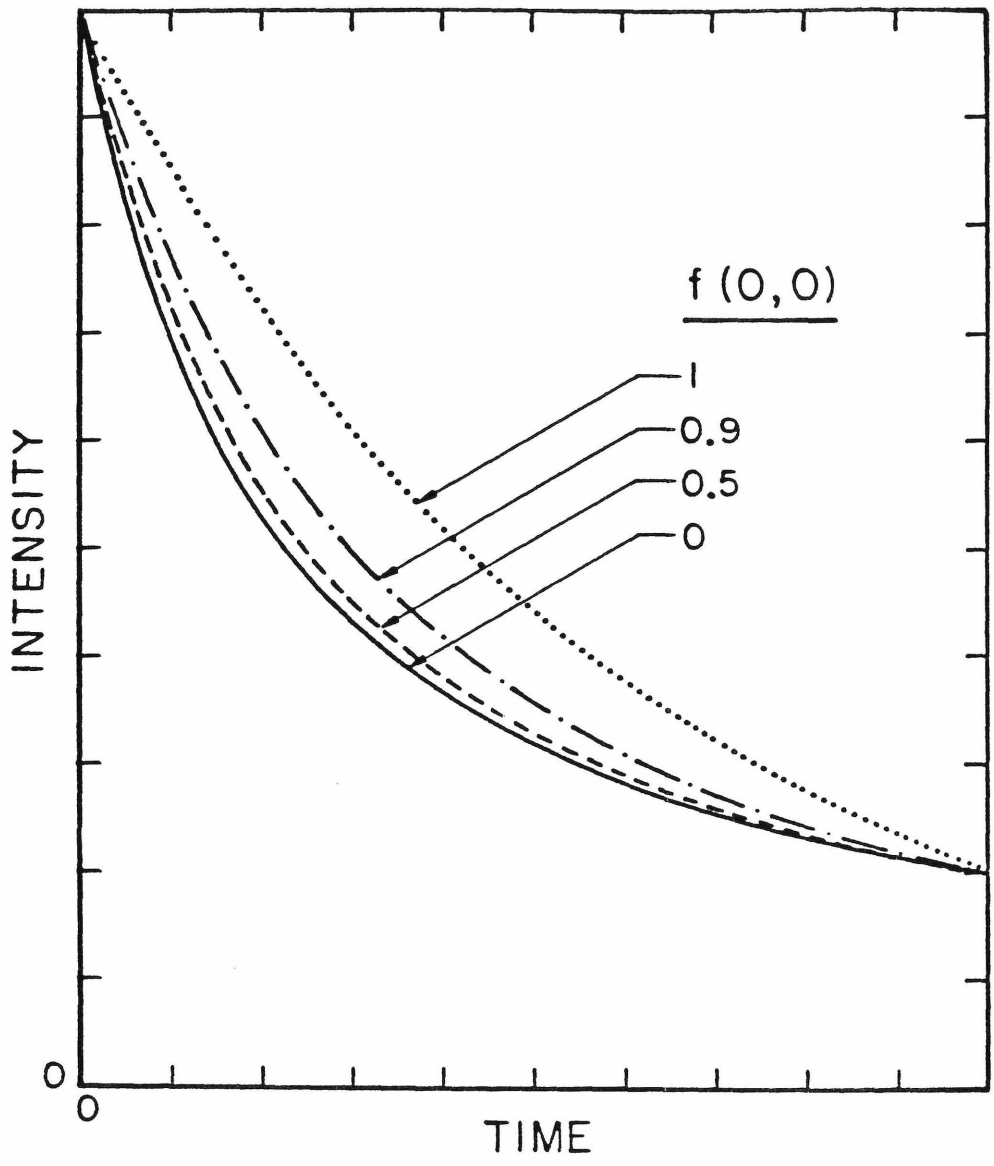


**Figure 3.6:** Theoretical curves for the decay of the $(Zn,O)_{m=1}$ luminescence. $f(0,0)$ is the maximum electron occupation of the centers. $f(0,0)\rightarrow 1$ for very large laser powers and $f(0,0)\rightarrow 0$ for small laser powers. For the experiments described here, $f(0,0) < 0.9$.

where $a$ is a constant, $\gamma$ is Euler's constant, $r_o = f(0,0)r$ is the observed decay rate, and $E_1$ is an exponential integral of the first kind. To this form, we have added another constant $b$ to account for the background intensity due to $(Zn,O)_{m>1}$. Equation (3.12) provides a good fit to all of the observed decay curves.

The data shown in Fig. 3.5 were fit to the functional form Eq. (3.12). The decay curves shown in the figure have had a background intensity $b$ (determined from the fit) subtracted from them. The decay rates determined from the fits are plotted in Fig. 3.7 versus the incident laser power. At low powers the rates increase linearly with power, at high powers the rates approach some limit: the saturated decay rate. The decay rates saturate when the electron occupation saturates. This justifies the above assumption that the dissociation rate is proportional to the electron occupation. The saturation power level increases with temperature as expected from Eq. (3.4b). The fact that the decay rates do indeed saturate provides evidence that sample heating and large hole concentrations due to the laser excitation are not significantly affecting our results.

The saturated decay rates are plotted versus temperature in Fig. 3.8. We find an activation energy of $0.60 \pm 0.07$ eV with a pre-exponential factor of approximately $3 \times 10^4$ $s^{-1}$. Similar activation energies have been observed in other GaP:(Zn,O) degradation studies[3,5]. For the data in Fig. 3.8 we have not included any corrections to the temperature due to sample heating since these corrections produce a negligible change to the activation energy within the quoted uncertainties. In addition to measuring the activation energy for the photoinduced reaction, we have also measured the barrier for the nearest-neighbor dissociation to proceed by purely thermal means. The procedure consisted of observing the absolute intensity of luminescence (at 1.77 eV) from a sample,

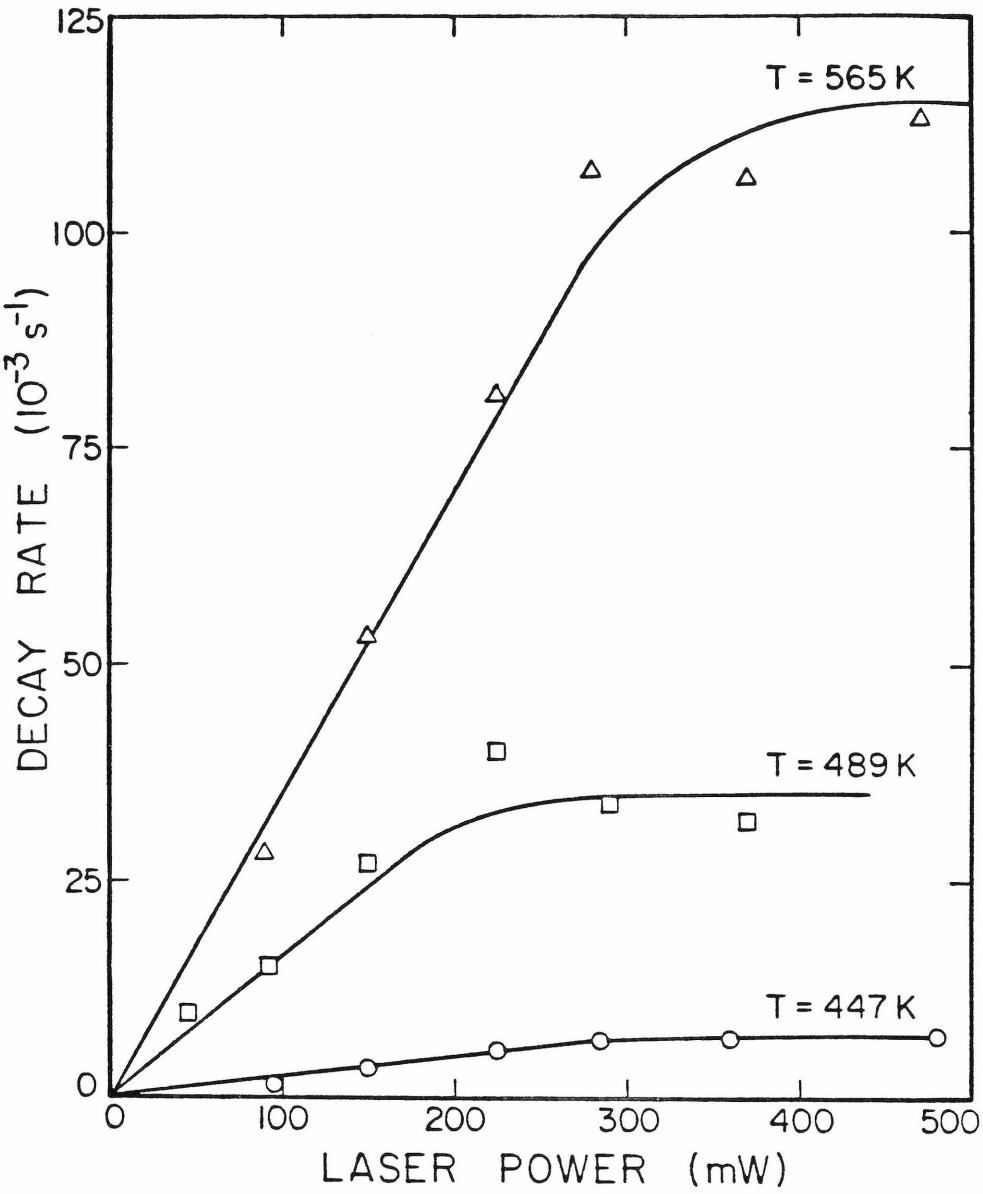


**Figure 3.7:** The decay rates of the $(Zn,O)_{m=1}$ luminescence versus the laser power, at various temperatures $T$. For high powers the decay rates saturate due to saturation of the electron occupation of the centers. The solid lines are drawn as a guide to the eye.

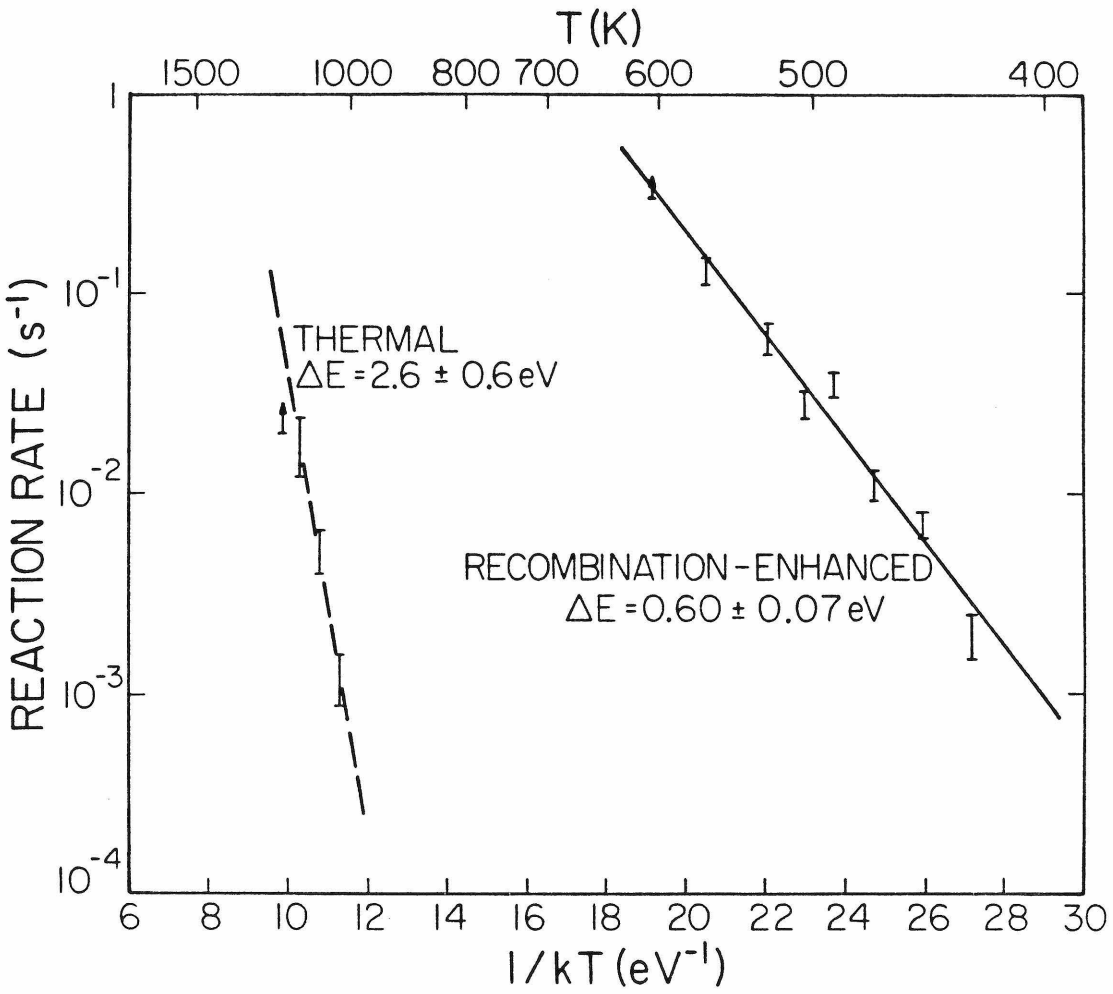


**Figure 3.8:** The dissociation rates of $(Zn,O)_{m=1}$ pairs. The rates labeled "recombination-enhanced" are for photoinduced dissociation of the pairs, in the limit of high laser power. The rates labeled "thermal" are for pair dissociation by purely thermal means.

putting it in a furnace for some amount of time, removing, quenching and etching the sample, and finally observing again the luminescence intensity. The annealing temperatures were greater than 600 °C (the initial state of the crystal[2]) and so the luminescence intensity decreased with annealing time due to dissociation of the nearest-neighbor pairs[9]. The resulting exponential decay rates are shown in Fig. 3.8. The activation energy is $2.6 \pm 0.6$ eV with a pre-exponential factor of approximately $10^{10}$ $s^{-1}$. This activation energy represents the barrier for dissociation of $(Zn,O)_1$ without a bound electron on the center (let us call this the ground state of the center).

## 3.5 MECHANISMS FOR THE REACTIONS

Now let us consider what mechanisms may be responsible for the photoinduced dissociation reaction. From the literature[7,23] we identify two mechanisms which have been observed in other systems. First, the $(Zn,O)_1$ dissociation could be a "recombination-enhanced" defect reaction (REDR) in which energy available from electron-hole recombination is transferred to defect vibrational modes, leading to a reaction. This is the mechanism we believe to cause the reactions observed here. The activation energy of 0.60 eV we identify roughly as the difference between the thermal barrier ($2.6 \pm 0.6$ eV) and the recombination energy ($\sim$1.9 eV). Since all of the recombination energy is used in surmounting the barrier, the reaction is the result of nonradiative recombination by multi-phonon-emission (MPE). Although MPE recombination has not been reported for $(Zn,O)_1$ it has been reported[6] for isolated O and it seems likely that it also occurs for $(Zn,O)_1$. If we assume that the 0.60 eV activation energy belongs to the MPE recombination rate, then the fraction of nonradiative recombination events which lead to a pair

dissociation is estimated to be $10^{-4}$ (roughly, this is the value of $\eta$ defined in Ref. 7).

The second mechanism which must be considered is a "charge state" reaction in which the $(Zn,O)_1$ dissociation would occur thermally from the excited state of the complex in which the bound electron is present. At high laser powers the pairs are almost always in this state. The observed 0.60 eV would be identified as the thermal reaction barrier for the excited state. This is rather different than the ground state barrier of 2.6 eV. Furthermore, the observed $3 \times 10^4$ $s^{-1}$ is about nine orders of magnitude less than a phonon frequency. This implies a multi-jump process in which the (Zn,O) pair dissociates and recombines $10^9$ times before permanently dissociating, or in which a third particle is needed for the reaction and must diffuse to the site. Although we cannot prove that these processes are not occurring, we consider them to be unlikely and we prefer the simpler explanation of the recombination-enhanced reaction.

The strong electron-phonon coupling required for a recombination-enhanced reaction is clearly evident in the photoluminescence spectra. As shown in Fig. 3.2(b), the $(Zn,O)_{m=1}$ band is very broad (due to a series of phonon replicas which are all smeared together). This strong coupling suggests that the dissociation reaction may proceed without the presence of any additional defects. Thus, it seems quite likely that the oxygen (or zinc) simply jumps from its substitutional site to an interstitial site and migrates away. The mobile ion is subsequently captured by a vacancy to form a $(Zn,O)_m$ pair with the nearest zinc (or oxygen) ion. The observed activation energy of 0.60 eV will in general contain contributions from each of the processes; dissociation, diffusion, and re-formation. From Fig. 3.8 it is clear that the observed reaction is a first order kinetic process. Also, as shown in Fig. 3.2(a) the $(Zn,O)_{m>1}$ pairs form at exactly the same rate as the

$(Zn,O)_{m=1}$ pairs dissociate. Thus, the rate limiting process is the dissociation, and the observed rates are indeed the rates for dissociation. We emphasize that it is the dissociation of the pairs which we believe to be a photoinduced reaction. The subsequent diffusion and re-formation can probably occur thermally at the temperatures considered here.

## 3.6 CONCLUSIONS

In this chapter we have given a detailed description of photoinduced reactions between nearest-neighbor zinc and oxygen impurities in gallium phosphide. We have shown that under conditions of laser excitation at elevated temperatures, the nearest-neighbor (Zn,O) pairs dissociate and subsequently re-form as further separated pairs. This reaction can be written as

$$(Zn,O)_{m=1} \rightarrow (Zn,O)_{m>1} . \tag{3.13}$$

We have identified the mechanism for this reaction by measurements of the dissociation rates. The observed luminescence decay curves are analyzed by a model of the electron-hole recombination kinetics which includes the effects of saturation and a spatially dependent generation rate. From the resulting dissociation rates, in the limit of high laser power, the activation energy for the photoinduced dissociation is found to be $0.60 \pm 0.07$ eV. We also observe dissociation of the pairs by purely thermal means, with an activation energy of $2.6 \pm 0.6$ eV. From these activation energies along with the observed pre-exponential factors, we conclude that the dissociation is a recombination-enhanced defect reaction. A nonradiative electron-hole recombination event puts the $(Zn,O)_{m=1}$ center into a highy excited vibronic state, resulting in the dissociation. The atomic motion in the dissociation and re-formation is not well understood. However, we propose that

in the dissociation the oxygen (or zinc) ion jumps to an interstitial site. This interstitial ion then diffuses thermally some short distance and is captured by a vacancy to form a pair with the nearest zinc (or oxygen) ion.

## REFERENCES


1. J. J. Hopfield, D. G. Thomas, and M. Gershenzon, *Phys. Rev. Lett.* **10**, 162 (1963).
2. R. H. Saul, J. Armstrong and W. H. Hackett, Jr., *Appl. Phys. Lett.* **15**, 229 (1969).
3. A. A. Bergh, *IEEE Tran. on Electron Devices* **18**, 166 (1971).
4. P. D. Dapkus and C. H. Henry, *J. Appl. Phys.* **47**, 4061 (1976).
5. C. H. Henry and P. D. Dapkus, *J. Appl. Phys.* **47**, 4067 (1976).
6. C. H. Henry and D. V. Lang, *Phys. Rev. B* **15**, 989 (1977).
7. L. C. Kimerling, *Solid State Electron.* **21**, 1391 (1978).
8. H. F. Wolf, *Semiconductors* (Wiley, New York, 1971), p. 84.
9. A. Onton and M. R. Lorenz, *Appl. Phys. Lett.* **12**, 115 (1968).
10. T. N. Morgan, B. Welber, and R. N. Bhargava, *Phys. Rev.* **166**, 751 (1968).
11. C. H. Henry, P. J. Dean and J. D. Cuthbert, *Phys. Rev.* **166**, 754 (1968).
12. P. J. Dean, C. H. Henry, and C. J. Frosch, *Phys. Rev.* **168**, 812 (1968).
13. Our calculations use $E_g = 2339$ meV, $E_A = 64$ meV, $E_D = 893$ meV, $\epsilon = 11.1$, $a_0 = 5.45$ Å for type-II geometry, and a Van der Waals coefficient of zero.
14. J. S. Prener, *J. Chem. Phys.* **25**, 1294 (1956).
15. J. D. Cuthbert, C. H. Henry, and P. J. Dean, *Phys. Rev.* **170**, 739 (1968).
16. J. S. Jayson, *J. Appl. Phys.* **41**, 3854 (1970).
17. R. N. Bhargava, *J. Appl. Phys.* **41**, 9 (1970).
18. J. M. Dishman, M. DiDomenico, Jr., and R. Caruso, *Phys. Rev. B* **2**, 1988 (1970).
19. J. S. Jayson, R. N. Bhargava, and R. W. Dixon, *J. Appl. Phys.* **41**, 4972 (1970).

20. J. S. Jayson and R. Z. Bachrach, *Phys. Rev. B* **4**, 477 (1971).

21. C. H. Henry, R. Z. Bachrach, and N. E. Schumaker, *Phys. Rev. B* **8**, 4761 (1973).

22. D. V. Lang and L. C. Kimerling, *Appl. Phys. Lett.* **28**, 248 (1976).

23. P. J. Dean and W. J. Choyke, *Adv. Phys.* **26**, 1 (1977).

# CHAPTER 4

# EXCITON CAPTURE CROSS SECTIONS IN Si:In,B

## 4.1 INTRODUCTION

### 4.1.1 Bound Excitons in Silicon

Free electrons and holes in semiconductor crystals can interact amongst themselves, and with impurities, to form a variety of multi-particle complexes[1]. A free electron and free hole experience an attractive Coulomb interaction, and they bind to form a free exciton (FE). These FE are neutral particles. They are free to move around in the crystal, and at sufficiently low densities they form a gas of noninteracting particles (at higher densities they condense into an electron-hole droplet[2]). If there are impurities in the crystal, then the FE may bind onto them. In silicon, bound exciton (BE) complexes consisting of a FE bound to a *neutral* donor or acceptor are observed[3]. The neutral impurity consists of a charged ion-core plus a bound electron or hole. In the simplest view, the attractive interaction between the neutral impurity and the FE is a Van der Waals type interaction. The resulting BE consists of a total of three mobile charged particles centered around the charged ion-core. If the FE density is high enough, an impurity may bind more than one exciton, resulting in bound multiexciton complexes[4].

During the past several years studies have been made on the process by which free excitons (FE) in a semiconductor crystal are captured on impurity sites to form bound excitons (BE). The luminescence resulting from radiative recombination of a bound exciton in silicon was first observed about twenty years ago[3], but only recently have attempts been made to measure the cross section (which characterizes the capture rate) for FE capture. Knowledge of the capture cross sections for many impurities is necessary in order to use exciton photoluminescence as a quantitative tool for determining impurity concentrations in semiconductors[5—7].

To date, FE capture processes have been studied in detail only in silicon. Elliott *et. al.*[8] observed the In BE lifetime in the temperature range 10—30 K and deduced values for the In cross section $\sigma_{In}$ which have a temperature dependence of roughly $T^{-4}$ with $\sigma_{In} \approx 10^{13}$ cm$^2$ at 10 K. Hammond and Silver[9] assume a cross section of $(10^{-12}$ cm$^2$K$)/T$ for B and P impurities in silicon, and show that this value is consistent with their observations of the FE lifetime and BE to FE intensity ratios, in the temperature range 2 — 16 K. Nakayama *et. al.*[6] report a value of $1.51 \times 10^{-14}$ cm$^2$ for the B cross section at 4.2 K.

### 4.1.2 Results of this Work

In this work, measurements are reported for the BE luminescence decay rates and intensity ratios in silicon doped with In and B. From these data, values are deduced for the exciton capture cross sections of In and B in the temperature range 3.6 — 5.9 K. The impurity concentrations of the sample used in these experiments were suitable to permit cross section measurements in this temperature range.

The results indicate that the In cross section shows a strong temperature dependence, increasing to greater than $10^{-12}$ cm$^2$ at 3.6 K. We believe that this temperature dependence is due to excited states of the In BE. The B cross section is found to be about $10^{-13}$ cm$^{-2}$ for $T \approx 5$ K, in agreement with the Hammond and Silver estimate. The ratio of B BE release rate to capture rate is shown to agree with simple detailed balance results using a ground state binding energy of $3.3 \pm 0.2$ meV.

### 4.1.3 Outline of Chapter

In Section 4.2.1 we describe the samples and the apparatus used to measure the lifetime of the BE luminescence lines. The results of the lifetime measurements are presented in Section 4.2.2. To relate these lifetimes to the capture

cross sections, it is necessary to understand the various capture and recombination mechanisms for the excitons in the system. In Section 4.2.3 we present a quantitative theory of the exciton recombination kinetics. Rate equations are formulated which describe the capture, release, and recombination of the excitons. We are able to obtain an analytic solution of these equations in the form of a linear eigenvalue problem. The principle of detailed balance is used in Section 4.2.4 to reduce the number of unknowns in the rate equations. In Section 4.2.5 the cross sections for FE capture are computed from the observed lifetimes. The In cross section is observed to have a relatively strong temperature dependence. In Section 4.3 we discuss this behavior in terms of excited states of the In BE. The conclusions of this work are presented in Section 4.4.

## 4.2 Kinetic Measurements

### 4.2.1 Experimental

Measurements were made on a single crystal float-zoned silicon sample doped with In and B. The impurity concentrations were determined by Hall effect measurements to be $6.8 \times 10^{12}$ cm$^{-3}$ and $3.5 \times 10^{13}$ cm$^{-3}$ respectively[10]. The residual P concentration was determined to be $0.9 \times 10^{13}$ cm$^{-3}$. The sample was mounted in a variable temperature cryostat. Optical excitation was provided by an $Ar^+$ laser with an opto-acoustic coupler to provide pulses of variable width. The beam was unfocussed, with a diameter of approximately 2 mm. Observations of the B BE decay rate were usually made using 2 $\mu$s pulses with a 0.2% duty cycle. Average power levels were always less than 5 mW, which was determined to result in less than 0.1 K sample heating. Continuous mode laser operation was used for observations of the intensity ratios. The luminescence wavelength

was selected with a SPEX 1269 single-pass spectrometer and photon counting was accomplished with a cooled S-1 photomultiplier. A time-to-pulse-height converter was used for decay rate measurements. The photomultiplier response as a function of wavelength was calibrated using a 1500 K black body source. All data were acquired on a Nuclear Data ND-60 multichannel analyzer and then passed to a PDP 11/34 computer for storage on floppy disk.

### 4.2.2 Luminescence Decay Rates

Figure 4.1 shows a typical photoluminescence spectrum of Si:In,B. The B(TO) line at 1.0928 eV and the In (NP) line at 1.1409 eV were used for the decay rate observations. In general, the decay rates of these BE luminescence lines depend on all the kinetic processes occurring in the system. Once the FE are created by the laser excitation, they can bind onto impurities, they can be released from impurities, or they can recombine. As will be shown, the BE decay curves (intensity versus time) are the sum of several exponentials, the decay time of each exponential being affected by all of these kinetic processes.

Figure 4.2 shows the observed decay rates of the BE luminescence lines. For $T < 7$ K the In and B BE decay curves appear to be single exponentials. Roughly speaking, the In BE decay rate equals the capture rate of FE on In sites, and the B BE decay rate is the sum of the recombination rate (Auger decay) and the release rate of the BE. As the temperature increases the FE population increases (relative to the BE) and the decay curves of the In BE, B BE, and FE all start to resemble each other. The major component of the resulting decay curve is due to FE recombination, which does not contain any information about the cross sections. For $T < 3$ K the B BE decay rate equals (within experimental error) the Auger decay rate, so that the B BE release rate is too small to measure and the associated cross section cannot be calculated. Thus, only for $3 < T < 7$ K do

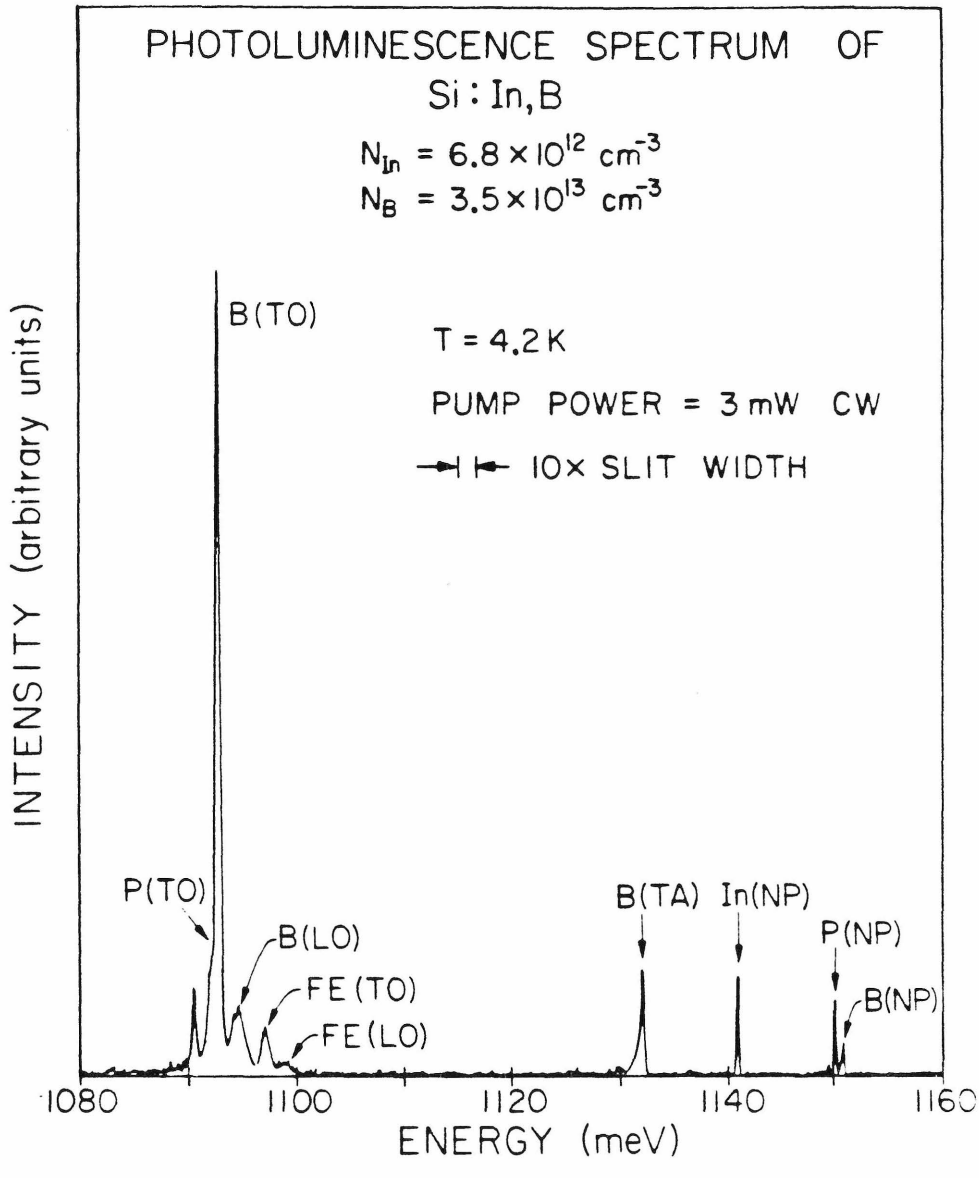


**Figure 4.1:** A typical photoluminescence spectrum of Si:In,B. A 3 mW unfocussed $Ar^+$ laser was used for optical excitation. The bound exciton luminescence lines are labelled by the impurity (B, P, or In), with the symbol in brackets referring to the type of phonon involved in the transition (NP=no-phonon, TA=transverse-acoustic, TO=transverse-optical, and LO=longitudinal-optical).

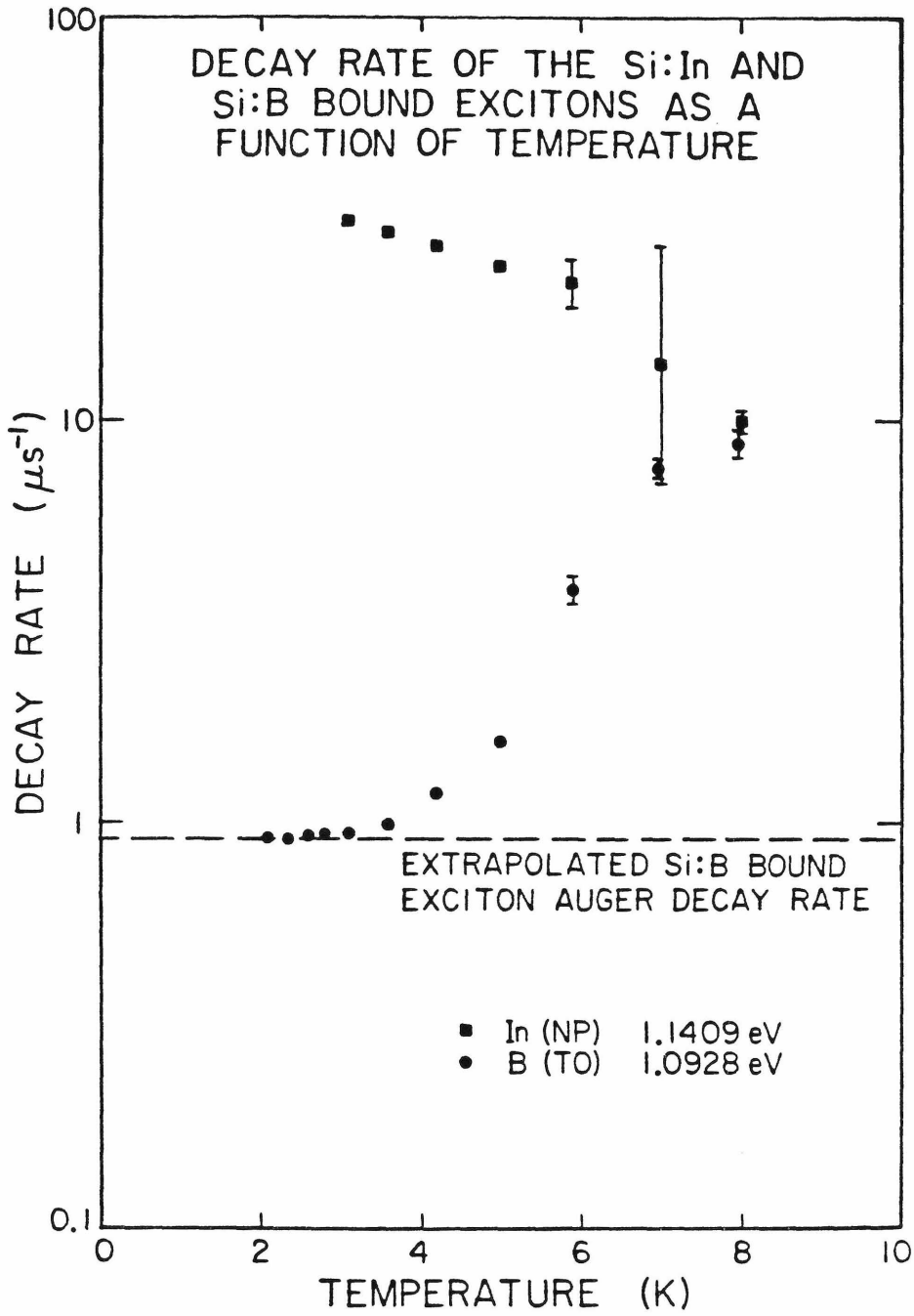


**Figure 4.2:** Decay rates of the In(NP) and B(TO) luminescence lines. Below 5 K the observed decays were exponential and the error bars are too small to show. Above 5 K the observed decays appeared to be the sum of several exponentials, with decay rates in the indicated range.

the observed decay rates yield the kinetic information required for computation of the cross sections.

### 4.2.3 Exciton Recombination Kinetics

Let us now investigate how the cross sections can be calculated from the observed decay rates of the luminescence lines. The observed intensity $I$, of the luminescence arising from a particular exciton state, is linearly related to the concentration of occupied states $n$, by

$$I = \frac{\mathcal{R}}{\tau^{rad}} n, \tag{4.1}$$

where $\mathcal{R}$ is the collection efficiency, which is determined by the sample characteristics and the efficiency of the photon collection system. The radiative decay rate $1/\tau^{rad}$ is proportional to the oscillator strength $f$ of the transition. The occupation of the exciton states is determined by a set of coupled kinetic equations[9] which describes the effect of exciton capture, release and recombination at neutral impurities. In the limit of low FE concentrations (low laser power), the role of bound multiexciton complexes can be neglected and the resulting equation for the FE (subscript 0) is

$$\frac{dn_0}{dt} = g - \frac{n_0}{\tau_0} - n_0 \sum_i C_i(N_i - n_i) + \sum_i R_i n_i, \tag{4.2a}$$

where $n_0$ is the FE concentration, $n_i$ is the concentration of excitons bound on impurity type $(i)$, $N_i$ is the concentration of impurity type $(i)$, g is the FE generation rate, $C_i$ and $R_i$ are the capture and release rates of excitons on impurity type $(i)$, and $\tau_0$ is the FE recombination lifetime. For BE of concentration $n_i$ $(i = 1, 2, \ldots)$, the rate equations are

$$\frac{dn_i}{dt} = -\frac{n_i}{\tau_i} + n_0 C_i(N_i - n_i) - R_i n_i, \tag{4.2b}$$

where $\tau_i$ is the BE recombination lifetime. For BE in silicon, Auger decay is the dominant recombination mechanism. For low exciton concentrations (*i.e.* when the impurities are far from saturation), these equations may be linearized by taking the concentration of unoccupied impurities ($N_i - n_i$) to be equal to the total concentration of impurities $N_i$. For the case of interest *viz.* decay following an optical pulse, $g = 0$ in Eq. (4.2a). With these two simplifications, the solution of Eq. (4.2) for the case of $m$ impurity types can be written as

$$\mathbf{n} = \sum_{i=0}^{m} a_i \mathbf{Z}_i e^{\lambda_i t}, \tag{4.3}$$

where

$$\mathbf{n} = \begin{bmatrix} n_0 \\ n_1 \\ \vdots \\ n_m \end{bmatrix}.$$

$\mathbf{Z}_i$ are the eigenvectors and $\lambda_i$ the eigenvalues of the fundamental matrix **A** formed from the coefficients of the concentrations in Eq. (4.2). The $a_i$ are constants determined by the initial conditions. For the case of two impurity types and the FE,

$$\mathbf{A} = \begin{bmatrix} -\frac{1}{\tau_0} - C_1 N_1 - C_2 N_2 & R_1 & R_2 \\ C_1 N_1 & -\frac{1}{\tau_1} - R_1 & 0 \\ C_2 N_2 & 0 & -\frac{1}{\tau_2} - R_2 \end{bmatrix}. \tag{4.4}$$

This matrix has three negative eigenvalues. Thus, the exciton concentrations will be composed of three decaying exponentials. The amplitudes of the exponentials are determined by the initial conditions, which for the case of decay following a long optical pulse will be the steady-state solutions of Eq. (4.2).

Once the fundamental matrix **A** is known it is straightforward to calculate its eigenvalues, which are equal to the experimentally observed decay times. For the case of In (subscript 1) and B (subscript 2) impurities, let us examine which

parameters in Eq. (4.4) are known. The FE recombination time $\tau_0$ is not very well-known and could be spatially dependent. Since these experiments were conducted at relatively low temperatures the results were not very dependent on $\tau_0$, and in all calculations $\tau_0$ was varied in the range $2 - 1000$ $\mu$s. The In BE Auger time $\tau_1$ was taken to be 3 ns[11] but the results are insensitive to this value (one of the eigenvalues of **A** is always very close to $-(3\text{ ns})^{-1}$ and contains no useful kinetic information). The B BE Auger time $\tau_2$ has been extrapolated from low temperature measurements[12] (see Fig. 4.2) and is $1/\tau_2 = 0.91 \pm 0.02$ $\mu s^{-1}$. The $T = 3.6$ K results to be presented later in this work are somewhat sensitive to this Auger rate, although the higher temperature results are not. The capture rates $C_i$ are related to the capture cross sections $\sigma_i$ by

$$C_i = \sigma_i v_{th}, \tag{4.5}$$

where $v_{th}$ is the FE thermal velocity. The mean velocity will be used here,

$$v_{th} = \left( \frac{8kT}{\pi m_{ex}} \right)^{1/2} \tag{4.6}$$

where $m_{ex}$ is the FE mass ($0.6\ m_o$)[8]. The cross sections $\sigma_i$ in Eq. (4.5) are the major unknowns in this work. Roughly speaking, by measuring two eigenvalues of **A** we can deduce $\sigma_1$ and $\sigma_2$. As will be discussed in the following section, the release rate $R_i$ can be related to the capture rates $C_i$ using detailed balance. We find that $R_1$ is negligibly small for the temperatures used here. $R_2$ is computed from $C_2$, but only with the use of one additional parameter ($E_2$). This parameter is the third unknown, and a luminescence intensity ratio is measured in order to determine its value.

**4.2.4 Detailed Balance**

Let us consider a system which consists of some population of species which can exist in either free states or bound states. The free species are captured into

the bound states, and the bound species are released into the free states. We assume that our system is in contact with some large heat bath (*e.g.* phonons) which provides the energy for the release process, and absorbs the energy from the capture process. Clearly there is some similar physics involved in the capture and release processes. The principle of detailed balance[30] tells us that the actual transition probabilities (matrix elements) for capture and release are equal. If the capture rate is large, then the release rate should also be large (just how large depends on the temperature and possibly other quantities). Thus, we expect some sort of proportionality to exist between the release and capture rates. This type of relationship goes under the general title of "mass-action". Here, we will derive this relationship for our system of free excitons (FE) and bound excitons (BE).

Excitons in semiconductors undergo various kinetic processes other than just capture and release. As shown in Eq. (4.2), the FE are generated and can recombine, and the BE can also recombine. However, the ratio of release to capture rate should not depend on these additional processes. In other words, the *probability* per unit time for release or capture should be independent of whatever other kinetic processes exist (but the *number* of particles released or captured per unit time clearly depends on all of the kinetics). Thus, the release to capture ratio in the real system should be equal to the release to capture ratio in some imaginary system in which the generation and recombination channels do not exist. Let us call this latter system the "long-lived" system (since the species have an infinite lifetime in this system). Our preceding remarks can be summarized as

$$\left(\frac{R}{C}\right)_{real} = \left(\frac{R}{C}\right)_{long\text{-}lived}, \tag{4.7}$$

where $R$ is the release rate and $C$ is the capture rate. This equation is the basic assumption of detailed balance. The arguments which led us to this assumption

are rather subtle. However, in our case we believe Eq. (4.7) to be valid as long as the system is truly in equilibrium with a large heat bath, and possibly as long as the concentration of free species is not too large.

The long-lived exciton system can be described as

$$\mathrm{BE} \leftrightarrow \mathrm{FE} + \mathrm{A}^0 \tag{4.8}$$

where $\mathrm{A}^0$ refers to a neutral acceptor. In analogy with Eq. (4.2), the rate equation for both the FE and the BE in this long-lived system, in steady-state, is given by

$$0 = n_0 C(N - n) - Rn, \tag{4.9}$$

where $n_0$ is the FE concentration, $n$ is the BE concentration, and $N$ is the total acceptor concentration. By rewriting Eq. (4.9), we find that

$$\left(\frac{R}{C}\right)_{long\text{-}lived} = \left(\frac{(N-n)}{n} n_0\right)_{long\text{-}lived}. \tag{4.10}$$

The quantity on the right-hand side of this equation can be computed using statistical mechanics. The FE are described using a spherical band of degeneracy $g_0$ and effective-mass $m_{ex}$. We assume that the occupation of the band can be described by a classical occupation factor; $\exp[-(E-\mu)/kT]$. The concentration of FE is then computed to be

$$n_0 = \int_0^\infty \exp[-(E-\mu)/kT] \frac{g_0}{4\pi^2} \left(\frac{2m_{ex}}{\hbar^2}\right)^{3/2} \sqrt{E}\, dE \tag{4.11a}$$

$$= g_0 \left(\frac{m_{ex} kT}{2\pi\hbar^2}\right)^{3/2} \exp(\mu/kT), \tag{4.11b}$$

where $\mu$ is the chemical potential. The concentration of BE is computed using a grand-canonical-ensemble of discreet levels with energy $-E$ and degeneracy $g$. Neglecting the probability for multiple occupation, we find that

$$\frac{n}{(N-n)} = g \exp(E/kT) \exp(\mu/kT). \tag{4.12}$$

By combining Eqs. (4.7)-(4.12), the release to capture ratio (in the real system or the long-lived system) is found to be

$$\frac{R}{C} = K(T) = \frac{g_0}{g}\left(\frac{m_{ex}kT}{2\pi\hbar^2}\right)^{3/2} \exp(-E/kT), \tag{4.13}$$

where $K(T)$ is defined here as an "equilibrium constant". Finally, by evaluating the degeneracy factors and adding a subscript $i$ to denote the impurity type, the equilibrium constant is computed to be

$$K_i = \frac{4 \cdot 24[1 + \exp(\Delta E_0/kT)]}{12 + 60\exp(-\Delta E_i/kT)}\left(\frac{m_{ex}kT}{2\pi\hbar^2}\right)^{3/2} \exp(-E_i/kT), \tag{4.14}$$

where $\Delta E_0 = 0.31$ meV is the splitting of the FE ground state [13,14] (degeneracy of 24 in each of the upper and lower states), $\Delta E_i$ is the J-J splitting of the BE ground state (degeneracy of 12 and 60 in the lower and upper states respectively), and $E_i$ is the BE binding energy. For In, $E_1 = 13.7$ meV, and for the temperature range used in these experiments the In release rate is negligibly small. The reported values of the B BE binding energy are $4.2 \pm 0.2$ [15], $3.8 \pm 0.2$ [16], $3.9 \pm 0.3$ [4], and $3.6 \pm 0.5$ meV[4]. For discussion we will use the value $E_2 = 3.9 \pm 0.3$ meV. The 8% uncertainty in $E_2$ results in almost an order of magnitude uncertainty in the factor $\exp(-E_2/kT)$ (for $3 < T < 7$ K). For this reason, the value of $E_2$ (and then of $K_2$) is treated as an unknown in the calculations.

**4.2.5 Analysis of Observed Data**

The theoretical decay rates of the BE luminescence lines are given by the eigenvalues of **A**, Eq. (4.4). As discussed in the previous sections, this matrix contains three unknowns; the In cross section $\sigma_1$, the B cross section $\sigma_2$, and the B equilibrium constant $K_2$. The purpose of these experiments is to determine these three parameters, as a function of temperature, based on measurements of the decay times and intensity ratios of various luminescence lines. In particular,

the quantities which are measured are two eigenvalues of the matrix Eq. (4.4), and the intensity ratio, $I_{In}/I_B$ of the B(TO) line to the In(NP) line. The observed values of $I_{In}/I_B$ were corrected for photomultiplier response, and were related to a concentration ratio using a B(TO) oscillator strength of $2.8 \times 10^{-5} \pm 10\%$[17] and an In(NP) oscillator strength of $8.5 \times 10^{-5} \pm 10\%$[18]. This concentration ratio is related to the unknowns through the eigenvectors of Eq. (4.4) and the steady-state solutions of Eq. (4.2). The procedure used to analyze the data was to calculate as a function of $K_2$, values for $\sigma_1$, $\sigma_2$ and $I_{In}/I_B$ based on the observed decay rates. The observed value of $I_{In}/I_B$ was then used to determine the appropriate range of $K_2$ consistent with experiment, and using these $K_2$ values the cross sections were determined. This procedure was repeated at each temperature.

The results for the B equilibrium constant $K_2$ are in agreement with the theoretical predictions of Eq. (4.14) using a binding energy $E_2 = 3.3 \pm 0.2$ meV and a splitting $\Delta E_2 = 0$. This binding energy is about 20% lower than the values observed by other authors. Most of these other values were obtained using spectroscopic line positions, and do not rely on the use of detailed balance. One possible source of the observed 20% discrepancy is that Eq. (4.14) is too simple, since it neglects effects such as anisotropic FE bands and excited states of the BE resonant with FE states.

Shown in Fig. 4.3 are the cross sections measured in these experiments, along with previously reported values [6,8,9]. The error bars on the cross sections are the result of uncertainties in the various quantities used in the calculations, and include possible errors due to the residual P in the sample. We see that the In cross section continues to show a strong temperature dependence down to $T \approx 5K$, in contrast with the mild temperature dependence of the B cross

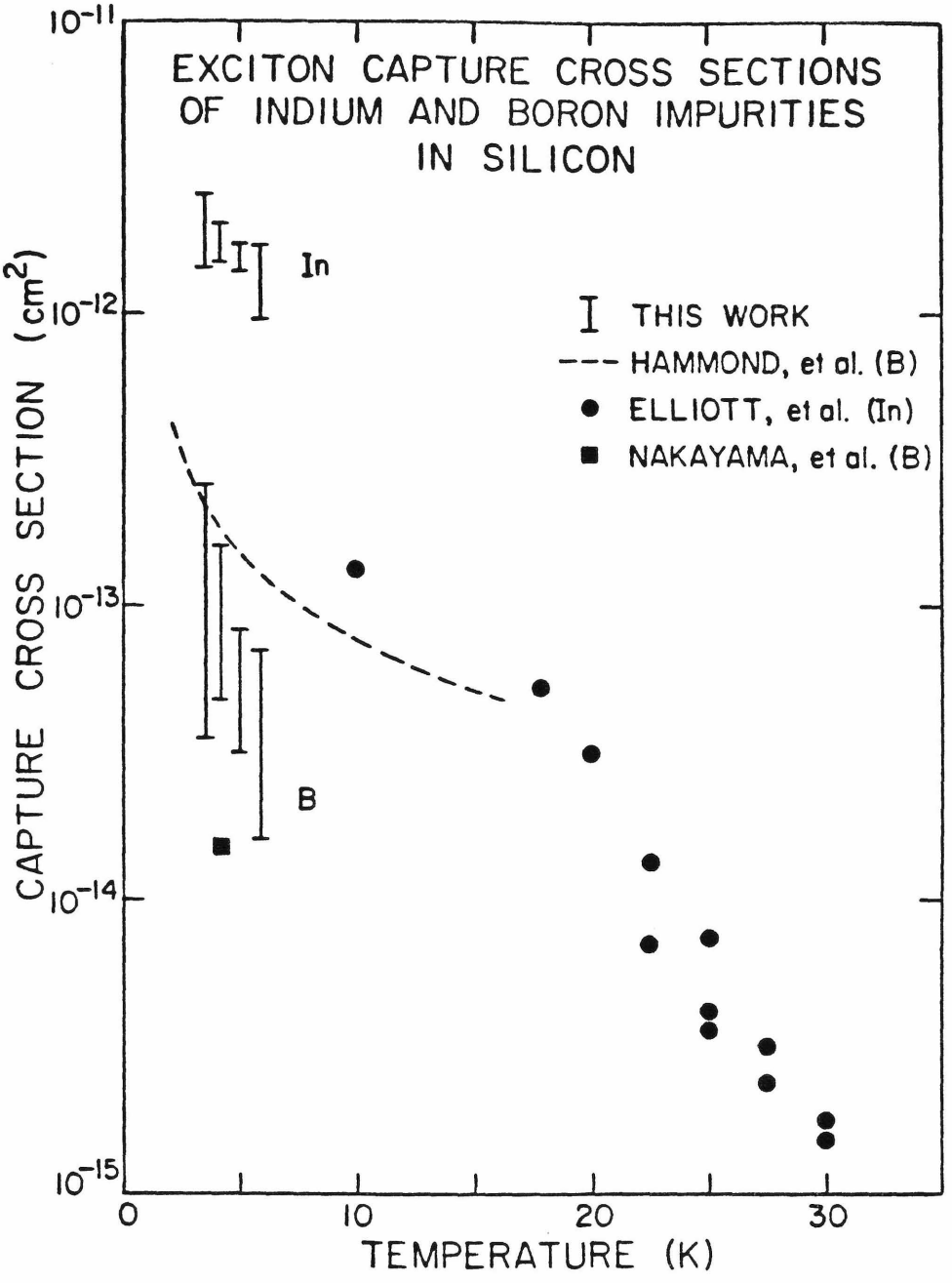


**Figure 4.3:** The observed capture cross-sections of free excitons on indium and boron impurities in silicon, as a function of temperature. The In cross-section has roughly a $T^{-4}$ temperature dependence, whereas the B cross-section has a $T^{-1}$ dependence.

section. The B cross section measured here appears to be somewhat smaller than the Hammond and Silver estimate, although the difference is not significant within experimental error. It is surprising to see that for $T \approx 5K$, the B cross section is an order of magnitude less than the In cross section. This is opposite to what is expected from consideration of BE ground state binding energy, since the In BE is more tightly bound than the B BE and hence should have a smaller capture cross section.

### 4.3 Excited States of the Bound Exciton

In the previous section we have presented results for the In and B BE capture cross sections. We observe that the In cross section has a much stronger temperature dependence than that of B, and at low temperatures $\sigma_{\mathrm{In}}$ is an order of magnitude larger than $\sigma_{\mathrm{B}}$. In an effort to explain these large differences between the In and B cross sections, let us consider excited states of the BE and what effect these states may have on the results presented here. The spatial extent of an excited state is large compared to the ground state, and so the probability of capture into these states should also be large. However, a particle which is captured into an excited state will have a relatively large probability for being thermally released back into the free states. At zero temperature, the total cross section for particle capture will simply be the sum of the cross sections of all states. At increased temperatures, the higher lying excited states will not be effective since the particles captured into these states will usually be immediately released. Thus, excited states lead to a temperature dependent cross section which could be rather large at low temperatures.

The BE spectrum for Si:In and Si:B has been previously investigated using

both luminescence and absorption [15,17,19—21]. For Si:In a low energy triplet structure (ground state plus two excited states) has been observed as well as two highly excited states [19]. For Si:B the ground state appears to be split into a triplet[21], and no other excited states have been observed. Calculations by Chang and McGill[22] indicate that the excitation energy of the $2s$ excited state of the outer particle, for the case of Si:In, is comparable to the BE binding energy so that the state might be bound. For Si:B the calculations indicate that this state is definitely not bound. Inner particle excitations and multiple-particle excitations may provide bound excited states.

It is straightforward to incorporate excited states into the rate equations (4.2). One simply writes an equation for each state, the population of the states being related by the transition rates between bound states and the transition rates from bound to free states. A more common procedure (especially for the case of electron-donor capture) is to analyze the decay rates (eigenvalues) on the basis of a single-level model with one rate equation for the free species and one rate equation for each bound species. The resulting capture cross sections are then interpreted as total cross sections and are compared with that computed from the theory of cascade capture, first developed by Lax[23], and extended by many authors [24—28]. Roughly speaking, the theory of cascade capture says that those levels bound by energies greater than $kT$ (lower levels) will contribute to the capture process whereas those levels bound by energies less than $kT$ (upper levels) do not contribute to the total capture cross section. Particles captured in lower levels are seen as rapidly losing their energy via phonon emission and moving down to the ground state. Particles captured in upper states are quickly ejected into the free states via phonon absorption. The total cross section $\sigma_t$ is computed from the cross sections of the individual levels $\sigma_j$ by

$$\sigma_t = \sum_j S_j \sigma_j, \tag{4.15}$$

where $S_j$ is the sticking probability of the $j^{th}$ level, defined as the probability that a particle captured in the $j^{th}$ level will reach the ground state before being ejected into the free states. $S_j$ is close to unity for the lower levels and close to zero for the upper levels.

It is clear that the total cross section defined by Eq. (4.15) is in no way rigorously related to that computed from experiment. As was originally pointed out by Lax, the very concept of a sticking probability implicitly makes some assumptions about the transition rates in the system, such that the captured particle reaches the ground state, or escapes, in a time that is small compared to the decay times in the experiment[23]. The validity of replacing a complete set of rate equations with just a single equation (for each impurity type) has been examined by Pickin[28] for the case of electron-donor capture. He shows that if the impurity concentration is low enough then the single rate equation is valid, with the capture rate being interpreted as a total capture rate (due to cascade capture) and the release rate as a total release rate (due to inverse- cascade). Direct calculation indicates that these total capture and release rates are related by detailed balance, using the ground state binding energy[29]. The reason that the ground state plays such an important role, even if most capture and release is via excited states, is that most of the population of the bound species resides in the ground state. Thus, when analyzing data in order to produce cross sections, it is only necessary to use one rate equation for each impurity type and one equation for the free species (*e.g.* as done in Eq. (4.2)) even if there are excited states in the spectrum. Also, detailed balance (using ground-state energies) can be used to relate release and capture rates. The resulting cross sections must be interpreted as total cross sections (in the sense of Eq. (4.15)) and may contain

small dependences on seemingly unrelated parameters, due to the approximations involved in defining a total cross section.

Now let us consider the case of interest, namely, acceptor bound excitons in silicon. The cross section of a single level $\sigma_j$ is the integral over occupied FE states of the cross section for capture of a FE of energy $\epsilon$ into the $j^{th}$ level $\sigma_{j\epsilon}$:

$$\sigma_j(T) = \int_0^\infty f(\epsilon, T)\sigma_{j\epsilon}N(\epsilon)d\epsilon, \tag{4.16}$$

where $f(\epsilon, T)$ is the occupation of FE states and $N(\epsilon)d\epsilon$ is the density of FE states. This equation will result in some temperature dependence of the $\sigma_j$, although $\sigma_{je}$ is not temperature dependent and is related to the matrix element of the electron-phonon interaction between neutral acceptor with FE state and the BE state. It seems reasonable that the temperature dependence expressed by Eq. (4.16) could account for the observed temperature dependence of the B cross section (see Fig. 4.3). However, the rapid variation with temperature of the In cross section must be due to highly excited states whose sticking probabilities contain the temperature dependence. The fact that the In cross section still varies rapidly at temperatures as low as 5 K suggests that the relevant excited states are bound by energies as small as about 1 meV. The 1.1544 eV line observed by Elliott *et. al.*[19] for Si:In probably plays an important role in determining the magnitude of the capture cross section.

### 4.4 Conclusions

In conclusion, we have measured the boron BE equilibrium constant (ratio of release to capture rates) and the boron and indium FE capture cross sections, in silicon, for the temperature range 3.6 — 5.9 K. The B BE equilibrium constant is shown to agree with detailed balance results using a ground state binding energy

of $3.3 \pm 0.2$ meV. The In cross section is found to be quite temperature dependent, increasing to greater than $10^{-12}$ cm$^2$ at 3.6 K. The B cross section about $10^{-13}$ cm$^2$ for $T \approx 5$ K. The strong temperature dependence of the In cross section, compared to that of B, probably results from highly excited states of the In BE.

## REFERENCES


1. J. I. Pankove, *Optical Processes in Semiconductors* (Dover Publications, New York, 1971), p. 12*f*.
2. G. A. Thomas, T. M. Rice, and J. C. Hensel, *Phys. Rev.* **33**, 219 (1974).
3. J. R. Haynes, *Phys. Rev. Lett.* **4**, 361 (1960).
4. S. A. Lyon, D. L. Smith, and T. C. McGill, *Phys. Rev. Lett.* **41**, 56 (1978).
5. M. Tajima, *Appl. Phys. Lett.* **32**, 719 (1978).
6. H. Nakayama, T. Nishino, and Y. Hamakawa, *Jap. J. of Appl. Phys.* **19**, 501 (1980).
7. G. S. Mitchard and T. C. McGill, *Appl. Phys. Lett.* **37**, 959 (1980).
8. K. R. Elliott, D. L. Smith, and T. C. McGill, *Solid State Comm.* **24**, 461 (1978).
9. R. B. Hammond and R. N. Silver, *Appl. Phys. Lett.* **36**, 68 (1980).
10. Hall effect measurements were performed at Hughes Research Laboratories.
11. W. Schmid, *Phys. Stat. Sol.(b)* **84**, 529 (1977).
12. The uncertainty in the Auger rate $1/\tau_2$ is estimated by calculating the difference between the B BE luminescence decay rate $r_2$ and the Auger rate for a very large range of capture cross sections and BE binding energies. The results demonstrate that $|r_2 - 1/\tau_2| < 0.005\mu s^{-1}$ for $T < 2.2$ K.
13. R. B. Hammond and R. N. Silver, *Solid State Comm.* **28**, 993 (1978).
14. J. C. Merle, M. Capizzi, P. Fiorini, and A. Frova, *Phys. Rev.* **B17**, 4821 (1978).
15. M. A. Vouk and E. C. Lightowlers, *J. of Luminescence* **15**, 357 (1977).
16. M. L. W. Thewalt, G. Kirczenow, R. R. Parsons, and R. Barrie, *Can. J. Phys.* **54**, 1728 (1976).
17. P. J. Dean, W. F. Flood, and G. Kaminsky, *Phys. Rev.* **163**, 721 (1967).

18. G. C. Osbourn and D. L. Smith, *Phys. Rev.* **B16**, 5426 (1977).

19. K. R. Elliott, G. C. Osbourn, D. L. Smith, and T. C. McGill, *Phys. Rev.* **B17**, 1808 (1978).

20. P. J. Dean, J. R. Haynes, and W. F. Flood, *Phys. Rev.* **161**, 711 (1967).

21. M. L. W. Thewalt, *Can. J. Phys.* **55**, 1463 (1977).

22. Y. C. Chang and T. C. McGill, *Solid State Comm.* **32**, 319 (1979).

23. M. Lax, *Phys. Rev.* **119**, 1502 (1960).

24. G. Ascarelli and S. Rodriguez, *Phys. Rev.* **124**, 1321 (1961).

25. R. A. Brown and S. Rodriguez, *Phys. Rev.* **153**, 890 (1967).

26. F. Belezany and G. Pataki, *Phys. Stat. Sol.* **13**, 499 (1966).

27. W. Pickin, *Solid State Elec.* **21**, 309 (1978).

28. W. Pickin, *Solid State Elec.* **21**, 1299 (1978).

29. D. L. Smith, unpublished. For the case of several closely spaced states near the ground state, the concept of a sticking probability must be generalized to include capture into such states as a "true capture event", and these states are assumed to be in thermal equilibrium amongst themselves.

30. F. Reif, *Fundamentals of Statistical and Thermal Physics*, (McGraw-Hill, New York, 1965), p. 383.

# CHAPTER 5

# VIBRATIONAL MODES OF OXYGEN IN GaP

## 5.1 INTRODUCTION

### 5.1.1 Phonon Spectroscopy

The photoluminescence spectra of defects in semiconductors often contain information about the vibrational modes of the defect. As was discussed in Section 1.3.2, "phonon replicas" of the main no-phonon luminescence line are observed in the spectra. These phonon-assisted lines are shifted from the no-phonon line by the energy of the particular phonon involved. Thus, the spectrum directly yields phonon energies, and in this sense can be regarded as a type of phonon spectroscopy. If the optical transition produces significant changes in the local electronic configuration of the defect, then the phonons which are excited will be characteristic of the defect itself (rather than the bulk crystal). This is often the case for "deep-level" defects in semiconductors. The observation and identification of the defect phonon modes yields information about the bond strengths and atomic configuration near the defect.

A defect vibrational mode can be roughly defined as a mode in which the amplitude of vibration in the vicinity of the defect is much larger than the amplitude far away from the defect. For a *localized* mode, the vibrational amplitude falls to zero as we move away from the defect. A localized mode occurs at some energy where no bulk modes appear. For a *resonant* mode, all of the atoms in the crystal vibrate with nonzero amplitude. However, in some range of energies the atoms near the defect may vibrate with a much enhanced amplitude. If this range of energies is small, we then have a "narrow" resonance which may be observed as a sharp spectral peak. If the energy range is large, we have a "broad" resonance which will probably not be observed. One quantity which effectively describes defect modes is the *local density-of-states*. Roughly, this is just the fraction of a state which is concentrated near some point in space (*e.g.*

the defect). Localized modes show up as $\delta$-functions in the local density-of-states, and resonant modes appear as peaks with some nonzero width. For particular types of experiments, the local density-of-states can be rigorously related to the observed quantity[1]. For our purposes, it will suffice to examine the local density-of-states itself.

For the case of oxygen in gallium phosphide, it is resonant vibrational modes which are observed in experiment. The calculations to be presented in this chapter were undertaken in an effort to understand the nature of these phonon resonances. The computational technique used is that of Green's functions. The first step in the computation is to calculate the normal modes of the perfect crystal. The defect is then introduced as a localized perturbation, and the vibrational modes of the imperfect crystal are evaluated. The Green's function method has been widely used in the evaluation of defect vibrational modes[1—9]. For the case of substitutional defects in zinc-blende crystals these applications have generally been concerned with localized phonons. Here we will be mainly concerned with resonant phonons. In particular, we will concern ouselves with the coupling between the vibrations of the defect and those of the bulk crystal. If this coupling is strong then the defect phonon will be quite extended in space and will probably not be observed in experiments. However, those defect phonons which are weakly coupled to the lattice may be observed. This investigation of the coupling ("width") of the resonances is a unique aspect of this work.

Let us consider the spectrum of phonons which may be observed for some defect in a crystal. What information can be obtained from the defect phonons? The energy of the phonons is determined by the mass and spring constants of the defect, along with the energies of the bulk phonons. For the case of a defect of known symmetry and known chemical type, we obtain information about the

strength of the bonds in the vicinity of the defect. However, it is often the case that the symmetry and/or chemical type of the defect is *not* known. Then the interpretation of the defect phonons is more difficult. Perhaps the phonon spectrum can be used to identify the type of defect. This immediately leads us to the following question: *how many* defect modes exist for some given type of defect? We are not so much concerned about the energies of the modes — the real question concerns the existence of modes and an assignment of their symmetries. In this chapter we will specialize to the case of oxygen in gallium phosphide, and so the question we will address is: *how many* defect vibrational modes exist for a substitutional impurity in a zinc-blende lattice? To answer this question, we must concern ourselves with the nature of the defect and the coupling between the defect and the bulk crystal. The number of defect modes depends on this coupling. We will use a simple model to describe the bulk crystal and the defect. Within this model, the vibrational modes of the entire system are evaluated exactly, and we will investigate the amplitude of these modes in the vicinity of the defect.

### 5.1.2 Defect Reactions

The intensity of phonon replicas observed in luminescence spectra is related to the change in the atomic configuration which occurs in the optical transition[10]. If a large change occurs in the value of some collective coordinate, then the associated phonon replicas will be very intense. Thus, by understanding the nature of the defect phonons which are observed in the spectrum, we learn about the ways in which the atoms move in the electronic transition.

In Chapter 3 we have argued that the dissociation of nearest-neighbor (Zn,O) pairs in GaP is due to some large amplitude vibration which is excited upon electron-hole recombination at the defect. This mechanism implies the existence

of some very intense phonon modes in the luminescence spectrum. These intense modes are indeed observed. The broad band seen in Fig. 3.2(b) for the $(Zn,O)_{m=1}$ DA luminescence is due to a series of phonon replicas. Although the band shown in Fig. 3.2(b) is featureless, other workers[11] have been able to resolve a 6.0 meV ripple on the high energy edge of the band. For the case of $(Cd,O)_{m=1}$ pairs[12], the phonon replicas are clearly resolved and most of the luminescence is contained in a 7.2 meV replica. We conclude that the broad $(Zn,O)_{m=1}$ band is due mainly to 6.0 meV replicas. This mode is very strongly coupled to the electronic transition and so it is almost certain that this mode leads to the dissociation of the nearest neighbor (Zn,O) pairs. Thus, by identifying the nature of this 6.0 meV mode we can gain a better understanding of the atomic motion which occurs when the nearest-neighbor pairs dissociate. The calculations presented in this chapter represent the first step towards identifying this 6.0 meV mode.

### 5.1.3 Results of this Work

The purpose of this work is to understand the vibrational modes of defects in crystals. The defect we will consider consists of an O atom on a P-site in GaP. The number of defect modes depends on the force constants of the springs which connect the impurity to its neighbors. For values of the defect force constants less than those of the bulk, we find two defect vibrational modes, one with $A_1$ symmetry and the other with $T_2$ symmetry. Depending on the force constants, these modes may be localized, or resonant with the bulk phonons. These results compare well with experiment, in which we observe two resonant modes. From the energy of the observed modes we find that the strength of the O-Ga springs is roughly 50% of the P-Ga springs. This suggests that O in GaP is a weakly bonded defect.

### 5.1.4 Outline of Chapter

The general theory of Green's functions as applied to the problem of the vibrational states of crystal defects will be discussed in Section 5.2. Symmetry considerations are presented in Section 5.2.1. The defect we are considering consists of a substitutional impurity atom together with its four nearest-neighbor atoms. This 5-atom cluster is described by 15 cartesian coordinates, leading to $15 \times 15 = 225$ elements in the Green's function matrix. By defining appropriate collective coordinates for the cluster, the number of independent matrix elements can be reduced to only 9. In Section 5.2.2, we present the two-parameter model which is used to describe the bulk phonons. The dynamical matrix for the system is derived, and the eigenvalues and eigenvectors of this matrix give the normal modes of the perfect crystal. In Section 5.2.3, we define the Green's function for the perfect crystal and we show how this can be used in the evaluation of the vibrational modes of the defect. The actual computation of the Green's function is discussed in Section 5.2.4. The perturbation which defines the defect in the crystal is given in Section 5.2.5.

The results of our calculations are presented in Section 5.3. We show the computed dispersion curves and density-of-states for the bulk phonons in GaP. The values for the two parameters in our model were chosen to give good agreement between the calculated phonon energies and the real energies. The P-site Green's functions are presented in Section 5.3.2. The local density-of-states for the $A_1$ and $T_2$ defect vibrational modes are shown in Section 5.3.3. For reduced values of the defect force constants, we find one $A_1$ defect mode and one $T_2$ defect mode. The energies of these modes are quite close to those obtained from an approximate solution to the problem. A comparison between theory and experiment is given in Section 5.3.4. The conclusions which can be drawn from

this work are presented in Section 5.4.

## 5.2 GENERAL THEORY

### 5.2.1 Symmetry Considerations

The labelling of the bulk phonon modes is determined by the space group of the crystal. The translational symmetry of the perfect crystal results in vibrational modes which are plane-waves, labelled by their wave-vector **k**. The values of **k** can be restricted to the first Brillouin zone. The shape of this zone is determined by the rotation symmetry (point group) of the Bravais lattice. Here we will be considering zinc-blende crystals for which the Bravais lattice is face-centered-cubic and the first Brillioun zone is a truncated octahedron[13]. The zinc-blende crystal has two atoms per unit cell, resulting in a total of six branches in the dispersion curves; three acoustic branches and three optical branches.

The symmetry of an imperfect crystal (perfect crystal plus a defect) is most easily seen by considering a small molecule which includes the defect and its neighboring atoms. For the case of a substitutional defect in a zinc-blende crystal this molecule consists of a 5-atom cluster with $T_d$ symmetry, as shown in Fig. 5.1(a). The positions of the 5 atoms are specified by 15 cartesian coordinates. These coordinates form a 15-dimensional representation of the $T_d$ group. This reducible representation $\Gamma$ can be decomposed into the irreducible representations of the $T_d$ group according to

$$\Gamma = A_1 + E + T_1 + 3T_2. \tag{5.1}$$

This equation classifies the collective coordinates of the 5-atom cluster. These coordinates are very useful for describing the motion of the molecule. The coordinates which we will use here are shown in Fig. 5.1(b) and 5.1(c). The

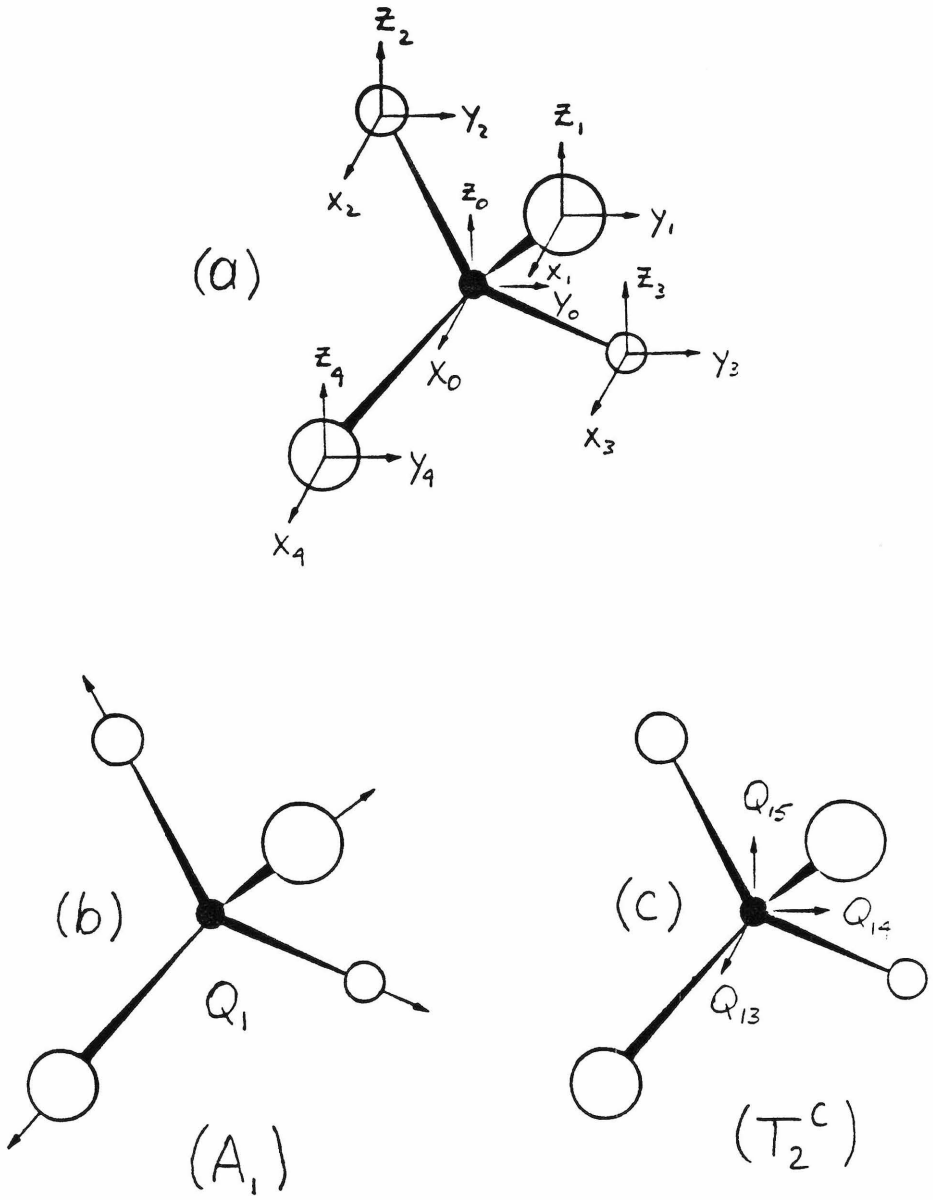


**Figure 5.1:** Coordinates for a five-atom defect with tetrahedral symmetry; (a) cartesian coordinates of the atoms, (b) an $A_1$ collective coordinate consists of radial motion of the outer atoms in a "breathing mode", and (c) motion of the inner atom which forms a $T_2$ collective coordinate.

$A_1$ coordinate consists of a "breathing" type of motion in which the central atom is stationary and the outer atoms move radially. In terms of the cartesian coordinates shown in Fig. 5.1(a), the $A_1$ coordinate can be expressed as

$$Q_1 = \frac{1}{\sqrt{12}}(x_1 + y_1 + z_1 - x_2 - y_2 + z_2 - x_3 + y_3 - z_3 + x_4 - y_4 - z_4). \quad (5.2)$$

The motion of the central atom, as shown in Fig. 5.1(c), forms a basis for a $T_2$ representation of the $T_d$ group. This $T_2$ coordinate is simply expressed as

$$Q_{13} = x_0, \quad Q_{14} = y_0, \quad Q_{15} = z_0. \quad (5.3)$$

The other two sets of $T_2$ coordinates involve particular types of motion of the outer atoms. Similarly, the $E$ and $T_1$ coordinates involve motion of the outer atoms with the inner atom stationary. The definition of all the collective coordinates is given in Table 5.1.

The description of the normal modes of a point defect in a crystal is greatly facilitated by the use of the collective coordinates described above. As will be discussed in Sections 5.2.3 and 5.2.4, the lattice dynamics is described by a Green's function matrix, with elements $G_{ij}$. Initially $i$ and $j$ label cartesian coordinates of each atom. The 5-atom defect molecule is described by a $15 \times 15$ block of the Green's function. This $15 \times 15$ matrix will be block diagonalized by transforming to the collective coordinates $Q$. The transformed matrix consists of $1 \times 1$, $2 \times 2$, $3 \times 3$, and $9 \times 9$ blocks for the $A_1$, $E$, $T_1$, and $3T_2$ representations respectively. Futhermore, the matrix elements do not depend on the row or column of the representation, so that these blocks can be further reduced to $1 \times 1$, $1 \times 1$, $1 \times 1$, and $3 \times 3$ blocks respectively; for a total of 9 independent matrix elements. Thus, using symmetry the $15 \times 15 = 225$ matrix elements of the Green's function in the space of the defect have been reduced to only 9 independent elements.

**Table 5.1:** Collective coordinates for a 5-atom tetrahedral molecule. The collective coordinates $Q$ are expressed in terms of the cartesian coordinates $(x, y, z)$ of each atom. The collective coordinates form bases for the irreducible representations of the $T_d$ group as indicated.

$A_1$:

$$Q_1 = (x_1 + y_1 + z_1 - x_2 - y_2 + z_2 - x_3 + y_3 - z_3 + x_4 - y_4 - z_4)/\sqrt{12}$$

$E$:

$$Q_2 = (-x_1 - y_1 + 2z_1 + x_2 + y_2 + 2z_2 + x_3 - y_3 - 2z_3 - x_4 + y_4 - 2z_4)/\sqrt{24}$$
$$Q_3 = (x_1 - y_1 - x_2 + y_2 - x_3 - y_3 + x_4 + y_4)/\sqrt{8}$$

$T_1$:

$$Q_4 = (-y_1 + z_1 - y_2 - z_2 + y_3 + z_3 + y_4 - z_4)/\sqrt{8}$$
$$Q_5 = (+x_1 - z_1 + x_2 + z_2 - x_3 + z_3 - x_4 - z_4)/\sqrt{8}$$
$$Q_6 = (-x_1 + y_1 + x_2 - y_2 - x_3 - y_3 + x_4 + y_4)/\sqrt{8}$$

$T_2^a$:

$$Q_7 = (+2x_1 - y_1 - z_1 + 2x_2 - y_2 + z_2 + 2x_3 + y_3 - z_3 + 2x_4 + y_4 + z_4)/\sqrt{24}$$
$$Q_8 = (-x_1 + 2y_1 - z_1 - x_2 + 2y_2 + z_2 + x_3 + 2y_3 + z_3 + x_4 + 2y_4 - z_4)/\sqrt{24}$$
$$Q_9 = (-x_1 - y_1 + 2z_1 + x_2 + y_2 + 2z_2 - x_3 + y_3 + 2z_3 + x_4 - y_4 + 2z_4)/\sqrt{24}$$

$T_2^b$:

$$Q_{10} = (x_1 + y_1 + z_1 + x_2 + y_2 - z_2 + x_3 - y_3 + z_3 + x_4 - y_4 - z_4)/\sqrt{12}$$
$$Q_{11} = (x_1 + y_1 + z_1 + x_2 + y_2 - z_2 - x_3 + y_3 - z_3 - x_4 + y_4 + z_4)/\sqrt{12}$$
$$Q_{12} = (x_1 + y_1 + z_1 - x_2 - y_2 + z_2 + x_3 - y_3 + z_3 - x_4 + y_4 + z_4)/\sqrt{12}$$

$T_2^c$:

$$Q_{13} = x_0$$
$$Q_{14} = y_0$$
$$Q_{15} = z_0$$

### 5.2.2 Description of Bulk Phonons

In this section we discuss the solution for the vibrational modes of a perfect crystal. The lattice dynamics will be described using a simple two-parameter model. This model consists of nearest-neighbor bond-stretching and bond-bending interactions. The potential energy for the entire lattice is constructed, and from this potential the dynamical matrix is computed. This model gives identical results with those described by Grimm *et. al.*[1]. They derived their dynamical matrix entirely from symmetry considerations and they showed that the model is the most general two-parameter model for a zinc-blende system described entirely by nearest-neighbor interactions.

Consider a lattice containing $N$ unit cells and $r$ atoms per unit cell. The indices $l$ and $m$ will label the cells, and $a$ and $b$ will label the atomic types. A general atom will be labelled by $i$ or $j$. Let the equilibrium position of an atom be denoted by $\mathbf{R}_{la}$, and let its position away from equilibrium be denoted by $\mathbf{u}_{la}$. The atoms are connected to their nearest-neighbors by springs. Each spring is described by a stretching force constant $f_1$ and a bending force constant $f_2$. The total potential for the system can be expressed as a summation over all springs $s$:

$$V = \frac{1}{2} f_1 \sum_s |(\mathbf{u}_{i_s} - \mathbf{u}_{j_s}) \cdot \mathbf{e}_s|^2 + \frac{1}{2} f_2 \sum_s |(\mathbf{u}_{i_s} - \mathbf{u}_{j_s}) \times \mathbf{e}_s|^2, \qquad (5.4a)$$

where

$$\mathbf{e}_s = \frac{\mathbf{R}_{i_s} - \mathbf{R}_{j_s}}{|\mathbf{R}_{i_s} - \mathbf{R}_{j_s}|} \qquad (5.4b)$$

is the direction vector for the $s^{th}$ spring. The terminating atoms of the $s^{th}$ spring are labelled by $i_s$ and $j_s$. The kinetic energy for the system can be expressed as a summation over all atoms $i$:

$$T = \frac{1}{2} \sum_i m_i \left| \frac{d\mathbf{u}_i}{dt} \right|^2, \qquad (5.5)$$

where $m_i$ is the mass of the $i^{th}$ atom.

The normal modes of the system can be obtained immediately from Eqs. (5.4) and (5.5) in the form of a $3rN$-dimensional eigenvalue problem[14]. An expansion of the potential energy is made, and in the limit of small oscillations only the $2^{nd}$-derivative terms are retained,

$$V = \frac{1}{2} \sum_{la\alpha mb\beta} \Phi^{\alpha\beta}_{lm\,ab} u^{\alpha}_{la} u^{\beta}_{mb}, \tag{5.6}$$

where $\alpha$ and $\beta$ label cartesian components ($x, y$ or $z$). The force constants $\Phi$ are given by

$$\Phi^{\alpha\beta}_{lm\,ab} = \frac{\partial^2 V}{\partial u^{\alpha}_{la} \partial u^{\beta}_{mb}}. \tag{5.7}$$

Assuming a harmonic time dependence for $u^{\alpha}_{la}(t)$,

$$u^{\alpha}_{la}(t) = u^{\alpha}_{la} \exp(i\omega t) \tag{5.8}$$

the equations of motion of the perfect lattice can be expressed as

$$\sum_{mb\beta} (m_a \omega^2 \delta_{lm} \delta_{ab} \delta_{\alpha\beta} - \Phi^{\alpha\beta}_{lm\,ab}) u^{\beta}_{mb} = 0. \tag{5.9}$$

This equation can be written more compactly in matrix form as

$$\mathbf{Lu} = \mathbf{0}, \tag{5.10}$$

where $\mathbf{L}$ is a matrix whose elements are the quantities given in brackets in Eq. (5.9), and $\mathbf{u}$ is a vector whose elements are the amplitudes $u^{\alpha}_{la}$. The matrix $\mathbf{L}$ here plays the role of the operator $E - H$ in the electronic (quantum-mechanical) defect problem.

The translational symmetry of the perfect lattice enables us to solve for its vibrational modes in terms of a $3r$-dimensional eigenvalue problem[14]. First we

**Table 5.2:** The dynamical matrix for a zinc-blende lattice. The matrix elements are denoted by $D_{ab}^{\alpha\beta}$ where $\alpha$ and $\beta$ label cartesian coordinates ($x$, $y$, or $z$), and $a$ and $b$ label atomic types (1 or 2). The dynamical matrix is Hermitian, so that $D_{ba}^{\beta\alpha} = D_{ab}^{\alpha\beta^*}$. The spring constants are given by $f_1$ for bond-stretching and $f_2$ for bond-bending. The lattice constant is denoted by $a_o$.

$$D_{aa}^{\alpha\beta} = \delta_{\alpha\beta}\frac{1}{m_a}\left(\frac{4}{3}f_1 + \frac{8}{3}f_2\right)$$

$$D_{12}^{\alpha\alpha} = \frac{1}{\sqrt{m_1 m_2}}\left(\frac{1}{3}f_1 + \frac{2}{3}f_2\right)\cdot$$
$$(-1 - \exp[-ia_o(k_x + k_y)/2] - \exp[-ia_o(k_x + k_z)/2] - \exp[-ia_o(k_y + k_z)/2])$$

$$D_{12}^{xy} = D_{12}^{yx} = \frac{1}{\sqrt{m_1 m_2}}\left(\frac{1}{3}f_1 - \frac{1}{3}f_2\right)\cdot$$
$$(-1 - \exp[-ia_o(k_x + k_y)/2] + \exp[-ia_o(k_x + k_z)/2] + \exp[-ia_o(k_y + k_z)/2])$$

$$D_{12}^{xz} = D_{12}^{zx} = \frac{1}{\sqrt{m_1 m_2}}\left(\frac{1}{3}f_1 - \frac{1}{3}f_2\right)\cdot$$
$$(-1 + \exp[-ia_o(k_x + k_y)/2] - \exp[-ia_o(k_x + k_z)/2] + \exp[-ia_o(k_y + k_z)/2])$$

$$D_{12}^{yz} = D_{12}^{zy} = \frac{1}{\sqrt{m_1 m_2}}\left(\frac{1}{3}f_1 - \frac{1}{3}f_2\right)\cdot$$
$$(-1 + \exp[-ia_o(k_x + k_y)/2] + \exp[-ia_o(k_x + k_z)/2] - \exp[-ia_o(k_y + k_z)/2])$$

construct a dynamical matrix, defined by

$$D_{ab}^{\alpha\beta}(n,\mathbf{k}) = \frac{1}{\sqrt{m_a m_b}} \sum_{l} \Phi_{l0\,ab}^{\alpha\beta} \exp(-i\mathbf{k}\cdot\mathbf{R}_{la}). \tag{5.11}$$

The index $\mathbf{k}$ labels the normal modes, which are plane-waves with wave-vector $\mathbf{k}$. From Eqs. (5.4), (5.6) and (5.11), the dynamical matrix for a zinc-blende lattice can be determined, and the result is given in Table 5.2. The normal modes are then given by the eigenvalues $\omega^2(n,\mathbf{k})$ and eigenvectors $\xi_a^\alpha(n,\mathbf{k})$ of the dynamical matrix,

$$\sum_{b\beta} D_{ab}^{\alpha\beta}(n,\mathbf{k})\xi_b^\beta(n,\mathbf{k}) = \omega^2(n,\mathbf{k})\,\xi_a^\alpha(n,\mathbf{k}), \tag{5.12}$$

where the $3r$ different solutions of this equation are labelled by $n$. The phonon energies are now given by $E_{n\mathbf{k}} = \hbar\omega_{n\mathbf{k}}$ and the atomic vibrational amplitudes in the $(n\mathbf{k})^{th}$ normal mode are given by

$$u_{la}^\alpha(n,\mathbf{k}) = \xi_a^\alpha(n,\mathbf{k})\frac{1}{\sqrt{m_a}} \exp(i\mathbf{k}\cdot\mathbf{R}_{la}). \tag{5.13}$$

### 5.2.3 Green's Function Formalism

The Green's function technique has been generally used in solid-state physics for treating the properties of defects in crystals. The idea of the technique is to solve the defect probem by first considering the normal modes of the perfect crystal. These modes are divided into various types according to the symmetry of the defect. One then constructs a perturbation matrix, which represents the effect of the defect in the crystal. Using this defect perturbation matrix, along with the normal modes of the perfect crystal, the normal modes for the imperfect crystal can be obtained. The size of the matrices involved in this final step depends on the extent of the defect perturbation in the crystal. For a localized defect, the Green's function technique offers significant computational advantages over the direct computation of the normal modes of the imperfect crystal. The general theory

of Green's functions as applied to defect problems has been discussed by many authors[15—20]. Maradudin and co-workers[1,19,20] treat the case of vibrational modes in crystals, and the formalism presented here closely follows their work.

In the previous section we discussed the solution for the normal modes of a perfect crystal. Now let us introduce a defect into the crystal. Let the new **L**-matrix be given by $\mathbf{L} = \mathbf{L}^0 - \delta\mathbf{L}$ where $\mathbf{L}^0$ refers to the perfect crystal. We will refer to $\delta\mathbf{L}$ as the "defect perturbation matrix". Just as in Eq. (5.10), the normal modes of the imperfect crystal are given by those values of $\omega^2$ and $\mathbf{u}$ which satisfy

$$\mathbf{Lu} = (\mathbf{L}^0 - \delta\mathbf{L})\mathbf{u} = \mathbf{0}. \tag{5.14}$$

This equation can be solved by introducing the Green's function for the perfect crystal $\mathbf{G}^0$, which is formally defined as the inverse of $\mathbf{L}^0$:

$$\mathbf{G}^0(\omega^2)\mathbf{L}^0(\omega^2) = \mathbf{1}. \tag{5.15}$$

Assuming that such a $\mathbf{G}^0$ does indeed exist, Eq. (5.14) can be rewritten as

$$\mathbf{G}^0(\mathbf{L}^0 - \delta\mathbf{L})\mathbf{u} = \mathbf{0} \tag{5.16a}$$

$$(\mathbf{1} - \mathbf{G}^0\delta\mathbf{L})\mathbf{u} = \mathbf{0}. \tag{5.16b}$$

This equation as it stands does not offer any particular advantage over Eq. (5.14) since it is still a $3rN$-dimensional eigenvalue problem. However, if the defect perturbation extends over only some small number of atoms, say $n$ atoms, then $\delta\mathbf{L}$ will only contain a small $3n \times 3n$ block of non-zero values. We can partition $\delta\mathbf{L}$, $\mathbf{G}^0$, and $\mathbf{u}$ into those coordinates in the space of the defect and those outside the defect:

$$\delta\mathbf{L} = \begin{pmatrix} \delta\mathbf{l} & \mathbf{0} \\ \mathbf{0} & \mathbf{0} \end{pmatrix}, \quad \mathbf{G}^0 = \begin{pmatrix} \mathbf{g}^0 & \mathbf{G}^0_{12} \\ \mathbf{G}^0_{21} & \mathbf{G}^0_{22} \end{pmatrix}, \quad \mathbf{u} = \begin{pmatrix} \mathbf{u}_1 \\ \mathbf{u}_2 \end{pmatrix}. \tag{5.17}$$

Equation (5.16b) then can be rewritten as

$$(\mathbf{1} - \mathbf{g}^0 \delta\mathbf{l})\mathbf{u}_1 = \mathbf{0} \tag{5.18a}$$

$$\mathbf{G}^0_{12}\, \delta\mathbf{l}\, \mathbf{u}_1 = \mathbf{u}_2. \tag{5.18b}$$

Equation (5.18a) is $3n$-dimensional and thus it is relatively easy to solve. If we denote $\mathbf{q} = (\mathbf{1} - \mathbf{g}^0 \delta\mathbf{l})$, then the solutions of Eq. (5.18a) are given simply by

$$\det\mathbf{q} = 0. \tag{5.19}$$

So far we have assumed that $\mathbf{G}^0$ as defined by Eq. (5.15) does indeed exist. This is true for energies outside of the allowed energy bands. However, for energies inside the bands, Eq. (5.15) clearly cannot be satisfied since $\mathbf{L}^0(\omega^2_{n\mathrm{k}})$ has a zero eigenvalue and therefore has no inverse. Formally, this problem is avoided by adding a small imaginary part to $\omega^2$; $\omega^2 \rightarrow \omega^2 + i\epsilon$, and later taking the limit $\epsilon \rightarrow 0^+$. Physically, the problem can be interpreted in terms of scattering theory, in which the defect is viewed as a scattering center of incident waves. For certain values of $\omega^2$ the defect may have a very large scattering cross-section. Alternatively, we can maintain a picture similar to localized modes but now all of the atoms in the system vibrate with non-zero amplitude. A resonant mode is one in which the defect atoms vibrate with significantly larger amplitude relative to atoms far away. Whereas a localized mode exists for only one discrete value of $\omega^2$, resonant modes exist for some range of $\omega^2$ values. A characteristic of a resonant mode is its "width" in terms of $\omega^2$ or $\omega$. Narrow (small width) resonances will generally be experimentally observable whereas broad (large width) resonances will be indistinguishable from bulk modes.

A useful way to study resonant modes is to examine the the local density-of-states. This can be computed from the diagonal elements of the Green's function $G_{ii}$ according to

$$-\frac{1}{\pi}\mathrm{Im}G_{ii} = i^{th} \text{ partial density-of-states.} \tag{5.20}$$

For a perfect crystal the local density-of-states is identical at each equivalent atomic site. For the imperfect crystal, defect modes will be seen as peaks in the local density-of-states near the defect. The Green's function for the imperfect crystal is given by Dyson's equation

$$\mathbf{G} = \mathbf{G}^0 + \mathbf{G}^0 \delta \mathbf{L} \mathbf{G}, \tag{5.21}$$

with the solution

$$\mathbf{G} = (1 - \mathbf{G}^0 \delta \mathbf{L})^{-1} \mathbf{G}^0. \tag{5.22}$$

Partitioning **G** in the manner of Eq. (5.17), we find that the Green's function for the imperfect crystal, in the space of the defect, can be computed from

$$\mathbf{g} = \mathbf{q}^{-1} \mathbf{g}^0 \tag{5.23}$$

where $\mathbf{q} = (1 - \mathbf{g}^0 \delta \mathbf{l})$. Roughly speaking, peaks in **g** should occur near zeroes of **q**. For a multi-dimensional **q** we can search for zeroes in its eigenvalues. For localized modes, **q** and its eigenvalues are real. For resonant modes, $\mathbf{g}^0$ and **q** are complex, but peaks in **g** may still occur near zeroes in the real part of the eigenvalues of **q**. If the eigenvalues of **q** are denoted by $\lambda$, then the energy of a defect mode is given by $E = \hbar\omega$, at those $\omega$ values which satisfy

$$\mathrm{Re}\lambda(\omega^2) = 0. \tag{5.24}$$

This equation unambiguously defines the energies of localized modes, but it is a somewhat arbitrary definition of a resonant defect mode. In general the local density-of-states as computed from Eqs. (5.20) and (5.23) should be examined. However Eq. (5.24) is a useful shorthand for locating resonant modes. The width in terms of $\omega^2$ of such a mode can be shown to be[19]

$$\Gamma = \frac{2\mathrm{Im}\lambda}{\frac{d}{d\omega^2}\mathrm{Re}\lambda} \tag{5.25}$$

evaluated at those values of $\omega^2$ which satisfy Eq. (5.24). The width is terms of energy is given by $\hbar\Gamma/2\omega$.

**5.2.4 Computation of Green's Functions**

In the previous section we considered the method by which the Green's function is used in the solution for defect modes. Here, we will discuss the actual computation of the function. Maradudin[19] has shown that the Green's function for the perfect crystal can be expressed as

$$G^{0\,\alpha\beta}_{lm\,ab}(\omega^2) = \frac{1}{N\sqrt{m_a m_b}} \sum_{n\mathbf{k}} \frac{\xi^{\alpha}_{a}(n\mathbf{k})\xi^{\beta\,*}_{b}(n\mathbf{k}) \exp[i\mathbf{k}\cdot(\mathbf{R}_{la} - \mathbf{R}_{mb})]}{\omega^2 + i\epsilon - \omega^2_{n\mathbf{k}}}, \qquad (5.26)$$

where $l$ and $m$ label unit cells, $a$ and $b$ label atomic types, and $\alpha$ and $\beta$ label cartesian components. $\omega^2_{n\mathbf{k}}$ are the eigenvalues and $\xi^{\alpha}_{a}(n\mathbf{k})$ are the eigenvectors of the $(n\mathbf{k})^{th}$ normal mode.

To produce a Green's function suitable for computation, we will apply two coordinate transformations. The first transformation is quite trivial and its effect is to drop the masses $m_a$ and $m_b$ from Eq. (5.26) and to absorb them in the defect perturbation $\delta\mathbf{L}$. This corresponds to expressing $\mathbf{G}^0$ with respect to the reduced coordinates $q_i = \sqrt{m_i}\,u_i$ where $u_i$ are cartesian coordinates. Second, we transform to the collective coordinates $Q_i$ discussed in Section 5.2.1 and defined in Table 5.1. In this coordinate system, $(s)$ and $(r)$ label the irreducible representation, $\sigma$ and $\rho$ label the occurence of the representation, and $\mu$ and $\nu$ label the row or column of the representation. The Green's function can now be expressed as

$$G^{0\,\mu\nu}_{(s)(r)\,\sigma\rho}(\omega^2) = \frac{1}{N} \sum_{n\mathbf{k}} \frac{Q^{\mu}_{(s)\sigma}(n\mathbf{k}) Q^{\nu}_{(r)\rho}{}^{*}(n\mathbf{k})}{\omega^2 + i\epsilon - \omega^2_{n\mathbf{k}}}. \qquad (5.27)$$

The summation on $\mathbf{k}$ extends over the entire first Brillouin zone. This can be divided into a sum over the irreducible wedge of the zone and a sum over the group elements $R$ which define the star of $\mathbf{k}$. Since the $Q$ coordinates form

bases for irreducible representations of the $T_d$ group, they are orthogonal[21] when summed over $R$, and we find that

$$G^{0\ \mu\nu}_{(s)(r)\ \sigma\rho}(\omega^2) = \frac{1}{N} \sum_{n\mathbf{k}\in wedge} \delta_{\mu\nu}\delta_{(s)(r)} \frac{\frac{h_\mathbf{k}}{d_s}\sum_\kappa Q^\kappa_{(s)\sigma}(n\mathbf{k}) {Q^\kappa_{(s)\rho}}^*(n\mathbf{k})}{\omega^2 + i\epsilon - \omega^2_{n\mathbf{k}}}, \qquad (5.28)$$

where $h_\mathbf{k}$ is the number of points in the star of $\mathbf{k}$, and $d_s$ is the dimension of the representation $(s)$. We see that the Green's function is zero unless $(s) = (r)$ and $\mu = \nu$ (in which case it is not dependent on the value of $\mu$). Keeping these zero elements in mind, we can simplify the notation by dropping the subscripts $\mu$, $\nu$, and $(r)$. Futhermore, the Green's function can explicitly be divided into its real and imaginary parts by defining the partial density-of-states ("spectral density"):

$$D_{(s)\sigma\rho}(\omega^2) = \frac{1}{N} \sum_{n\mathbf{k}\in wedge} \frac{h_\mathbf{k}}{d_s} \sum_\kappa Q^\kappa_{(s)\sigma}(n\mathbf{k}) {Q^\kappa_{(s)\rho}}^*(n\mathbf{k}) \delta(\omega^2 - \omega^2_{n\mathbf{k}}), \qquad (5.29)$$

from which Eq. (5.28) can be expressed as

$$G^0_{(s)\sigma\rho}(\omega^2) = P\int d\bar{\omega}^2 \frac{D_{(s)\sigma\rho}(\bar{\omega}^2)}{\bar{\omega}^2 - \omega^2} - i\pi D_{(s)\sigma\rho}(\omega^2) \qquad (5.30)$$

where $P$ signifies a principal value integral. Equations (5.29) and (5.30) are in a form suitable for computation. The sum over $\mathbf{k}$ (in the first Brillioun zone) was reduced to a sum over the irreducible wedge (1/48 of the zone for the zinc-blende structure) and was performed using the Gilat-Raubenheimer method[22,23]. The principal value integral was then computed following Bernholc and Pantelides[17].

**5.2.5 Evaluation of Defect Modes**

Once the Green's function matrix for the perfect crystal is known, the vibrational modes of a defect can be computed in a fairly straightforward manner. The defect perturbation matrix (difference between the **L**-matrices of the perfect and imperfect crystals) must be written down and evaluated. The Green's function for the imperfect crystal in the space of the defect is then computed from Eq.

**Table 5.3:** The vibrational modes of an $OGa_4$ molecule imbedded in a rigid zinc-blende lattice. Springs with bond-stretching constant $f_1'$ and bond-bending constant $f_2'$ connect the O-atom to its neighboring Ga-atoms. The Ga-atoms are connected to their outer neighbors by springs with constants $f_1$ and $f_2$. The defect perturbation matrix used in the Green's function calculation can be obtained from these formulae using the substitutions given in the text.

$$\omega^2(A_1) = \frac{1}{m_{\mathrm{Ga}}}\left(f_1' + \frac{1}{3}f_1 + \frac{8}{3}f_2\right)$$

$$\omega^2(E) = \frac{1}{m_{\mathrm{Ga}}}\left(f_2' + \frac{1}{3}f_1 + \frac{8}{3}f_2\right)$$

$$\omega^2(T_1) = \frac{1}{m_{\mathrm{Ga}}}\left(f_2' + \frac{1}{3}f_1 + \frac{8}{3}f_2\right)$$

$\omega^2(T_2) =$ eigenvalues of

$$\begin{bmatrix} \frac{1}{m_{\mathrm{Ga}}}(f_2' + \frac{4}{3}f_1 + \frac{5}{3}f_2) & 0 & \sqrt{\frac{8}{3m_{\mathrm{O}}m_{\mathrm{Ga}}}}f_2' \\ 0 & \frac{1}{m_{\mathrm{Ga}}}(f_1' + \frac{1}{3}f_1 + \frac{8}{3}f_2) & \sqrt{\frac{4}{3m_{\mathrm{O}}m_{\mathrm{Ga}}}}f_1' \\ \sqrt{\frac{8}{3m_{\mathrm{O}}m_{\mathrm{Ga}}}}f_2' & \sqrt{\frac{4}{3m_{\mathrm{O}}m_{\mathrm{Ga}}}}f_1' & \frac{1}{m_{\mathrm{O}}}(\frac{4}{3}f_1' + \frac{5}{3}f_2') \end{bmatrix}$$

(5.23), and this gives the local density-of-states (LDOS) for the imperfect crystal. Defect vibrational modes appear as peaks in the LDOS.

The form of the defect perturbation matrix $\delta\mathbf{l}$ is very similar to the **L**-matrix for a molecule consisting of the defect plus its neighboring atoms, imbedded in a rigid lattice. Rather than displaying $\delta\mathbf{l}$ itself, we will give the **L**-matrix for this defect molecule. In Table 5.3 we show elements of the **L**-matrix for an $OGa_4$ cluster imbedded in an immovable zinc-blende lattice. This matrix is actually $15 \times 15$. When expressed in terms of the collective coordinates, it is block diagonal, as dicussed in Section 5.2.1. The resulting nonzero matrix elements are given in Table 5.3. The $\omega^2$ values of the molecular modes are given by these matrix elements (or by the eigenvalues of the submatrices). The $\delta\mathbf{l}$-matrix used in the Green's function computations can be obtained from Table 5.3 by the substitutions:

$$\begin{aligned} f_1' &\rightarrow \Delta f_1 \\ f_2' &\rightarrow \Delta f_2 \\ f_1 &\rightarrow 0 \\ f_2 &\rightarrow 0 \\ m_O &\rightarrow m_P, \end{aligned}$$

and a term $-\omega^2(m_O - m_P)/m_P$ must be added to the third diagonal element of the $T_2$ matrix.

## 5.3 Results

### 5.3.1 Bulk Phonons

Shown in Fig. 5.2 are phonon dispersion curves computed from the two-parameter model described in Section 5.2.2. These curves can be compared with the experimentally determined phonon energies shown in Fig. 1.2(b). The values of the model parameters $f_1$ and $f_2$ have been chosen to produce a good fit to the

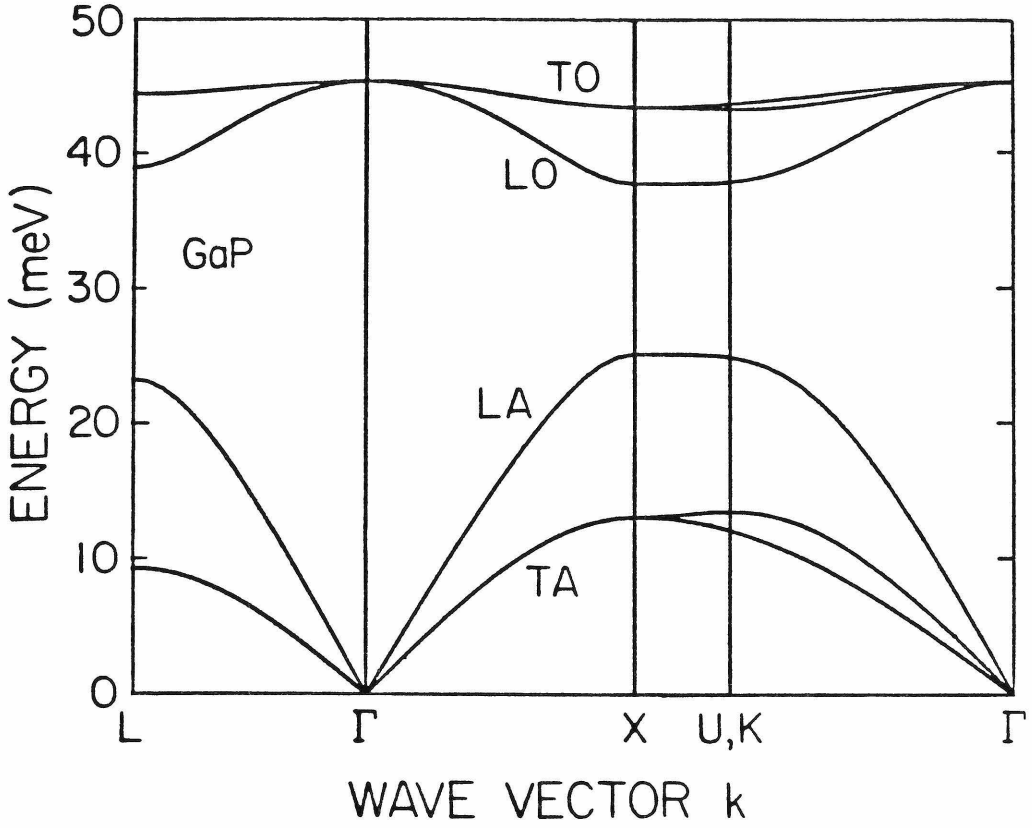


**Figure 5.2:** The phonon dispersion curves of GaP computed using the two-parameter model described in the text. The acoustic (A) and optical (O) branches are labelled according to the polarization of the phonons (T=transverse, L=longitudinal). Some branches may have mixed polarization.

actual phonon energies of GaP. The fit was accomplished by matching the TAX and TOΓ energies. From the dynamical matrix given in Table 5.2, these energies are given by

$$\omega^2(\mathrm{TO}\Gamma) = \frac{A}{\mu} \tag{5.31a}$$

and

$$\omega^2(\mathrm{TAX}) = \frac{A}{\mu}\left(\frac{1}{2} - \frac{1}{2}\sqrt{1 - \frac{4\mu}{m_{\mathrm{Ga}} - m_{\mathrm{P}}}\left[1 - \frac{B^2}{A^2}\right]}\right), \tag{5.31b}$$

where

$$A = \frac{4}{3}f_1 + \frac{8}{3}f_2, \quad B = -\frac{4}{3}f_1 + \frac{4}{3}f_2, \quad \text{and} \quad \mu = \frac{m_{\mathrm{Ga}}m_{\mathrm{P}}}{m_{\mathrm{Ga}} + m_{\mathrm{P}}}.$$

For GaP, the actual energies are known to be[28] $E(\mathrm{TAX}) = 13.1$ meV and $E(\mathrm{TO}\Gamma) = 45.4$ meV, from which the values for the force constants are determined to be $f_1 = 6.87$ eV/Å$^2$ and $f_2 = 0.525$ eV/Å$^2$.

The dispersion curves shown in Fig. 5.2 do have the major features of the actual GaP phonons, namely, three acoustic and three optical branches separated by an energy gap. In our model, the dispersion of the transverse branches is entirely due to the bond-bending interactions (*i.e.* if $f_2 = 0$ then the TA and TO branches would be flat). Rather than using bond-bending, we could have accomplished this dispersion of the transverse branches using second-nearest-neighbor interactions. For a purely covalent material the bond-bending model is more appropriate, and for a purely ionic material the use of second-nearest-neighbor interations is more appropriate. For GaP (partially ionic), probably both effects should be included. However, we have chosen to limit ourselves to bond-bending since this produces a more localized description of the material. The subsequent computation of Green's functions can then be accomplished with greater ease. In particular, for very weakly bonded defects we need only consider the nearest-neighbor interactions, rather than second-nearest neighbor

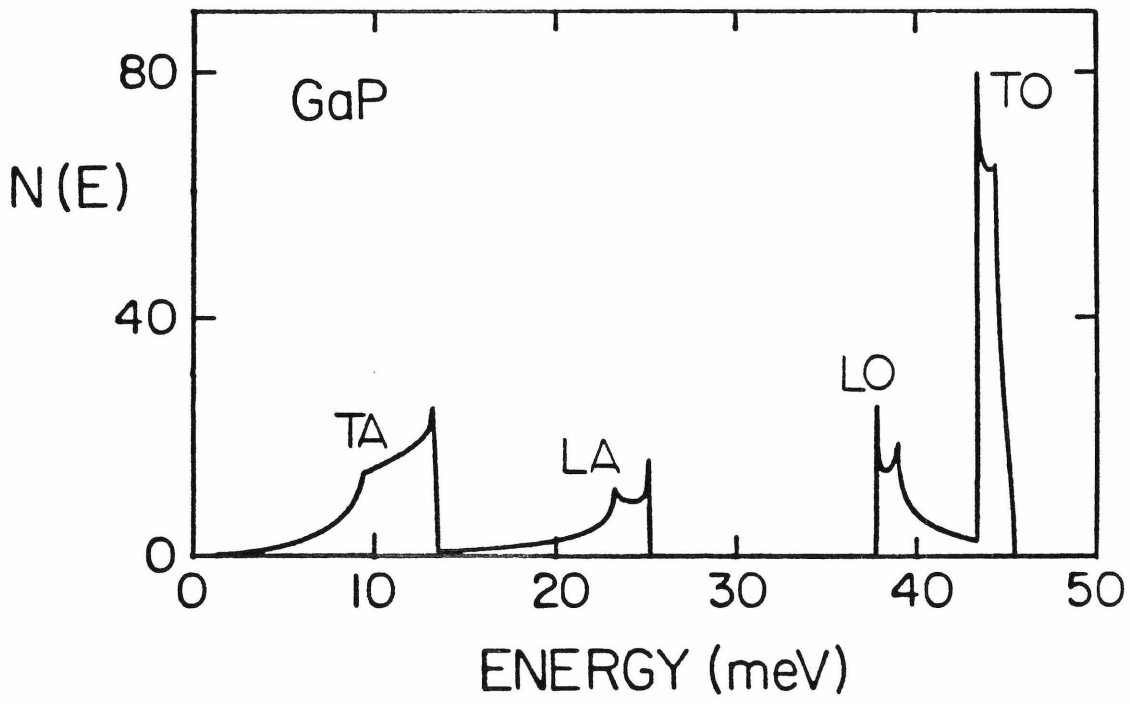


**Figure 5.3:** The density-of-states for the phonon modes in GaP computed using the two-parameter model described in the text. The acoustic (A) and optical (O) branches are labelled according to the polarization of the phonons (T=transverse, L=longitudinal). Some branches may have mixed polarization.

interactions. Also, the simplicity of the present model helps us to interpret the results in a straightforward fashion.

Shown in Fig. 5.3 is a computed density-of-states, which can be compared with that given by other models[5,25]. The major problem with the present computation is that the LO branch (near 40 meV) should actually be higher in energy. In our model, the TO and LO branches are degenerate at the $\Gamma$ point ($\mathbf{k} = \mathbf{0}$). In reality, the entire LO branch is raised in energy due to Coulomb interactions between the Ga and P ions. For GaP, this $\Gamma$-point splitting is 4.6 meV[24], so that the LO branch is raised above the TO branch. This discrepancy in the bulk phonons may affect some of the energies of the defect phonons which we will compute. However, we are not really concerned about the precise energies of the defect modes. The primary result of these calculations concerns the existence of the modes. Other models for the bulk phonons should produce the same number of defect modes as those seen here.

**5.3.2 Green's Functions**

Shown in Fig. 5.4 are the elements of the Green's function matrix for the perfect crystal, as computed from Eq. (5.29). These functions are computed using a P-site as the origin. We plot $-Im\mathbf{G}^0/\pi$ for the $A_1$, $E$, $T_1$, and the diagonal elements of the $T_2$ representations. We do not show the off-diagonal elements of the $T_2$ representations (there are three of these). Shown on the top of Fig. 5.4 is the bulk density-of-states. The Green's function elements are the partial densities of states in each of the various symmetry types. By summing these partial densities for both a P-site origin and a Ga-site origin we get the entire density-of-states:

$$-\frac{1}{\pi}\mathrm{Im}\left(\mathrm{Tr}\mathbf{g}^0_{\mathrm{P}}\right) - \frac{1}{\pi}\mathrm{Im}\left(\mathrm{Tr}\mathbf{g}^0_{\mathrm{Ga}}\right) = 5 \cdot N(\omega^2), \qquad (5.32a)$$

where

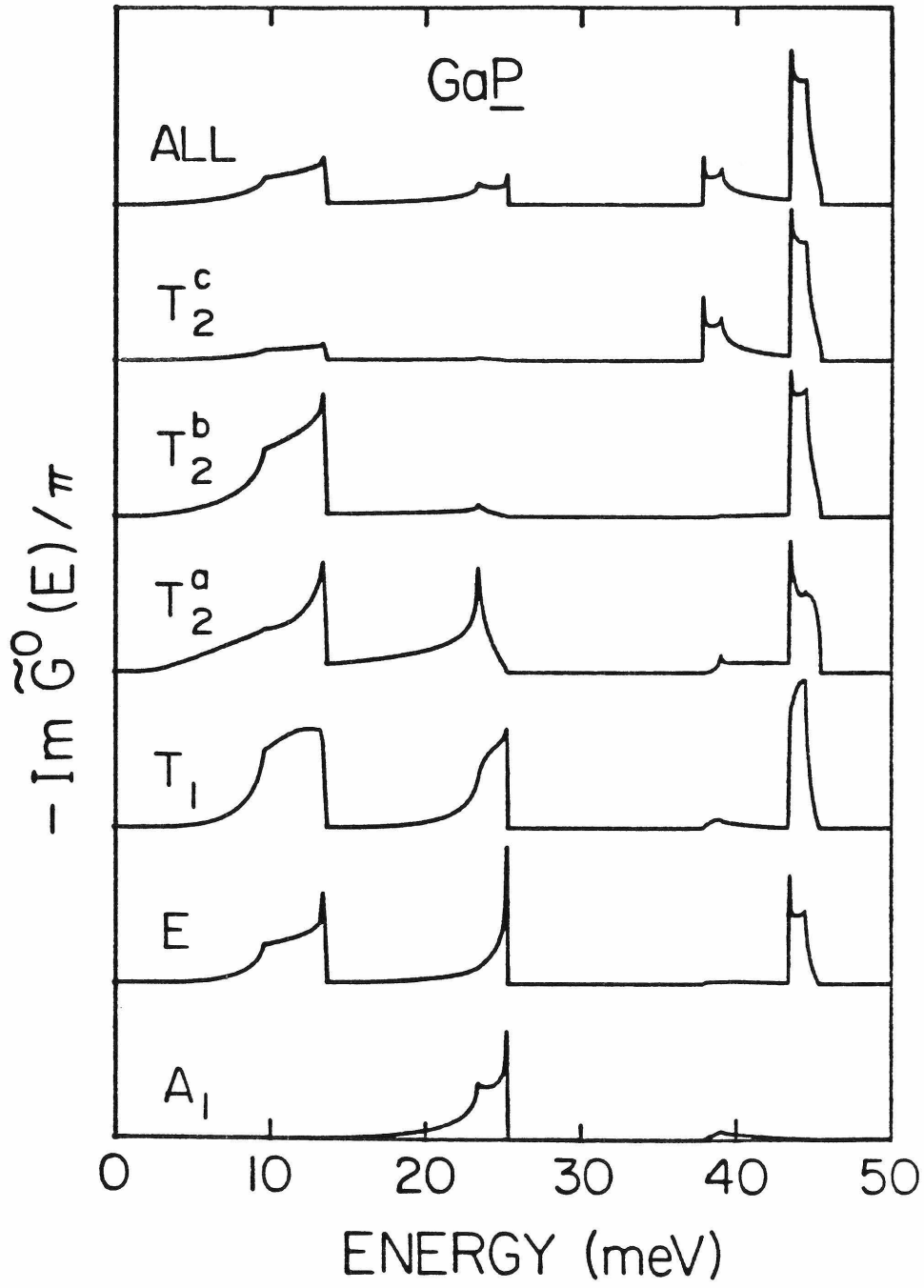


**Figure 5.4:** The imaginary part of the Green's function for the perfect crystal, using a P-site for the origin in space. At the top is shown the bulk density-of-states. The elements of the Green's function matrix shown here are the partial density-of-states into each of the $A_1$, $E$, $T_1$, $T_2^a$, $T_2^b$, and $T_2^c$ collective coordinates.

$$\mathrm{Tr}\mathbf{g} = \Big(g(A_1) + 2g(E) + 3g(T_1) + 3g(T_2^a) + 3g(T_2^b) + 3g(T_2^c)\Big). \qquad (5.32b)$$

The factor of 5 on the right-hand side of Eq. (5.32a) arises from the presence of 5 atoms in the defect cluster. The density-of-states obtained from Eq. (5.32) can be compared with that directly computed from

$$N(\omega^2) = \frac{1}{N}\sum_{n\mathbf{k}} \delta(\omega^2 - \omega_{n\mathbf{k}}^2). \qquad (5.33)$$

In our calculations, the $N(\omega^2)$ computed in these two ways agree to an absolute accuracy of 0.004. This agreement provides a very important check on the computation of the Green's functions.

The major part of the computation of the perfect crystal Green's function is performing the summation Eq. (5.29). The results presented here were computed using 5950 points in the irreducible wedge, corresponding to 256000 points in the entire zone. The computations were all performed as a function of $\omega^2$, using an $\omega^2$ interval of 4.12 meV$^2$. This corresponds to an accuracy of about 0.05 meV in the optical branches and 0.5 meV near the bottom of the acoustic branch. The number of points used in the **k**-space summation was consistent with this $\omega^2$ interval size. The Green's function elements $\tilde{G}(\omega)$ shown in Fig. 5.4 were computed from $G(\omega^2)$ by

$$\tilde{G}(\omega)d\omega = G(\omega^2)d\omega^2. \qquad (5.34)$$

The Ga-site Green's function elements are identical with the P-site Green's function elements except that the relative amplitude of the acoustic and optical modes is reversed (*e.g.* the $A_1$ Ga-site partial density of states has a small peak in the acoustic branch and a large peak in the optical branch).

### 5.3.3 Defect Vibrational Modes

The vibrational modes of a defect are characterized by a peak in the local density-of-states (LDOS). This peak is the center of a band of vibrational modes

in which the defect vibrates with significantly greater amplitude than those atoms far removed from it. The LDOS is computed from the imaginary part of the Green's function for the imperfect crystal, which is computed from the Green's function for the perfect crystal and from the defect perturbation matrix. The defect we are considering here consists of an impurity atom substitutional for the P atom. Our results are for oxygen, with a mass defect parameter of

$$\frac{\Delta m}{m} = \frac{m_O - m_P}{m_P} = -0.4834\,. \tag{5.35}$$

The springs which connect the impurity to its nearest neighbors are described by a bond-stretching $f_1'$ and a bond-bending $f_2'$ interaction. These interactions are allowed to differ from those of the bulk, and they are varied by the same fractional amount. Thus, the defect perturbation matrix depends on one parameter $\Delta f/f$, the fractional change in spring constants for the defect relative to the bulk material:

$$\frac{\Delta f}{f} = \frac{f_1' - f_1}{f_1} = \frac{f_2' - f_2}{f_2}, \tag{5.36}$$

where $f_1$ and $f_2$ are the bulk spring constants. Negative value of $\Delta f/f$ refer to a weakly bonded defect and positive values of $\Delta f/f$ refer to a strongly bonded defect. By definition, $\Delta f/f \geq -1$. It seems physically unlikely that a substitutional impurity will form bonds which are very much stronger than those of the bulk material. Therefore, we will concentrate our attention on the range of $\Delta f/f$ values $-1 < \Delta f/f < 1$.

For a given value of defect spring constants, we compute a LDOS for each type of vibrational mode ($A_1$, $E$, $T_1$, and $T_2$). The LDOS reflects some details of the bulk vibrational modes, as well having peaks for each of the defect modes. For defect perturbation values in the range $-1 < \Delta f/f < 1$, we find defect modes of $A_1$ and $T_2$ symmetry only. The $A_1$ (breathing) mode shown in Fig. 5.5

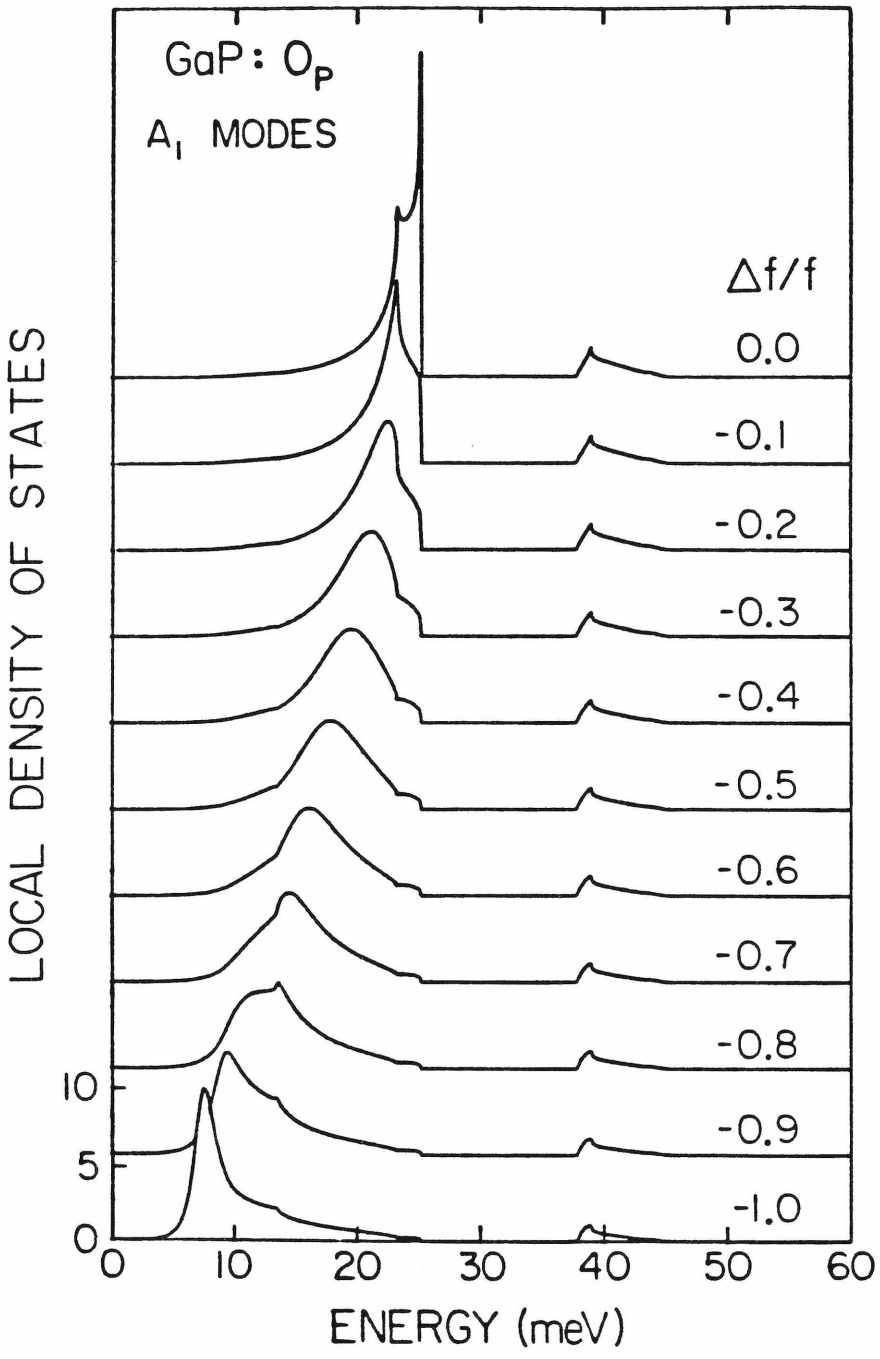


**Figure 5.5:** The local density-of-states of $A_1$ modes for an O atom on a P-site in GaP. The defect force constant $\Delta f/f$ is varied from $\Delta f/f = 0$ (defect springs identical to bulk springs) to $\Delta f/f = -1$ (defect springs of zero strength). A resonance in the acoustic branch appears as a peak in the local density-of-states. This resonance moves to lower energies as the defect force constant is reduced.

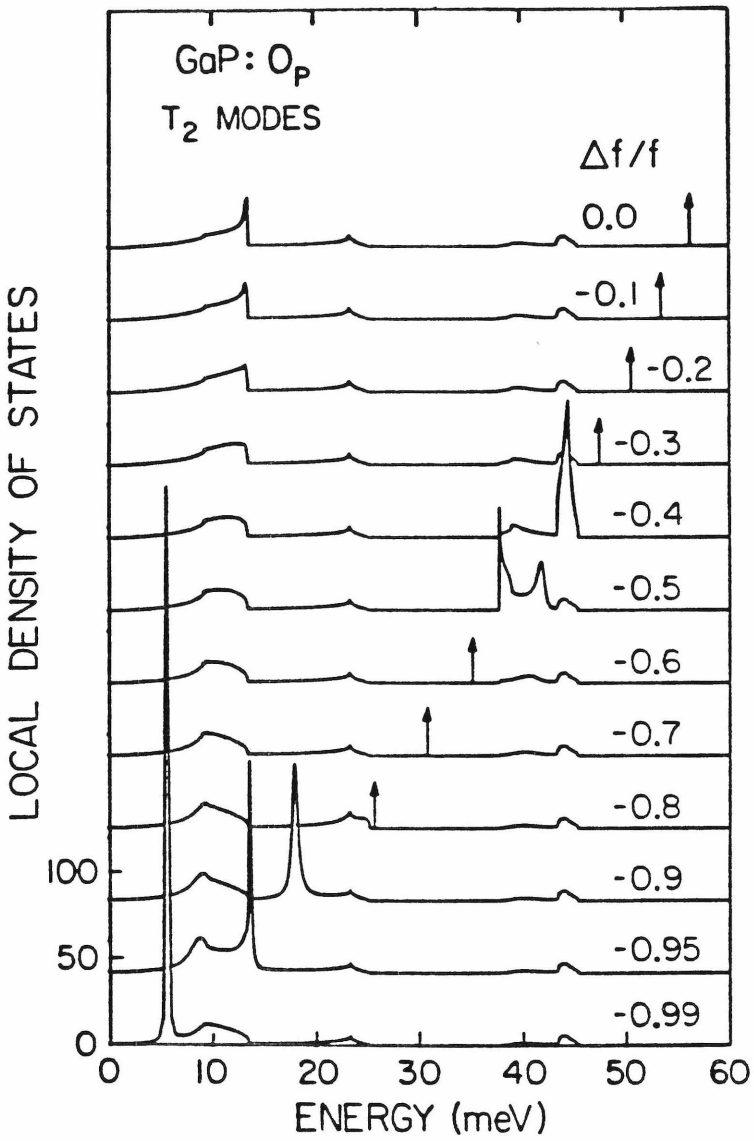


**Figure 5.6:** The local density-of-states of $T_2$ modes for an O atom on a P-site in GaP. The defect force constant $\Delta f/f$ is varied from $\Delta f/f = 0$ (defect springs identical to bulk springs) to $\Delta f/f \rightarrow -1$ (defect springs of zero strength). For $\Delta f/f = 0$ a localized mode at 56 meV is shown as a $\delta$-function in the local density-of-states. As $\Delta f/f$ is reduced, this mode moves to lower energies, entering the optical branch as a resonance, becoming localized in the acoustic-optical gap, and entering the acoustic branch as a sharp resonance. As $\Delta f/f \rightarrow 0$ the mode approaches a $\delta$-function at zero energy, corresponding to motion of the O atom in the absence of any restoring force.

is a resonance in the acoustic branch. For $\Delta f/f = 0$ the $A_1$ LDOS curve at the top is identical to the $A_1$ Green's function for the perfect crystal. As $\Delta f/f$ is reduced, a resonance mode appears and moves to lower energies. This resonance is rather broad, with a width of about 5 meV. The sum of the LDOS for the $T_2^a$, $T_2^b$, and $T_2^c$ modes is shown in Fig. 5.6. These modes consist of vibrations of the oxygen atom itself, along with some response of the rest of the lattice. For $\Delta f/f = 0$ we see a localized mode at about 56 meV. As $\Delta f/f$ is reduced this $T_2$ mode falls in energy; entering the optical branch as a resonance, becoming localized in the acoustic-optical gap, and finally entering the acoustic branch as a rather sharp resonance. As $\Delta f/f \rightarrow 0$, the $T_2$ mode approaches a $\delta$-function at zero energy. This corresponds to motion of the oxygen atom in the absence of any restoring force. The $T_2$ resonances in the optical and acoustic branches are rather sharp, with a width of about 2 meV or less.

The results from the LDOS calculations are summarized in Fig 5.7. Here we plot the energies of the defect modes versus the defect spring constant parameter. On the left-hand side of the figure a bulk density-of-states is shown for reference. The solid lines in the figure are the results from the Green's functions. These energies are defined as the location of zeroes in the real part of the eigenvalues of the **q**-matrix, Eq. (5.24). For $\Delta f/f < 0$ we see the $A_1$ and $T_2$ modes discussed above. For $\Delta f/f > 0$ another $T_2$ mode appears as a resonance in the acoustic branch. For $-1 < \Delta f/f < 1$, no defect modes of $E$ or $T_1$ symmetry occur (*i.e.* there are no zeroes in the real part of the eigenvalues of their **q**-matrices). Physically, this means that $E$ and $T_1$ vibrations of the defect are strongly coupled to the bulk crystal, so that these types of motion are not at all localized near the defect. The defect perturbation for the $E$ and $T_1$ modes contains only bond-bending interactions, which are too weak to produce defect modes for $-1 <$

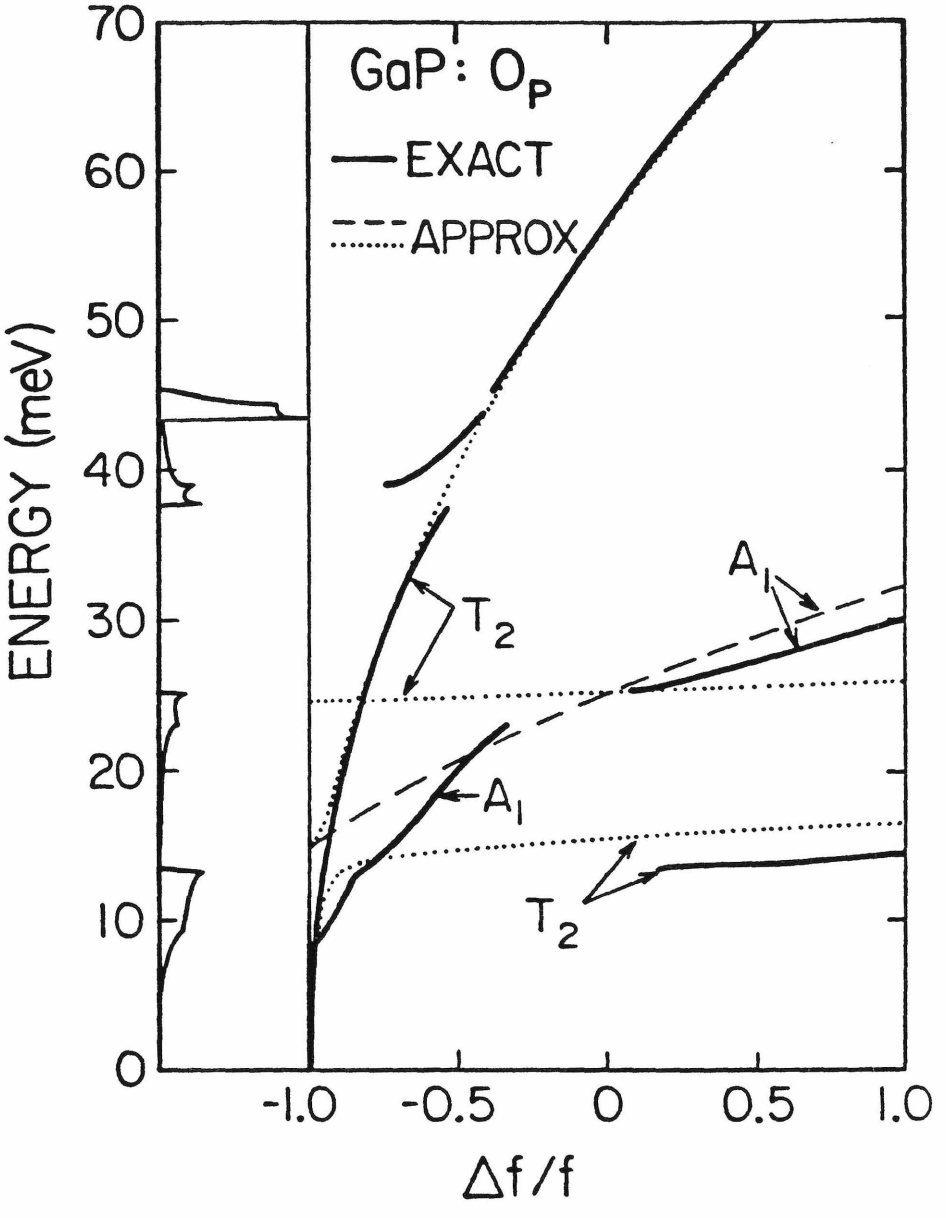


**Figure 5.7:** The defect vibrational modes of oxygen on a P-site in GaP. The energy of the modes is plotted versus the defect force constant $\Delta f/f$. Values of $\Delta f/f < 0$ imply a weakly-bonded defect, and values of $\Delta f/f > 0$ imply a strongly-bonded defect. The heavy solid lines show the solutions from the Green's function calculations. These solid lines indicate roughly the location of peaks in the local density-of-states. An approximate solution for the defect modes is given by the normal modes of a 5-atom "molecule" imbedded in a rigid lattice. The dashed lines gives the approximate $A_1$ modes and the dotted lines give the approximate $T_2$ modes.

$\Delta f/f < 1$. For $\Delta f/f \gg 1$, $E$ and $T_1$ modes do appear. The defect perturbation for $A$ and $T_2$ modes contains bond-stretching and mass-defect terms which are relatively large and produce the modes shown here.

The energy of some Green's function modes are quite close to those calculated from a simple molecular model. In Fig. 5.7 we show the modes for a $OGa_4$ molecule imbedded in a rigid lattice, as listed in Table 5.3. The dashed line is the $A_1$ molecular modes, which agree roughly with the Green's function modes. The dotted lines give the $T_2$ molecular modes. There are three of these modes for each value of $\Delta f/f$. The molecular modes and Green's function modes agree very well for the high energy localized $T_2$ mode, whose energy is given asymptotically by

$$\omega^2 \sim \frac{1}{m_O}\left(\frac{4}{3}f_1' + \frac{8}{3}f_2'\right) + \frac{1}{m_{Ga}}(f_1' + f_2'). \tag{5.37}$$

The second term on the right-hand side of this equation is due to the nearest-neighbor Ga atoms, whose motion always makes a significant contribution to the energy of the mode. Some of the molecular modes agree closely with the Green's function modes, but other molecular modes appear where there are no Green's function modes. In the latter case, the vibration of the defect molecule is strongly coupled to the bulk modes so that a peak in the LDOS does not appear. This illustrates the major deficiency of the molecular model results — the number of modes is determined by the size of the cluster. The Green's function method allows us to couple these molecular modes to the rest of the crystal in order to see if they remain somewhat localized around the defect. The real importance of the molecular mode calculation is that it provides a very good check on the Green's function computation, since in certain limits the modes from both methods agree quite well.

### 5.3.4 Comparison of Theory and Experiment

Now let us compare the theoretical results with experiment. The vibrational

modes of GaP:O have been observed in a number of photoluminescence experiments. Here, we will discuss those modes associated with the charge state $O^+$, *i.e.* without the donor electron present. These modes are shown in Fig. 3.2(b), in the luminescence band marked $m \rightarrow \infty$. As discussed by other workers[26,27], the defect phonons consist of a 19 meV mode (resonance in the acoustic branch), and a 47 meV mode (resonance in the optical branch). Comparing these modes with the results shown in Fig. 5.7, we see that for a defect spring constant of $\Delta f/f \approx -0.5$, the theory predicts two resonances in approximately the right location. The 19 meV mode we identify as being an $A_1$ type motion. As shown in Fig. 5.1(b) this mode consists as a radial "breathing motion" of the nearest-neighbor Ga atoms. The 47 meV mode we identify as having $T_2$ symmetry. This mode involves motion of the O atom itself, as shown in Fig. 5.1(c). In general, for the oxygen impurity with reduced spring constants, our theory predicts the existence of two defect modes, and this is just what is observed in experiment.

### 5.4 Conclusions

In this chapter, we theoretically analyze the vibrational modes of oxygen in GaP. For the charge state $O^+$, two resonant vibrational modes are observed in experiment. On the basis of our calculations we identify these modes as an $A_1$ breathing mode of the oxygen nearest-neighbors, and a $T_2$ motion of the oxygen atom itself. From the observed energies of the modes we find that the O-Ga spring constants are roughly 50% of the bulk P-Ga spring constants, which indicates that O in GaP is a weakly bonded defect. This has implications to the dissociation of the (Zn,O) pairs discussed in Chapter 3, since it suggests that it may be the oxygen atom that moves in the dissociation, rather than the zinc

atom. The techniques developed here can be used to analyze the vibrational modes of any type of substitutional defect in a zinc-blende lattice. With some additional effort, other types of defects can also be treated. We hope to continue this work and examine the vibrational modes of (Zn,O) pairs in GaP. This should lead to a greater understanding of the atomic motions which occur when the pairs dissociate.

Aside from the results for particular defects, the calculations in this chapter illustrate some general properties of the normal modes of defects in crystals. We have treated both localized and resonant modes, and we have shown how these types of modes are similar in many ways. Both types of modes are observed in photoluminescence experiments. The important quantity in the theory is the local density-of-states, which tells us how much of the mode is concentrated near the defect. Localized and resonant modes both appear as peaks in the local density-of-states. Also, we have shown how the vibrational modes of molecules imbedded in a rigid lattice are similar to the defect modes obtained from the Green's function calculations. The important aspect of the Green's function results is that they show how a vibration of the defect couples into the rest of the lattice. Those modes which remain concentrated near the defect will be observed as defect modes, whereas those modes which are distributed equally throughout the entire crystal will be indistinguishable from the bulk modes.

## REFERENCES


1. A. Grimm, A. A. Maradudin, I. P. Ipatova, and A. V. Subashiev, *J. Phys. Chem. Solids* **33**, 775 (1972).
2. P. G. Dawber and R. J. Elliott, *Proc. Roy. Soc. A* **273**, 222 (1963).
3. K. Kunc, *Czech. J. Phys. B* **15**, 883 (1965).
4. R. J. Elliott and P. Pfeuty, *J. Phys. Chem. Solids* **28**, 1789 (1967).
5. S. P. Gaur, J. F. Vetelino, and S. S. Mitra, *J. Phys. Chem. Solids* **32**, 2737 (1971).
6. D. N. Talwar and Bal K. Agrawal, *Phys. Rev. B* **9**, 2539 (1974).
7. D. N. Talwar and Bal K. Agrawal, *Phys. Rev. B* **12**, 1432 (1975).
8. M. Vandevyver and P. Plumelle, *Phys. Rev.* **17**, 675 (1978).
9. M. Vandevyver and D. N. Talwar, *Phys. Rev. B* **21**, 3405 (1980).
10. K. K. Rebane, *Impurity Spectra of Solids*, (Plenum, New York, 1970).
11. C. H. Henry, P. J. Dean, and J. D. Cuthbert, *Phys. Rev.* **166**, 754 (1968).
12. T. N. Morgan, B. Welber, and R. N. Bhargava, *Phys. Rev.* **166**, 751 (1968).
13. C. Kittel, *Introduction to Solid State Physics*, $5^{th}$ ed., (Wiley, New York, 1976).
14. A. A. Maradudin, E. W. Montroll, G. H. Weiss, and I. P. Ipatova, *Solid State Physics*, Supplement no. 3, (Academic Press, New York, 1971), p. 16.
15. G. F. Koster and J. C. Slater, *Phys. Rev.* **95**, 1167 (1956).
16. J. Callaway, *J. Math. Phys.* **5**, 783 (1964); *Phys. Rev.* **154**, 515 (1967).
17. J. Bernholc and S. T. Pantelides, *Phys. Rev. B* **18**, 1780 (1978).
18. J. Bernholc, N. O. Lipari, and S. T. Pantelides, *Phys. Rev. B* **21**, 3545, (1980).
19. A. A. Maradudin, *Rep. Prog. Phys.* **28**, 331 (1965).
20. A. A. Maradudin, *Solid State Physics*, Vol. 18, (Academic Press, New York,

1966), p. 273.

21. M. Tinkham, *Group Theory and Quantum Mechanics*, (McGraw-Hill, New York, 1964), p. 23.
22. G. Gilat and L. J. Raubenheimer, *Phys. Rev.* **144**, 390 (1966).
23. J. F. Janak, in *Computational Methods in Band Theory*, edited by P. M. Marcus, J. F. Janak, and A. R. Williams (Plenum, New York, 1971), p. 323.
24. A. S. Barker, Jr., *Phys. Rev.* **165**, 917 (1968).
25. A. S. Barker, Jr. and A. J. Sievers, *Rev. Mod. Phys.* **47**, Supplement no. 2, (1975), p. S52.
26. P. J. Dean, C. H. Henry, and C. Frosch, *Phys. Rev.* **168**, 812 (1968).
27. B. Monemar and L. Samuelson, *J. of Luminescence* **12/13**, 507 (1976).
28. J. L. Yarnell, J. L. Warren, R. G. Wenzel, and P. J. Dean, in *Neutron Inelastic Scattering*, (IAEA, Vienna, 1968), Vol. 1, p. 301.